Novel Covalent Organic Frameworks (COFs) for Electrochemical Energy Storage and Conversion

ZHUYU WANG

A thesis submitted to fulfil requirements for
the degree of Master of Philosophy

School of Chemical and Biomolecular Engineering
The University of Sydney
2023

Authorship attribution statement

Chapter III of this thesis is published as:

Zhuyu Wang, Chaojun Wang, Yuan Chen and Li Wei, Covalent Organic Frameworks for Capacitive Energy Storage: Recent Progress and Technological Challenges, *Advanced Materials Technologies*, **2023**, 8, 2201828.

I contributed to manuscript writing and revision.

Chapter IV of this thesis has been submitted and under-review as:

Di Zhang, Zhuyu Wang, Fangzhou Liu, Peiyun Yi, Linfa Peng, Yuan Chen, Li Wei, and Hao Li, From Single to Double Sabatier Optima: the pH-Dependency of Oxygen Reduction on M-N-C Catalysts

I contributed to material synthesis, performance test, data analysis, and manuscript writing.

Attesting authorship attribution statement

In addition to the statements above, in cases where I am not the corresponding author of a published item, permission to include the published material has been granted by the corresponding author.

Zhuyu Wang

As supervisor for the candidature upon which this thesis is based, I can confirm that the authorship attribution statements above are correct.

Yuan Chen

Statement of originality

This is to certify that to the best of my knowledge, the content of this thesis is my own work. This thesis has not been submitted for any degree or other purposes.

I certify that the intellectual content of this thesis is the product of my own work and that all the assistance received in preparing this thesis and sources have been acknowledged.

Zhuyu Wang

Acknowledgments

This thesis not only represents the personal learning and research achievements during my MPhil studies but also encompasses the support and assistance provided by my supervisors, collaborators, and family members. I would like to express my gratitude to them for their invaluable contributions.

In the past two years, I have experienced the frustration of failed experiments and the immense pressure of changing researches, as well as the psychological anxiety of not being able to complete my studies successfully due to the lockdown caused by the COVID-19 outbreak. However, amidst these challenges, I have also gained precious experiences. The two different research projects have broadened my horizon and expanded my knowledge, providing me with a deeper understanding of academic research. At the same time, the care and guidance of my supervisors, and the help and cooperation of my colleagues in the group have brought me immense warmth and hope. Additionally, I successfully published a literature review and have submitted an academic paper for the second project.

First and foremost, I would like to express my gratitude to my supervisors, Prof. Yuan Chen, and Dr. Li Wei. They have provided comprehensive and meticulous guidance throughout my experimental research and the completion of my papers. Despite their busy schedules, they have assisted me in resolving the issues and difficulties encountered during my research through weekly meetings, phone calls, and emails.

Secondly, I would like to thank my team members, who have been of great assistance during my MPhil. They have conducted in-depth research in different domains and have provided me with reasonable advice and suggestions based on their practical experiences.

I would also like to express my deepest gratitude to my family, especially my grandfather and uncle, who cared about my studies and life before their sudden passing. I regret not being able to see them one last time. I am grateful to my family for their unwavering support, both financially and emotionally. Without them, I would not have been able to successfully complete my studies.

Finally, I extend my deep appreciation to all those who have supported, taught, encouraged, and helped me in my studies and life during these two years.

List of publications

1. Zhuyu Wang, Chaojun Wang, Yuan Chen, Li Wei, Covalent Organic Frameworks for Capacitive Energy Storage: Recent Progress and Technological Challenges. *Advanced Materials Technologies* 2023, 8, 2201828.
2. Di Zhang, Zhuyu Wang, Fangzhou Liu, Peiyun Yi, Linfa Peng Yuan Chen, Li Wei, and Hao Li, From Single to Double Sabatier Optima: the pH-Dependency of Oxygen Reduction on M-N-C Catalysts. *ArXiv. Physics. Chem* 2023, 8, 11182.

Table of Contents

List of Figures

List of Tables

Abstract

Covalent Organic Frameworks (COFs) are a new type of crystalline porous organic materials composed of covalently linked organic molecular modules. They possess the advantages of ordered channels, nano-scale pore structures, large specific surface areas and high crystallinity. Meanwhile, unlike traditional linear polymerization leading to uncontrolled product structures, COFs can be designed to form highly regular structures in two or even three dimensions. In addition, rigid structures can provide excellent stability for COFs. Furthermore, the designable structure allows functional groups to be introduced into COFs to meet the specific requirements of devices. As a result, COFs have been widely used in various fields. In particular, COFs have been found to be suitable for electrochemical energy conversion and storage applications. In this thesis, I present two conceptual applications of COFs as electrochemical active material in supercapacitors for energy storage and as electrocatalysts bearing the metal-nitrogen-carbon single-atom structure for the oxygen reduction reaction. The results demonstrated in this thesis represent the specific applications of COFs in electrochemistry, offering further possibilities and new ideas for developing novel materials for electrochemical energy storage and conversion.

Keywords: covalent organic frameworks; supercapacitors; oxygen reduction reaction

Chapter I. Introduction

1.1 Covalent Organic Frameworks (COFs) as novel porous materials

More advanced, stable and tunable new materials have been extensively investigated in order to accommodate the emergence and application of a wide range of devices with complex structures and multifunctionality.[1] Different chemical connections, such as intermolecular hydrogen bonds, π-π interactions, coordination bonds and covalent bonds, can synthesize various inorganic or organic materials with different dimensions as well as pore and topologies structures.[2] The emergence of these materials has led to wide-ranging applications in various fields and has facilitated the production and use of more large-scale devices.

Covalent bonding as a strong interaction has been widely employed in a large variety of polymeric materials. From everyday items such as polyethylene and polystyrene plastics as well as nylon fabrics to microporous polymers used in precision instruments.[3] Through connected by covalent bonds, many small monomeric units can be linked together to form long-chain polymers with stable and rigid structures. However, the disordered skeleton, the linear linkage, and the singular pore structure of these polymers impose limitations on their applications.

In 2005, a new class of porous polymers linked by covalent bonds was first reported and named covalent organic frameworks (COFs).[4] Such polymers, which are called COFs, have polymeric structures with periodic π-conjugated frameworks and are connected by strong covalent bonds such as C−N, B−O, and N−N. The two 2D COFs (COF-1 and COF-5) were synthesized through the condensation of $C_6H_4[B(OH)_2]_2$ and

$C_{18}H_6(OH)_6$, respectively. They exhibited large specific surface areas of 711 $m^2\ g^{-1}$ and 1590 $m^2\ g^{-1}$, with pore volumes of 0.32 $cm^3\ g^{-1}$ and 0.998 $cm^3\ g^{-1}$, respectively. The exceptional porosity came from the combined contribution of micropores and mesopores. Furthermore, the rigid structure linked by covalent bonds presented excellent thermal stability and maintained its structure even at a high temperature of 600 °C. Subsequently, 3D COFs were synthesized by the same research group.[5] These two 3D COFs, named COF-102 and COF-103, were obtained through the condensation of precursors with a tetrahedral structure. Similar to the 2D COFs, the strong intermolecular interactions contributed to the high thermal stability of the 3D COFs (<500 °C). However, unlike the 2D COFs, COF-102 and COF-103 exhibited low densities of 0.41 g cm^{-3} and 0.38 g cm^{-3}, respectively. The three-dimensional structure also led to better exposure of active sites within the COFs. Consequently, these two COFs demonstrated exceptional specific surface areas of 3472 $m^2\ g^{-1}$ and 4210 $m^2\ g^{-1}$, along with excellent pore volumes (1.35 $cm^3\ g^{-1}$ and 1.66 $cm^3\ g^{-1}$).

In addition to their large specific surface area, diverse pore structures and low density, COFs possess numerous unique advantages. Firstly, the designable modules allow for structural controllability, tunability, and regularity. Secondly, COFs can form three-dimensional structures rather than only a single linear structure by condensing building blocks with two- or three-dimensional architectures. Thirdly, the nanoporous framework of COFs provides channels and spaces for ion transport and storage. Fourthly, the rigid structure contributes to their high thermal and chemical stability. Fifthly, a large contact area can be provided by COFs and resulting in more active site

exposure. Sixthly, the open channels in COFs facilitate ion transport and enhance the interaction between ions and active sites. Seventhly, the abundant channels also provide pathways for fast charge carriers after doping with other conductive materials. Therefore, the conductivity of composite materials can be enhanced. Based on these advantages, COFs have been used in several applications, including gas separation,[6] gas storage,[7] catalysis,[8] semiconductors,[9] optoelectronics,[10] drug delivery,[11] sensors,[12] as well as energy storage and conversion devices.[13]

The common characterization methods of COFs are as follows. (1) The surface morphology and structural profile of COFs can be observed by SEM and TEM. (2) The internal composition and functional group distribution can be analyzed by FT-IR. (3) TGA can be used to test the thermal stability of COFs. (4) The phase purity and crystal structure of the samples can be evaluated by XRD. (5) The stacking mode and aggregation structure can be studied by NMR. (6) The pore structure and specific surface area of COFs can be analyzed by BET. (7) The composition and valence of elements in the samples can be determined by XPS.

1.2 COFs in electrochemistry

In response to the energy crisis, the development of efficient, environmentally friendly, and sustainable energy conversion and storage devices is imperative. The function and lifetime of electrochemical devices rely on their electrode materials. Typically, energy conversion occurs at the surface of the electrode, while energy storage requires transmission through the pore structure of the material. The unique advantages of COFs

make them highly suitable as electrode materials. Firstly, COFs can be designed with well-defined internal structures and tunable porosity by selecting and constructing appropriate building blocks. Secondly, the nano-mesh structure provides a larger contact area and more active sites. Thirdly, the interconnected multi-level channels facilitate rapid ion and charge transport, enabling better contact between ion and active sites. Fourthly, different functional groups can be introduced into COFs through post-synthetic modifications. This flexible designability supports specific requirements for different functional devices.

In this thesis, I first provide a comprehensive discussion of the synthesis and preparation methods of COFs. Then, post-modification strategies are explored for specific characteristics and requirements. Furthermore, based on the recent advancements and developments of COFs in electrochemistry, I specifically emphasize their applications in supercapacitors and oxygen reduction reactions.

Supercapacitors, known for their high capacitance and have garnered significant attention in energy storage devices due to their fast charge-discharge rates and long cycle life.[14] COFs, with their large specific surface area and abundant pore structures, have demonstrated immense potential as electrode materials for supercapacitors. However, the presence of van der Waals forces between COF nanosheets leads to their self-stacking, which is detrimental to the exposure of active sites and particle transport. As a result, the electrode performance is severely compromised. Moreover, the inherent poor conductivity limits the migration of charge carriers. An effective way to solve this problem is to introduce graphene, a highly conductive material, into COFs because

graphene can not only serve as a physical spacer to prevent the stacking of nano-layers but also enhance the overall conductivity of the composite material.

The oxygen reduction reaction (ORR) plays a crucial role in energy conversion processes. However, the low mass transfer efficiency of ORR leads to sluggish kinetics, seriously affecting the performance of energy storage devices, particularly in fuel cells and metal-ion batteries.[15] Therefore, highly efficient catalysts have been developed. The high abundance, low-cost non-precious metal catalysts are excellent candidates. COFs, as porous polymers with a designable framework structure, are well suited as templates for metal embedding. Meanwhile, metals can be better anchored due to the rigid structure of COFs, which allows a well-defined and controlled coordination environment for metals and thus improves the utilization of metal atoms. In addition, a rich pore structure can improve ion transport and storage. Finally, the large specific surface area facilitates the exposure of catalytic active sites, thus enhancing the contact of ions with the active sites.

Chapter II. Literature Reviews

COFs have been extensively studied as a new type of organic material linked by rigid covalent bonds. Therefore, this chapter will first provide an overview of COFs design and synthesis methods, including solvothermal synthesis, ionothermal synthesis, microwave synthesis, sonochemical synthesis and mechanochemical synthesis. Secondly, their post-synthetic modifications are summarized, including methods for modifying porosity, conductivity, crystallinity, skeleton structure and functional groups. Finally, the applications of COFs in electrochemistry are outlined, including their use in water splitting, oxygen reduction reactions, rechargeable batteries and supercapacitors.

2.1 Synthesis and preparation of COFs

2.1.1 Solvothermal synthesis

The solvothermal method involves the reaction of precursors with organic or inorganic solvents within a vacuum-sealed reaction vessel, such as a heat-resistant glass bottle or a reaction flask. By applying temperatures higher than the boiling point of the solvent and utilizing the self-generated pressure of the closed system, the crystallization of the reactants is facilitated.[16] This method has a number of advantages. Firstly, the closed vacuum environment effectively prevents the oxidation of the reactants. Secondly, the heating conditions promote enhanced solubility of the reactants and the rate of reaction. Thirdly, organic solvents with low boiling points have a higher air pressure of their own, and the high air pressure is more favorable for the crystallization process. Fourthly, the solvothermal method facilitates the growth of COFs with fewer defects and higher

crystallinity. Hence, the solvothermal method is the most commonly employed approach for the synthesis of COFs.

Smith and the group reported the synthesis of a COF (COF-5) linked by boronic acid esters via a solvothermal method (Figure 2.1a and b).[17] The precursors were reacted with a 1 mL: 1 mL mixture of dioxane and mesitylene solvent in a sealed glass tube at 100 °C for 72 hours. The synthesized COF exhibited improved crystallinity and a large specific surface area of 2000 m^2 g^{-1}. Simultaneously, COF-5 demonstrated a rapid crystallization under solvothermal conditions. Within five minutes, the mass of the precipitate reached 17% of the total yield. And 75% of the product was obtained after 24 hours. In addition, COF-5 was found to crystallize more rapidly at temperatures above 30 °C. This rapid crystallization may be attributed to the elevated temperature, which promoted the crystallization of the reactants.

In addition to powdered crystals, the solvothermal method can also be utilized for the synthesis of thin films. In a study, the precursors 2,3,6,7,10,11-hexahydroxytriphenylene (HHTP) and 1,4-phenylene bis-boronic acid (PBBA) were subjected to solvothermal condensation with a solvent mixture of 1 ml mesitylene and 1 ml dioxane at 90 °C to form COF-5 thin films (Figure 2.1c).[18] The results revealed the presence of minimal bulk structures in the COF-5, demonstrating the successful synthesis of the films. In addition, the uniformity of the COF film interface with a thickness of approximately 94 nm was confirmed by measurement.

COF nanofibers can also be synthesized using the solvothermal method. Another study obtained a fiber-like COF by condensing the reactants 2,4,6-tris(4-aminophenyl)

pyridine (TAPP) and 2,6-Dihydroxynaphthalene-1,5-dicarbaldehyde (DHNDA) which were dissolved in anhydrous ethanol solvent and heated at 180 °C in a high-pressure reactor for two days (Figure 2.1d).[19] The synthesized fibrous COF exhibited a homogeneous strip structure with a length of approximately 10 μm and a diameter of around 0.8 nm. The formation of the nanofibers could be attributed to the solvothermal conditions, which promoted the reversible synthesis of imines, led to the dissolution and re-crystallization of the bulk product into fibrous structures.

In order to compare the effect of solvothermal methods and common synthetic methods with an open reaction environment on the crystallization of COFs, Kalidindi and coworkers synthesized COF-1 using both approaches (Figure 2.1e).[20] Initially, under the catalysis of a Lewis base, the reactants 1,4-dioxane and 1,4-benzenediboronic acid (BDBA) were condensed to form COF-1-NH_3, which was further purified by heating to obtain COF-1. Subsequently, the precursor was placed in a closed vessel and reacted at 150 °C to generate the product. The yield of the COF synthesized by the solvothermal method was 83%, which was higher than the yield obtained by the conventional method. This could be attributed to the requirement of high-temperature catalysis for the synthesis of COF-1, which was facilitated by the solvothermal method at relatively higher temperatures, enabling more precursors to be activated and converted into COF-1. Moreover, the vacuum environment in solvothermal synthesis prevented the oxidation of reactants so that the product obtained exhibits a higher degree of crystallinity.

While the solvothermal method has advantages in synthesizing COFs with high

crystallinity and large specific surface area, its limitations should not be overlooked. Firstly, the vacuum-sealed environment results in the reaction process and crystal growth cannot be followed and observed. Secondly, the reaction process is slow and time-consuming, typically requiring 3–7 days for solvothermal synthesis. Thirdly, the method demands high requirements equipment and is not suitable for large-scale production. Fourthly, the high temperature and pressure reaction conditions pose many safety risks.

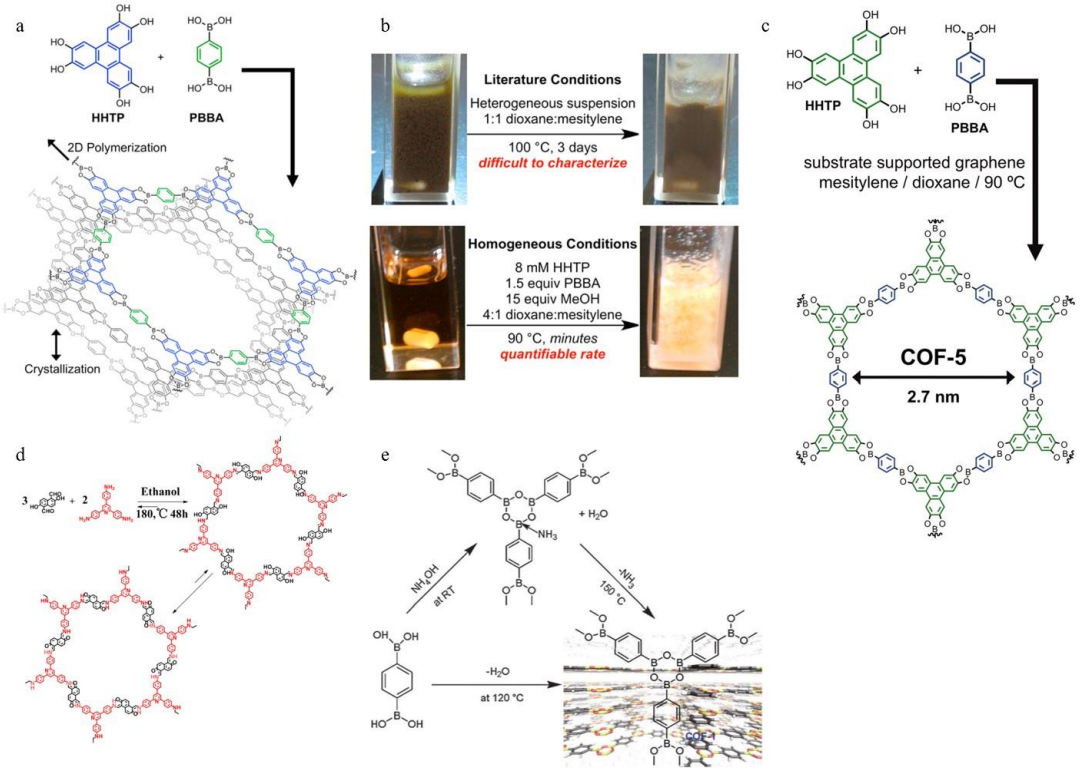

Figure 2.1. (a), The synthesis scheme of COF-5. (b), COF-5 synthesized under initial homogeneous conditions and by solvothermal synthesis, respectively.[17] (c), Schematic representation of COF-5 thin film.[18] (d), Synthesis of fibrous COF by condensation of DHNDA and TAPP.[19] (e), COF-1synthesized by normal condensation and ammonia-assisted solvothermal synthesis, respectively.[20]

2.1.2 Ionothermal synthesis

The ionothermal method is a technique for synthesizing COFs using ionic liquids or molten materials as solvents in an ionic state reaction environment. Unlike the solvothermal method, the ionothermal method can typically be conducted at atmospheric pressure. This effectively avoids the operational difficulties and safety hazards associated with high-pressure conditions. In the meantime, the required reaction time is significantly less than that required by the solvothermal method. In addition, the ionothermal synthesis offers advantages in the investigation of COF synthesis mechanisms. Moreover, it can also be easily combined with other synthesis methods, such as microwave-assisted synthesis, enabling synergistic effects for COFs production.

The utilization of ionic liquids (ILs) as solvents and catalysts for COFs synthesis has been extensively investigated. Specifically, 1-butyl-3-methylimidazolium bis ((trifluoromethyl) sulfonyl) imide ([BMIm][NTf_2]) has been employed as an IL catalyst to promote the condensation between reactants, leading to the synthesis of 3D-IL-COFs (Figure 2.2a).[21] In contrast to solvothermal methods, the IL-assisted synthesis can be completed within 12 hours, and the appearance of the product was observed within 3 minutes. The synthesized 3D-IL-COFs demonstrated excellent performance, particularly in terms of thermal stability, even at elevated temperatures of more than 450 °C. This may be due to the embedding of the IL in the pores of the COF structure, which imparted enhanced thermal stability.

Another ionic salt, $ZnCl_2$, has been explored as a catalyst for the synthesis of covalent triazine-based frameworks (CTFs) at high temperatures (Figure 2.2b).[22] This CTF exhibited a large specific surface area, high crystallinity, and a well-ordered pore

structure. This could be attributed to the enhanced solubility of aromatic nitriles in molten $ZnCl_2$. Moreover, $ZnCl_2$ promoted the cyclic trimerization of nitrile groups, leading to the formation of cyclic structures that enhance the stability of the CTF. In addition, $ZnCl_2$ improved the reversible reaction of nitrile cyclization, further facilitating CTF crystallization. The $ZnCl_2$ could be a catalyst in CTF synthesis has also been demonstrated in another study (Figure 2.2c).[23] $ZnCl_2$ promoted the dynamic polymerization reaction of the precursor 2,6-naphthalene carbonitride, resulting in the synthesis of porous CTF with a high specific surface area of 2255 $m^2 g^{-1}$ and excellent thermal stability. The exceptional specific surface area derived from the balanced pore structure, with micropores contributing 59% and mesopores contributing 41% of the total porosity. As well as the presence of mesopores enhanced the mass transfer rate and expanded the potential applications of the CTF.

In order to compare the effect of solvothermal and ionothermal methods on the synthesis of imide COFs, a method utilizing $ZnCl_2$-catalyzed crystallization of molten reactants had been reported (Figure 2.2d and e).[24] The synthesized polyimide-linked COF (PI-COF) exhibited high crystallinity and a large specific surface area of 1250 $m^2 g^{-1}$, which is comparable to COFs synthesized via solvothermal methods (1297 $m^2 g^{-1}$). The synthesis of PI–COF through the ionothermal method had several advantages. Firstly, no soluble reactants were required, which provided more flexibility in precursor selection. Secondly, the total reaction time was less than 10 hours, significantly lower than the 3–7 days required by the solvothermal methods. Thirdly, unlike the irreversible cyclization and condensation of imides in solvothermal reactions,[25] the product

synthesized via the ionothermal method experienced reversible synthesis, allowing for secondary repair and resulting in higher crystallinity. In the meantime, the ionothermal method eliminated the need for toxic solvents that are essential in solvothermal synthesis.[26] This made the reaction process safer and more environmentally friendly.

The ionothermal method, while presenting many advantages for COF synthesis, is constrained by the requirement of high temperatures (typically exceeding 400 °C). These elevated temperatures can lead to structural damage and collapse of frameworks and may also result in increased product decomposition. Consequently, only a limited number of building blocks can be successfully condensed by this approach. As a result, the application scope of the ionothermal method remains limited.

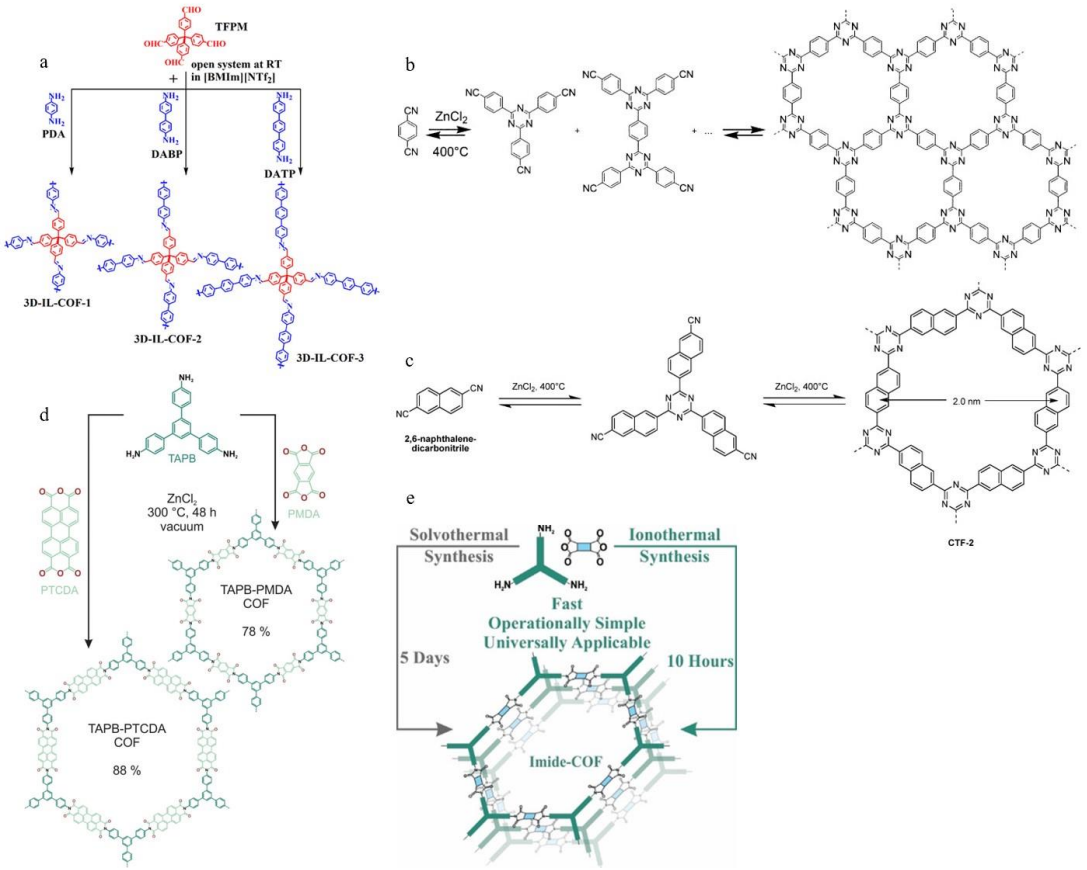

Figure 2.2. (a), Strategy for the Synthesis of 3D COFs by using [BMIm][NTf_2] as an ionic liquid solvent.[21] (b), The precursor catalyzed by the molten ionic liquid $ZnCl_2$ to polymerize into a covalent triazine framework (CTF-1).[22] (c), The condensation of 2,6-dicyanonaphthalene catalyzed by $ZnCl_2$ at 400 °C to CTF.[23] (d), Schematic comparison of imide COFs synthesized by solvothermal and ionothermal synthesis. (e) Synthesis of TAPB COFs by ionothermal synthesis in molten $ZnCl_2$.[24]

2.1.3 Microwave synthesis

The microwave method is an optimized approach derived from the solvothermal method. It retains the reaction conditions of solvothermal synthesis but significantly reduces the required reaction time, enabling the rapid synthesis of COFs with high crystallinity and porosity. Microwave synthesis of COFs offers several advantages. Firstly, it drastically reduces the reaction time, typically 1/200th of the duration required in solvothermal reactions. Secondly, it provides more uniform heating of the reactants, resulting in well-defined product structures.[27] Thirdly, it minimizes the formation of by-products and leads to higher yields of products.[28]

Campbell *et al.* reported the first microwave synthesis of boronic acid ester COF (COF-5).[29] Under solvothermal reaction conditions, the reaction vessel was placed in a microwave reactor operating at 200 W power and heated at 100 °C for 20 minutes. This synthesis method significantly reduced the reaction time compared to solvothermal synthesis, which typically takes more than three days. Meanwhile, the resulting COF-5 exhibited higher crystallinity and a larger specific surface area (2019 $m^2\ g^{-1}$) compared

to the products synthesized via solvothermal methods (1590 $m^2 g^{-1}$).

In order to compare the effects of the microwave method and solvothermal method on the synthesis of imine COF, Wei and group synthesized two enamine COFs (TpPa-COF-MW and TpPa-COF-CE) using these two methods.[30] Compared to solvothermal synthesis, which required a reaction time of 72 hours at 120 °C, microwave synthesis yielded the products in just 60 minutes at 100 °C. The TpPa-COF-MW synthesized by microwave method demonstrated a significantly higher yield of 83% compared to the solvothermal-synthesized TpPa-COF-CE with a yield of 60%. Additionally, TpPa-COF-MW exhibited a more diverse pore structure and a larger specific surface area of 725 $m^2 g^{-1}$ relative to TpPa-COF-CE (152 $m^2 g^{-1}$). In addition, the microwave-synthesized COF displayed higher crystallinity, potentially due to the ability of microwaves to promote the formation of C–N bond.

The microwave method also serves as an effective method for improving the ionothermal synthesis of triazine COFs. This approach offers shorter reaction times and lower required reaction temperatures. Therefore, the decomposition of the product that results from long reaction times at high temperatures in ionothermal synthesis can be avoided. The advantages of the microwave method in CTF synthesis have been demonstrated in a recent study.[31] The synthesis of COF at 110 °C and 200 W microwave power only required 30 minutes, and the appearance of the product was observed as early as 30 seconds. In the meantime, CTF-COF synthesized by microwave achieved a higher yield of 90% than that synthesized by ionothermal methods. Additionally, the products synthesized using this method exhibited enhanced crystallinity, which can be attributed

to the microwave's ability to prevent carbonization of the reactants and promote crystallization.

2.1.4 Sonochemical Synthesis

Sonochemical method is a rapid approach for the synthesis of COFs. By applying mechanical waves, the formation and collapse of bubbles in the solvent are accelerated. A localized high temperature and pressure condition were created, which thus accelerate the chemical reactions.[32] In addition to its short reaction time, sonochemical synthesis offers advantages such as low energy consumption and simple equipment requirements.[33] In addition, it allows for the avoidance of toxic organic solvents, making the process safer and more environmentally friendly.

Sonochemical synthesis was employed by Yang *et al.* to facilitate the rapid condensation of reactants for COFs.[34] Accelerated mixing of the reactants in the solvent at 50% ultrasonic power allowed the synthesis of COF at rates up to 387 K and required a reaction time of no more than 2h. Meanwhile, the products synthesized using this method exhibited a significantly larger specific surface area of 2122 $m^2 g^{-1}$, surpassing the surface area of solvothermal COF (1590 $m^2 g^{-1}$). This enhancement in the surface area could be attributed to the improved dissolution of poorly soluble components in the precursor facilitated by the sonication process.

A novel study presented a method for the synthesis of imine COFs in aqueous solution.[35] By employing sonochemical synthesis with the catalytic assistance of acetic acid in an aqueous medium, the reaction time required was significantly reduced to less

than 1 hour. The COFs synthesized using this approach exhibited a large specific surface area of 2059 m^2 g^{-1}, along with higher crystallinity and porosity compared to COFs synthesized *via* the solvothermal method. In addition, food vinegar has been identified as an effective catalyst for inducing the crystallization of reactants. This research introduced a green synthesis approach that replaced hazardous organic solvents with environmentally friendly aqueous solutions.

2.1.5 Mechanochemical synthesis

A mechanochemical method is an approach that facilitates the crystallization process by involving grinding the reactants in a mortar. This technique has several advantages, including simplicity and safety reaction apparatus and process, as well as fast reaction rates. These benefits make it an attractive approach for promoting the crystallization of reactants.

The first *β*-ketoenamine COF synthesized via the mechanochemical approach was achieved by manually grinding the reactants to promote the aldehyde-amine condensation reaction (Figure 2.3a).[36] The reaction was observed to commence after five minutes and completed within forty minutes. The resulting product, TpPa-1 (MC), exhibited a similar structure and stability to the solvothermal synthesized counterpart, TpPa-1 (ST). However, TpPa-1 (MC) demonstrated a significantly lower specific surface area of 61 m^2 g^{-1} compared to the 537 m^2 g^{-1} of TpPa-1 (ST). Additionally, the crystallinity and porosity of TpPa-1 (MC) were found to be inferior to the solvothermal synthesized product.

In order to overcome the limitations of mechanochemical synthesis and enhance its practicality in COF synthesis, a method assisted by an ionic liquid has been reported (Figure 2.3b).[37] The ionic liquid served as a catalyst to facilitate the contact between reactants as well as accelerate the reaction. And then promoted the crystallization of the product. The hydrazone-based COF (TpTh (LAG)) synthesized using this method exhibited higher yield and crystallinity. Furthermore, the crystallinity of TpTh (LAG) was maintained for over seven days in an acidic environment. This approach showed improved efficiency and stability in the mechanochemical synthesis of COFs.

The combination of ionothermal synthesis and mechanochemical synthesis can be further improved by applying a certain temperature to the reaction system (Figure 2.3c).[38] A ketenamine COF (TpPa-COF) was successfully synthesized by applying a temperature of 170 °C and utilizing an ionic liquid catalyst, p-toluenesulfonic acid monohydrate (PTSA-H_2O). The synthesis process was simple and could be completed in less than a minute. The resulting TpPa-COF exhibited high crystallinity and a large specific surface area of 3109 $m^2\ g^{-1}$, which far exceeded that of the product obtained through the original mechanochemical method and the counterpart obtained by the solvothermal method. The enhanced properties were probably due to the thermal assistance in reactant decomposition and improved molecular contact. Simultaneously, the catalytic effect of PTSA-H2O reduced defects during the synthesis process, resulting in highly crystalline products.

In addition to direct heating of the system, the utilization of high-temperature steam as an auxiliary in mechanochemical transformations has shown superior results. A study

reported the ability to synthesis of highly crystalline nanofiber COF through a solid-state grinding reaction with the assistance of a small amount of solvent steam at 120 °C (Figure 2.3d and e).[39] The steam-assisted mechanochemical processing accelerated the grinding process, leading to the formation of a significant number of mesh-like COFs after 48 hours. In contrast, only a few soluble polymers could be observed in the original mechanical grinding. Simultaneously, steam improved the crystallinity and structural ordering of the product, resulting in fibrous COFs that present a homogeneous and average diameter of approximately 65 nm.

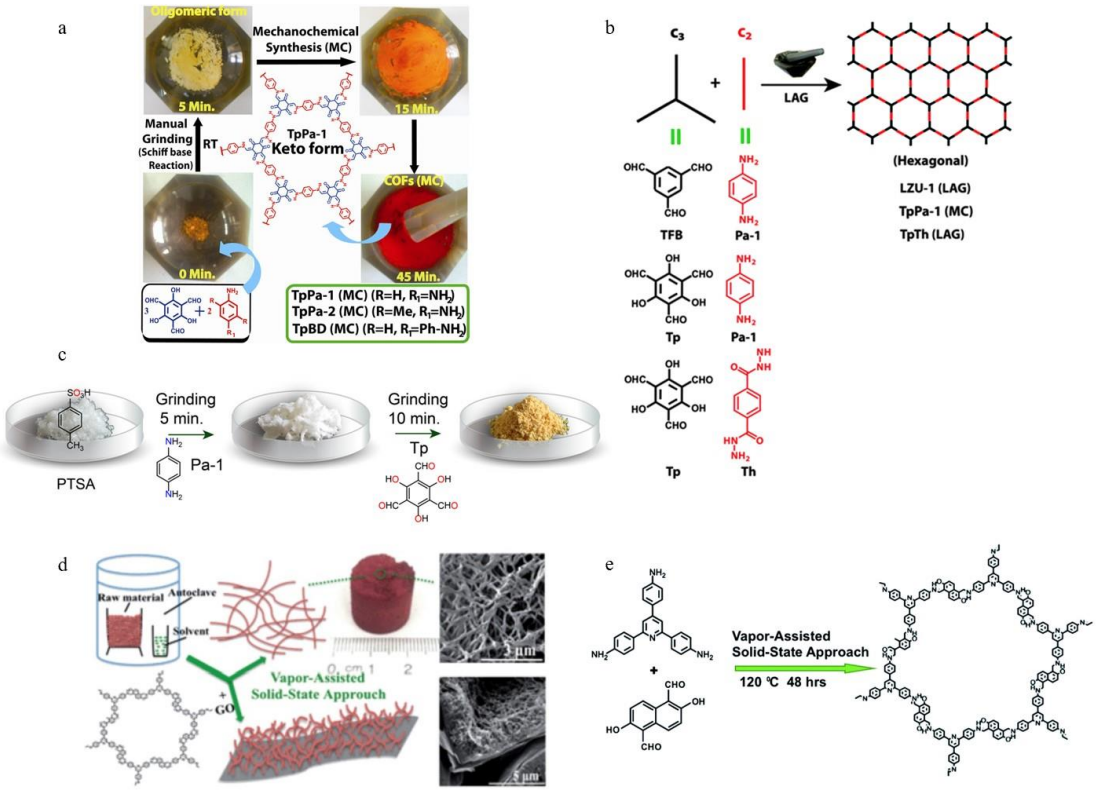

Figure 2.3. (a), Schematic representation of the fabrication of Schiff base condensation to TpPa-1 (MC) by grinding in a mortar and pestle.[36] (b), Schematic illustration of the synthesis of TpTh (LAG) by liquid-assisted grinding.[37] (c), The synthesis process of

TpPa-COF by ionic liquid synergistic mechanical grinding at 170 °C.[38] (d), The generation of fibrous COF by solid-state mechanical grinding with the aid of solvent vapor. (e), Reaction scheme for the synthesis of COF.[39]

2.2 Modification of COFs

2.2.1 Porosity

Porosity is a crucial parameter in COFs as it significantly impacts their performance. Micropores can provide a large specific surface area to facilitate increased contact between electrolyte ions and promote charge accumulation as well as improve specific capacitance. However, relying solely on micropores can lead to mass transport limitations, which can affect the chemical reactions taking place at the electrode. On the other hand, mesopores and macropores can offer unobstructed pathways for rapid ion transport.[40] Therefore, achieving a balanced pore structure in COFs is an important modification aspect. It can provide a larger contact area, facilitate fast mass transfer, enhance the interaction with active sites, and improve the performance of electrochemical devices.

Firstly, the pore structure and pore size of COFs can be designed and expanded by modifying the shape and length of the structural units. COF-300 was a porous crystalline crystal linked by imine bonds synthesized through the condensation of linear terephthalaldehyde and tetrahedral tetra-(4-anilino)-methane (Figure 2.4a).[41] It exhibited a large specific surface area of 1360 $m^2 g^{-1}$ and a pore structure with a pore size of 7.8 Å (Figure 2.4b). Furthermore, another novel porous COF, named COF-43,

with structural modules linked by hydrazone bonds, was obtained by the condensation of 2,5-diethoxy-p-phenylene terephthalhydrazide and 1,3,5-tris(4-formylphenyl) benzene (Figure 2.4c).[42] This COF displayed excellent crystallinity, a permanent porous structure with an average pore size of 38 Å as well as high stability (Figure 2.4d). Additionally, a rigid crystalline COF (COF-1) was reported. It was formed by the condensation of hexahydroxytriphenylene ($C_{18}H_6(OH)_6$) and benzene-1,3,5-triboronic acid ($C_6H_4[B(OH)_2]_2$) (Figure 2.4e).[4] COF-1 exhibited a large specific surface area of 711 $m^2\ g^{-1}$, indicating the presence of abundant micropores. Moreover, it possessed a wide range of pore sizes, ranging from 7 to 27 angstroms (Figure 2.4f). In addition, COF-1 demonstrated excellent stability, maintaining a stable morphology and pore structure even at temperatures as high as 600 °C. These findings highlighted that tailoring pore structures in COFs by manipulating the structural units is an effective approach of enhancing porosity.

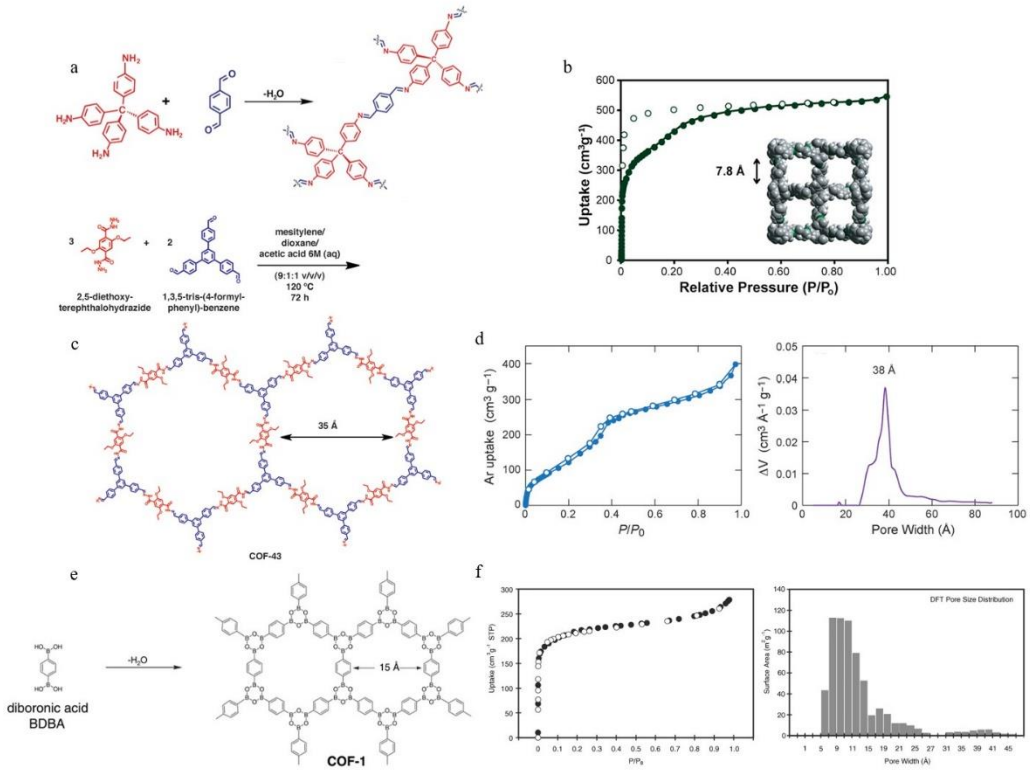

Figure 2.4. (a), The process and structure of COF-300 from precursor terephthaldehyde and tetra-(4-anilyl) methane. (b), Argon adsorption and desorption isotherm for COF-300 at 87 K. Illustration: Spatial model of the pore size distribution of COF-300.[41] (c), Schematic representation of the synthesis of COF-43 linked by hydrazone linkage. (d), The argon adsorption/desorption isotherm and the pore size distribution of COF-43.[42] (e), Schematic representation of the formation of COF-1 by condensation of boric acid. (f), The nitrogen adsorption/desorption curve and the histograms of the pore size distribution for COF-1 at 77 K.[4]

Secondly, the surface channels of COFs can be modified by the introduction of heteroatoms and functional groups. For example, the incorporation of carboxylic acid groups was investigated as a means to facilitate the conversion of mesopores to micropores within COFs.[43] The channels were functionalized by the ring-opening

reaction of the hydroxyl-containing precursor ([HO]x%-H_2P-COF) with succinic anhydride, resulting in [HO_2C]x%-H_2P-COF interconnected by ester linkages. The functionalized COF exhibited a type I nitrogen adsorption isotherm with pore size distribution, indicating the presence of microporosity compared to the typical mesoporous type IV profile shown by the precursor. In addition, [HO_2C]x% -H_2P-COF maintained its pore structure for 24 hours in acidic (1 M HCl), neutral (1 M $NaHCO_3$) and alkaline (1 M KOH) environments, demonstrating its excellent stability.

Finally, secondary pore engineering with the introduction of tunable mesopores and macropores in microporous-rich COFs can be used to increase their hierarchical porosity. Zhao and group[44] reported a strategy to create macropores with adjustable pore sizes in a microporous COF. The resulting macro-TpBpy with a micropore-macropore structure obtained by this method exhibited macropores with an average diameter of 270 nm. Nitrogen adsorption-desorption experiments revealed that the precursor TpBpy had a total pore volume of 0.381 $cm^3\ g^{-1}$ and displayed a typical type I adsorption isotherm, indicating that its porosity was provided by the micropores. The macro-TpBpy also exhibited a type I profile, but with an increased total pore volume of 1.273 $cm^3\ g^{-1}$. And unlike the precursor, whose nitrogen adsorption increased at low relative pressures, the functionalized COF showed higher nitrogen uptake values at high relative pressures, demonstrating that macroporosity had been successfully introduced. Furthermore, the macro-TpBpy exhibited a larger specific surface area, indicating that the macropores alleviated the diffusion limitations caused by the single micropores and led to more efficient mass transfer. In addition, when coordinated with metallic cobalt, macro-TpBpy

demonstrated excellent performance with a low overpotential of 380 mV at a current density of 10 mA cm^{-2} as an oxygen evolution reaction (OER) catalyst. This enhanced catalytic performance could be attributed to the facilitated diffusion provided by the macropores, allowing easier access of Co^{2+} to the active sites.

2.2.2 Electrical conductivity

The low electrical conductivity is a significant challenge of COFs. The rapid charge transport is essential for the contact of the active site. Therefore, the low electrical directly affects the electrocatalytic activity and the performance of the energy storage device. The conductivity of COFs can generally be modified in two strategies: enhancing the intrinsic conductivity of COFs and hybridizing them with highly conductive materials.

Firstly, the spatial structure within COFs can be designed. The charge transport can be enhanced by designing maximally overlapping electron orbitals or cyclized chemical bonds. And then, their own electrical conductivity can be improved. A study had shown that the complete cyclisation of aromatic rings was an effective method for the synthesis of COF-conjugated structures.[45] Therefore, an approach to enhance the conductivity of COFs by complete cyclisation of pyrazine rings was reported (Figure 2.5a and b).[46] This novel conductive COF (COF-DC-8) was formed by the cyclisation condensation of 2,3,9,10,16,17,23,24-octa-aminophthalocyanine nickel (II) and the tetraketone and octaamine conjugate units of pyrene-4. It exhibited an excellent bulk conductivity of 2.51×10^{-3} S m^{-1}. This may be because the fully conjugated energy band structure in

COF-DC-8 could enhance the intrinsic conductivity of COF by facilitating rapid planar charge movement through cyclized aromatic chemical bonding.

Another work demonstrated a COF that exhibited high electrical conductivity by designing the topology of the structural units (Figure 2.5c and d).[47] JUC-518 with a non-interpenetrating pts network was synthesized through the hybridization of a highly conductive tetrathiafulvalene (TTF) unit and a tetrahedral structure of 1,3,5,7-tetraaminoadamantane (TAA) unit. This rare topology provided JUC-518 with a high conductivity of 1.4×10^{-2} S cm^{-1}. In the meantime, unlike the interpenetration structure that exhibited mainly microporosity, the non-interpenetrating network was more conducive to the formation of large pores that provide fast transport channels. In addition, the TTF structure could be doped with conductive materials to further improve the conductivity of the JUC-518.

Although the conductivity of COFs can be enhanced by designing the topology, the results are still not as good as expected. And the designed out of a fixed topology can also affect the diverse structural functions of COFs. Therefore, other highly conductive materials (graphene, conductive polymers, carbon nanotubes, etc.) can be introduced into COFs to enhance the conductivity of the composites.

It has been shown that films of COFs with lower thicknesses have more satisfactory electrical conductivity. Firstly, the layered structure of the films promotes self-exchange of electrons, which improves the conductivity. Second, thinner films contain less resistance and faster charge transfer. Finally, dopant materials with high electroactivity are more easily exposed in thinner electrodes, thus providing a fast response.[48] In order

to improve the practicality of thin film electrodes, Mulzer *et al.* presented a method for producing highly conductive films with a thickness exceeding 1 μm (Figure 2.5e).[49] By introducing 3,4-ethylenedioxythiophene (EDOT) into a COF containing redox-active functional groups, 3,4-ethylenedioxythiophene (PEDOT) was found to polymerize and propagate in the pores of COF and to be transported into its backbone as well as create a conductive network throughout the framework. The resulting PEDOT facilitated the connection between the COF and the redox active groups, thus significantly enhancing the charging efficiency of the electrode up to 1600 C which was ten times higher than that of unmodified electrode (Figure 2.5f). Simultaneously, the composite electrode exhibited excellent stability, maintaining its maximum capacitance even after 10,000 charge-discharge cycles.

Another study for oxygen reduction reaction (ORR) electrocatalysts showed that the efficient charge transfer within catalyst materials is crucial for enhancing their catalytic activity.[50] By doping with graphene, a highly conductive composite COP-P-SO_3-Co-rGO exhibited a high electrical conductivity of 2.56×10^{-1} S m^{-1}, which was seven times higher than that of the non-functionalized precursor. Meanwhile, COP-P-SO_3-Co-rGO demonstrated a half-wave potential of 150 mV and a Tafel slope of 66 mV dec^{-1}. In addition, the catalysts showed excellent stability in a 0.1 M KOH alkaline electrolyte with almost no loss in cathodic current density after more than 3000 charge/discharge cycles. Excellent conductivity and ORR performance came from the incorporation of graphene. The precursor COP provided abundant active sites, while graphene facilitated fast electron transport. Their synergistic effect could help better binding of electrons to

the active sites, thus improving the ORR activity of the catalyst.

In addition, another approach is to integrate electron-donating groups into the backbone of COFs. Yu yu's team used porphyrin, an electron-donating group with a large π-bond, as a monomer, The conjugated COF (TA-Por-sp^2-COF) consisted of two interconnected structural units, porphyrin and triazine, was formed by cyanine autopolymerisation. The porphyrin moiety had strong electron-donating properties, while the triazine ring exhibited excellent electron-withdrawing ability. The synergistic effect of these two groups could promote carrier separation and migration, thus achieving the enhancement of COF conductivity.

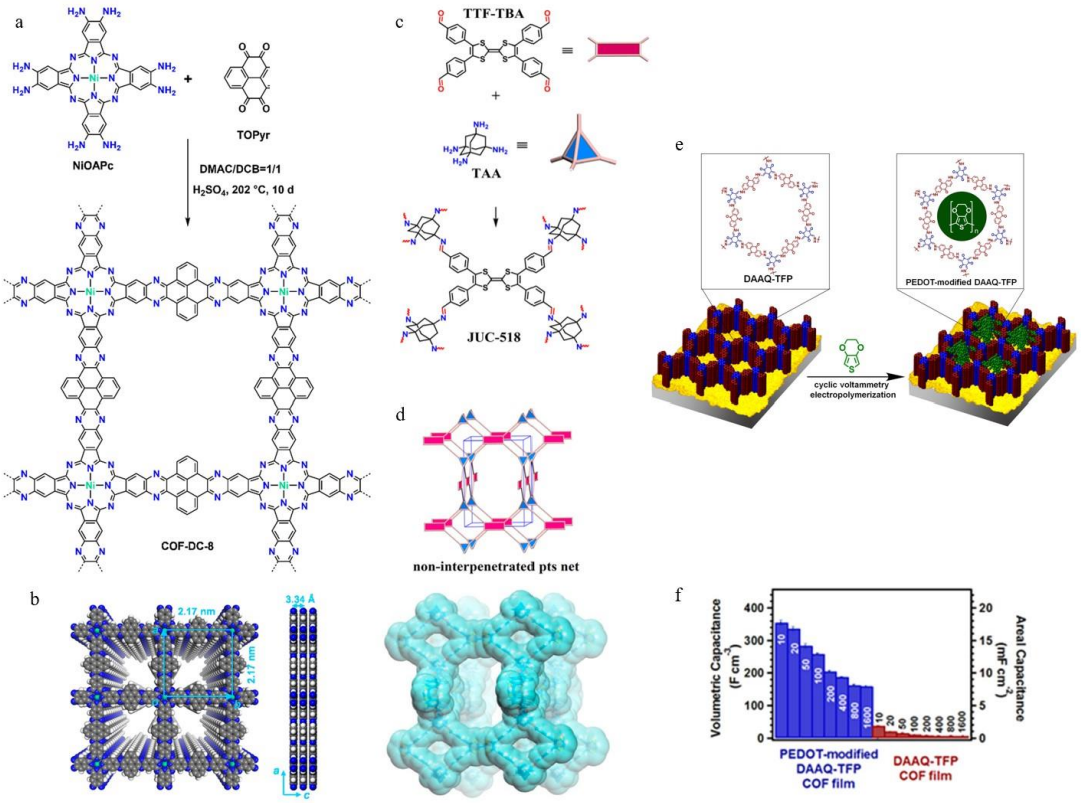

Figure 2.5. (a), Synthetic route to COF-DC-8 linked by pyrazine rings. (b), Schematic diagram of the structure of the COF-DC-8 with a fully conjugated network using square-

overlapping stacks.[46] (c), Schematic diagram of the synthesis strategy for JUC-518. (d), Structure of JUC-518 with a non-interpenetrating pts network.[47] (e), Schematic representation of the structure of thin film COFs before and after 3,4-ethylenedioxythiophene (EDOT) modification. (f), The capacitance of the original COF electrode and the PEDOT-modified film electrode tested by galvanostatic charging and discharging experiments at different scan rates.[49]

2.2.3 Crystallinity

Crystallinity is a crucial characteristic of COFs and is determined by the presence of local defects and disorders. It is also closely linked to the porosity.[51] While the crystallinity of COFs can be repaired and improved through reversible chemical transformations based on their synthesis principles, the achieved outcomes have been far from ideal.

Therefore, a strategy for enhancing the crystallinity of COFs can be explored by investigating their interlayer stacking modes and topological design. One work observed that the stacking modes of COF layers could be manifested as vertical AA stacking or shifted AA stacking (Figure 2.6a).[52] Vertical AA stacking was less stable and exhibited lower crystallinity. In contrast, COFs with inclined or serrated shifted AA stacks tend to displayed higher crystallinity. These COFs also exhibited superior pore structures and larger specific surface areas. Another study demonstrated that COF-1 synthesized using the interlocking hexagonal ring stacking mode exhibited a higher degree of crystallinity due to the presence of more disordered defects (Figure 2.6b).[53] This behavior may be

attributed to the van der Waals forces between COF layers, favoring the shifted AA stacking mode as the optimal arrangement for π orbitals.

The second method is to design a junctional approach connected by reversible covalent bonds. This approach promotes the repair and secondary crystallization of non-crystalline defect regions in COFs that do not crystallize following dynamic chemistry, thus improving their overall crystallinity. Xu *et al.* published a study on a benzene-based COF (TPB-DMTP-COF), in which methoxy groups were introduced as connectors between the benzene moieties (Figure 2.6c).[54] The embedding of methoxy groups provided off-domain lone pairs of electrons, thus enhancing the interlayer interactions between the COF layers and reducing the polarization effects of repulsion. PXRD plots (Figure 2.6d) of TPB-DMTP-COF revealed six distinct peaks, demonstrating its excellent crystallinity. Simultaneously, this COF exhibited a large specific surface area of 2105 m^2 g^{-1}. In addition, TPB-DMTP-COF demonstrated remarkable stability, maintaining its structure and morphology even under high temperatures and strong acid and alkaline conditions.

Intramolecular hydrogen bonds (–OH) can also be formed in COFs by introducing hydroxyl groups. One study proposed that the introduction of -OH between [–C=N] units produced hydrogen bonds and then anchored the benzene rings in the same plane.[6a] This planarity reduced the presence of disordered structure and thus facilitated COF stacking. In the meantime, the resulting COF exhibited a significantly increased specific surface area of 1305 m^2 g^{-1}, three times that of the precursor without the introduction of hydroxyl groups. The increased surface area signified an improvement in porosity, which

was also attributed to the hydrogen bonding. In addition, the intramolecular hydrogen bonding enhanced the stability of the COF, maintaining its porosity and crystallinity in 3 N HCl for more than seven days. A similar result was demonstrated in another work.[55] An interlayer hydrogen bond was formed by introducing DHPh between porphyrin units. This hydrogen bonding inhibited the indeterminate morphology of COF structural units so that they were locked into the same plane. This mitigated the repulsive forces that hindered COF stacking and extended the delocalized space. Simultaneously, as more DHPh groups were introduced, additional hydrogen bonding sites were created. The functionalized COF exhibited a maximum specific surface area of 916 m^2 g^{-1} compared to the 186 m^2 g^{-1} that the precursor possessed. This demonstrated the beneficial effect of hydrogen bonding on improving COF porosity.

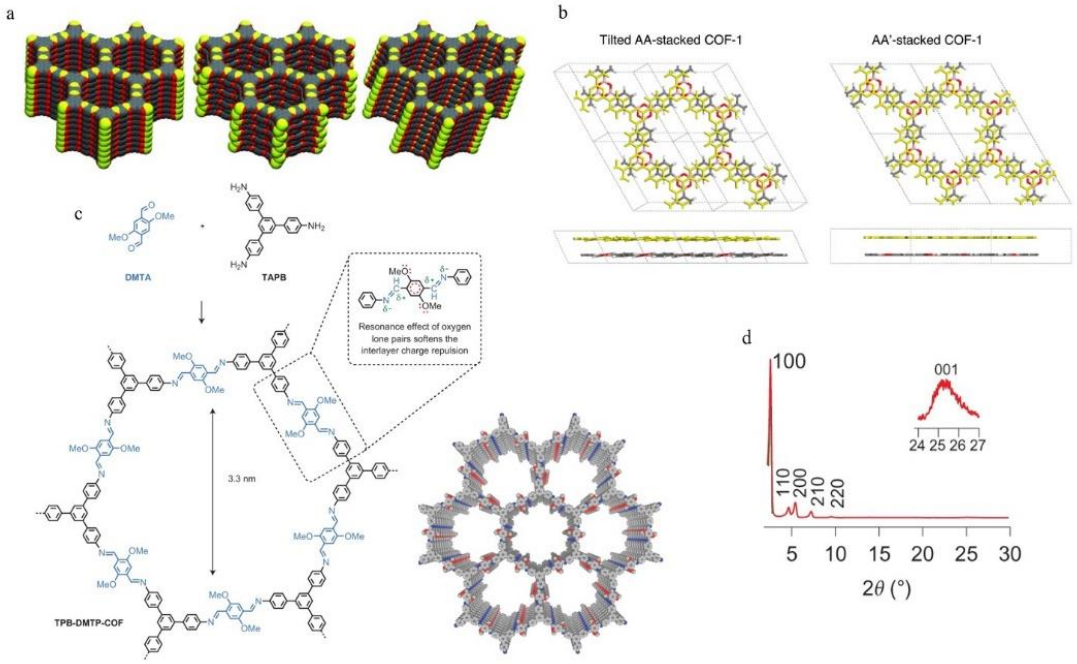

Figure 2.6. (a), Stacking patterns of COFs. Left: vertical AA stacking, middle: serrated shifted AA stacking, and right: inclined shifted AA stacking.[52] (b), Structural schematic

of the tilted AA-stacked COF-1 and the AA′-stacked COF-1.[53] (c), Synthesis method and structure of TPB-DMTP-COF. (d), The PXRD pattern of TPB-DMTP-COF with six diffraction peaks.[54]

2.2.4 Solvent induction

The solvent is also an important factor in the crystallinity of COFs. One study suggested that acetic acid could facilitate the synthesis of imine COFs by promoting condensation between amines and aldehydes.[56] Nonetheless, the effectiveness of acetic acid as a catalyst for the crystallization of COFs fell far short of expectations. The resulting COF exhibited lower crystallinity and specific surface area, not surpassing half of the theoretical values.[57]

Additionally, sulphonic acids can also be employed as catalysts for imine COFs synthesis.[58] By introducing *p*-toluene sulphonic acid into the amine, intermolecular hydrogen bonds were thus formed between the nitrogen atom of the amine and the oxygen atom of the acid. The COF exhibited maximum crystallinity and an excellent specific surface area of 969 $m^2\ g^{-1}$ when the hydrogen bond length ranged from 2.06 to 2.19 Å. In the meantime, the reversible reaction between sulphonic acid and amine slowed down the formation of imines, thus promoting the reversibility of COF synthesis and maximizing crystallinity. However, the distance of the hydrogen bonds was a crucial factor affecting COF crystallization. Excessively long distances could hinder imine bond formation and thus impact COF formation. Whereas the excessively short hydrogen bonds led to a rapid synthesis, slowing down the achievement of secondary

crystallization through reversible synthesis.

Furthermore, Lewis acids can act as catalysts for boronic ester-based COFs. A study discovered that the Lewis acid $BF_3 \cdot OEt_2$ catalyzed the conversion of acetone to catechol.[59] The generated catechol is condensed with cyclic boroxane, obtained from boric acid dehydration, to form the boronic ester-based COF. COF-5 exhibited a large specific surface area of 1670 $m^2\ g^{-1}$ and high porosity. However, the catalytic effect of Lewis acids required fast reaction kinetics to achieve the desired COF properties.

In addition to the acid that can act as a catalyst, an alkaline isoquinoline solvent can also effectively catalyze the formation of imide COFs.[26] Compared to the synthesis process without a catalyst, isoquinolines could modulate the dissolution rate of the precursor and the reversible conversion of imines. This modulation promoted the closure of imine rings and successfully transformed failed amorphous products into Imine COFs. The synthesized COF exhibited a high crystallinity and a large specific surface area of 2346 $m^2\ g^{-1}$. However, the amount of solvent and the temperature of the reaction during the catalytic process needed to be precisely designed.

2.2.5 Functionalized modifications

For COFs materials, in addition to designing and modifying their inherent properties such as porosity, periodicity and conductivity, they are also functionally modified according to their specific needs in electrochemical applications. Examples include the embedding of functional groups and the control of the number of redox-active sites. The incorporation of redox-active group plays a crucial role in electrochemical energy

storage applications, especially for supercapacitors. This is because they can provide pseudocapacitance through redox reactions, which significantly increase the capacitance of supercapacitors. Furthermore, coordination with metal atoms has been widely used in electrocatalysis.

DeBlase *et al.* reported functionalizing a two-dimensional COF (DAAQ-TFP COF) with redox-active groups 2,6-diamino anthraquinone (DAAQ).[60] The modified COF exhibited a significantly increased maximum specific surface area of 1800 $m^2 g^{-1}$, which was much larger than that of the unmodified one and approached the theoretical Connelly surface area of 2340 $m^2 g^{-1}$ for the first time. The enhanced surface area provided a larger charge storage capacity, facilitating the storage of more charges. Simultaneously, the DAAQ group contributed to pseudocapacitance during redox reactions. As a result, supercapacitors assembled with the modified COFs as electrode materials exhibited higher specific capacitance and demonstrated excellent stability during 5000 charge-discharge cycles in acidic electrolytes.

The periodic and well-defined structure of COFs provides regular metal coordination sites, which are crucial for incorporating metal complexes required in electrocatalysts. Moreover, the arrangement of catalytic structures within the COF building blocks can be controlled and designed.[5] In addition, the presence of heteroatoms and functional groups in COF structures can exhibit synergistic effects with coordinated metals, further enhancing the functionality or stability of electrocatalysts. Lin *et al.* utilized the internal π–π stacking interactions to synthesize and optimize a COF electrocatalyst (COF-366-Co) with a reticulated cobalt porphyrin structural unit connected through strong covalent

bonds.[61] The optimized catalyst exhibited an overpotential of –0.55 V in a neutral electrolyte, showing a 26-fold enhancement in activity compared to the unfunctionalized precursor. At the same time, it demonstrated an excellent Faradaic efficiency of 90%. In comparison to conventional cobalt porphyrin molecules, the cobalt porphyrin units within COF-366-Co exhibited a 10% increase in selectivity towards carbon dioxide and maintained high catalytic activity for more than a day. The high selectivity and activity can be attributed to the site isolation effect arising from the electronic structure of cobalt and the COF framework.

2.2.6 Structural modifications

Functionalized modification is a distinct strategy based on the COF structures and employed to improve COFs and expand their application range by introducing functional modules and achieving direct transformations. However, this linkage and the new functional groups selected are inherently limiting. On the other hand, structural modification refers to the direct transformation of COF skeleton to achieve the maximum repair and calibration of COFs according to the chemistry theory of reversible chemical synthesis of COFs.[62]

The limited stability of COFs remains a primary drawback that seriously hinders the lifespan and practical utility of the assembled electrochemical devices. In order to improve the stability, Haase's group proposed a method for the conversion of COFs linked by imines (TTI-COF) to COFs linked by thiazoles (TTT-COF) via sulphation (Figure 2.7a).[63] The direct transformation of imines to amides is attributed to the

reversible synthesis of COFs (Figure 2.7b).[64] The sulphated COF retained the topology, porosity, and crystallinity of the precursor. However, its specific surface area increased from 1362 m^2 g^{-1} of the precursor to 1431 m^2 g^{-1}. Unlike the randomly stacked TTI-COF, the structure of TTT-COF exhibited greater symmetry and larger interlayer spacing. These structural features contributed to the weakening of van der Waals forces between COF nanolayers and prevented undesired stacking. Furthermore, TTT-COF demonstrated superior stability against electron beam irradiation and chemical degradation, highlighting its enhanced electronic and chemical stability compared to TTI-COF.

In another study, a novel COF named MF-1a is reported, wherein the dynamic imine linkages were transformed into more stable quinone connections (Figure 2.7c).[65] MF-1a exhibited exceptional stability even under extreme chemical conditions. It maintained its morphology for more than 72 hours in 98% TfOH acid, 24 hours in 14 M NaOH strong base, 24 hours in $KMnO_4$ strong oxidizing agent, and 24 hours in $NaBH_4$ strong reducing agent (Figure 2.7d). This remarkable stability suggested that incorporating quinone units in the COF framework leads to improved structure preservation. Additionally, MF-1a retained the pore size and crystallinity of the precursor. However, the precursor experienced a significant loss of over 80% in specific surface area after acid/base treatment. MF-1a, on the other hand, still maintained a porous structure with a reduction in specific surface area of no more than 25%. This further emphasized that aromatic frameworks connected by quinone linkages exhibit superior chemical stability compared to imine bonds.

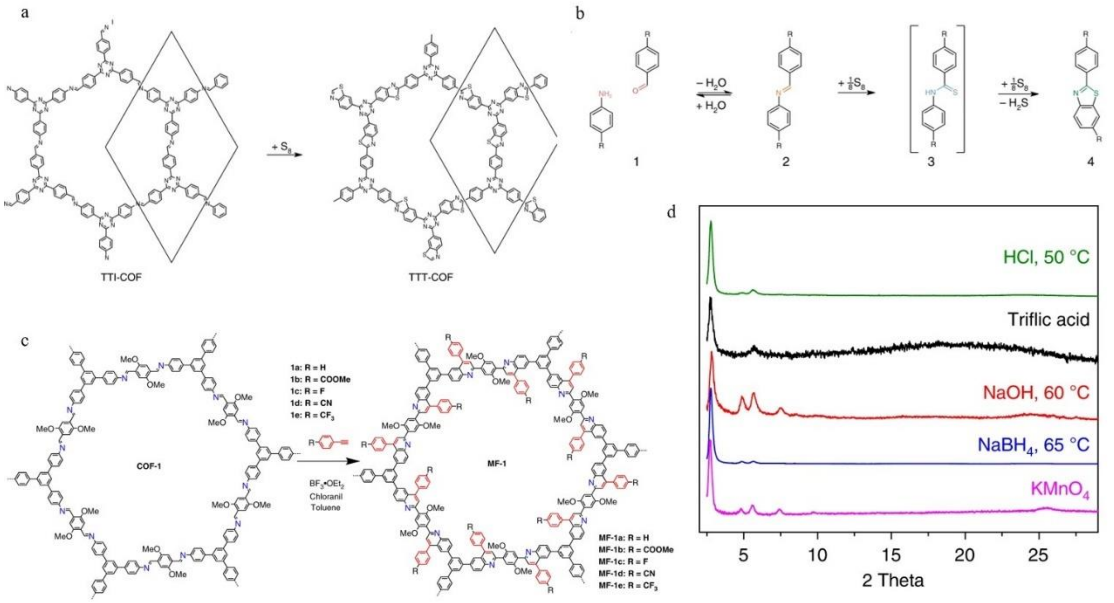

Figure 2.7. (a), Synthetic strategy for the conversion of TTI-COF linked by imine bond to TTT-COF linked by thiazole bond through sulfation. (b), Schematic representation of the direct conversion of an imine group to a thiazole group in the presence of elemental sulfur.[63] (c), Schematic representation of the synthesis of the conversion from a dynamic imine-linked COF to an amide-linked COF with higher stability. (d), The durability of MF-1a in strong mineral acid, ultra strong acid, strong base, strong oxidant and strong reducing agent.[65]

2.3 Electrochemical applications of COFs

The unique properties of COFs, such as large specific surface area, tunable frameworks, and ordered pore structures, make them promising candidates for advancing the field of electrochemistry and unlocking new opportunities for sustainable energy technologies.[66] The large specific surface area of COFs provides an increased contact

interface, facilitating the exposure of a greater number of active sites. Moreover, the ordered pore structure enables efficient transport of electrolyte ions. In addition, the high stability of COFs contributes to a prolonged electrode lifespan. As a result, COFs demonstrate excellent potential as electrodes in various electrochemical applications, including oxygen reduction reaction (ORR), oxygen evolution reaction (OER), and hydrogen evolution reaction (HER), as well as in electrochemical energy storage systems such as batteries and supercapacitors.

2.3.1 Electrocatalysis

COFs utilized for electrocatalysis exhibit distinctive characteristics which contribute to their effectiveness in catalytic applications. Firstly, their large specific surface area and high pore volume provide a large number of catalytic sites, enabling efficient connection with reactants. Secondly, COFs possess remarkable thermal and chemical stability, ensuring their durability and long lifetime under different reaction conditions. Thirdly, the ordered and designable skeletons of COFs facilitate the effective mass transfer, enhancing the accessibility of ions to catalytic sites. As a result, COFs have been directly employed as electrode materials for electrocatalysts.

Meanwhile, they can be coordinated with transition metals which possess catalytic properties as they can anchor metals within COF frameworks and provide metals with a well-defined spatial environment. The unique structure and characteristics of COFs and the synergistic combination with catalytically active metals, hold significant potential in the advancing electrocatalytic systems. Therefore, they have been used to control and

enhance catalytic performance for diverse applications precisely.

2.3.1.1 Water splitting

Water splitting is a chemical process that involves the cleavage of water molecules, resulting in the generation of two hydrogen atoms through the hydrogen evolution reaction (HER) and one oxygen atom through the oxygen evolution reaction (OER)[67]. To mitigate the overpotential caused by contact and solvent resistances, electrocatalysts are crucial in facilitating the two processes of water splitting. The performance of electrocatalysts can be evaluated using various indicators such as Tafel slope, Faradaic efficiency, and stability.[68] The Tafel slope represents the linear relationship between overpotential and current density. It is used to assess the overpotential of different catalysts at the same current density, thereby reflecting their performance. Generally, a smaller Tafel slope indicates a faster increase in current density with decreasing overpotential, indicating better catalytic performance. In addition, faradaic efficiency compares the theoretical and actual values of hydrogen or oxygen evolution to assess the practical catalytic efficiency of the catalyst. The stability of a catalyst determines its practical utility, as a more stable catalyst exhibits a longer lifetime and can be applied in practical applications.

COFs have demonstrated their potential as direct catalysts for water splitting. Ma and colleagues reported a catalyst (JLNU-302) formed through solvothermal condensation of 2,2'-dithiophene-5,5'-dicarboxaldehyde (bTDC) containing thiophene moieties and 2,4,6-Tris(4-aminophenyl)-1,3,5-triazine (TAPT) containing triazine groups (Figure 2.8a).[69] This COF catalyst exhibited excellent catalytic performance in alkaline

electrolytes. It demonstrated a low overpotential of 91 mV and a small Tafel slope of 103.88 mV dec^{-1} at a current density of 10 mA cm^{-2} (Figure 2.8b). These remarkable characteristics could be attributed to the high conductivity of the thiophene units, which promoted the rapid movement of electrons and thus enhanced the catalytic performance for HER. Furthermore, JLNU-302 had outstanding chemical stability, maintaining its structure and catalytic activity for more than 72 hours in strong acid and strong base environments.

Another study showed the potential of thiadiazole-based COFs as catalysts for OER (Figure 2.8c).[70] The electrocatalyst (C_4-SHz COF) synthesized through the condensation of 2,5-dihydrazinyl-1,3,4-thiadiazole (SHz) and 1,3,5-tris(4-formylphenyl) benzene (C_4-CHO), exhibited a large specific surface area of 1224 m^2 g^{-1} and high crystallinity. Additionally, it demonstrated excellent OER catalytic performance, with an overpotential of 0.32 V and a small Tafel slope of 39 mV dec^{-1} at a current density of 10 mA cm^{-2} (Figure 2.8d). The superior catalytic performance came from the large contact surface of active sites resulting from the high specific surface area and efficient mass transfer facilitated by the ordered framework. In addition, the C_4-SHz COF had remarkable cycle life and could maintain stable catalytic performance at high current densities for over 10 hours.

An alternative approach in electrocatalysis is the integration of COFs with metal coordination ligands. The large specific surface area of COFs can provide abundant metal active sites, while the rich pore structure can offer efficient pathways for mass transport. Furthermore, the ordered framework facilitates the anchoring of metals.

Additionally, COFs can be effectively combined with relatively inexpensive transition metals to replace the currently used catalysts based on noble metals, which exhibit superior catalytic performance but are limited by their low abundance.

As a macrocyclic complex with a conjugated network, the porphyrin groups are highly suited as a coordination structure for the metal inside the COFs.[71] Firstly, the macrocyclic structure of the porphyrin provides a fixed coordination environment for metals, thereby enhancing the stability of the catalyst. Secondly, the rich redox active sites of porphyrin moiety can provide multiple proton transfer catalysis. Thirdly, the functionalization of porphyrin groups allows for a tailored performance suitable for specific applications. Therefore, Wu *et al.* developed a cobalt porphyrin electrocatalyst (CoTcPP-1), which exhibited excellent electrocatalytic performance in acidic electrolytes.[72] This catalyst achieved a current density of 10 mA cm^{-2} with a small overpotential of 475 mV in a 0.5 M H_2SO_4 electrolyte. This indicated the enhanced HER efficiency attributed to the metal-porphyrin coordination structure. This might be due to its large surface area of 441.74 m^2 g^{-1}, which could provide a greater number of catalytically active sites. Additionally, CoTcPP-1 displayed a low Tafel slope of 197 mV dec^{-1}, indicating fast catalytic kinetics. Moreover, this catalyst demonstrated high stability, maintaining its structural integrity and catalytic performance for more than 10 hours in acidic conditions.

Porphyrin groups with $M–N_4$ structures also find applications in the catalytic process of OER. Liu *et al.* reported a copper porphyrin COF (Complex 1) that exhibited excellent OER catalytic activity in neutral electrolytes.[73] This catalyst achieved an overpotential

of 0.31 V at a current density of 0.10 mA cm^{-2}. In the meantime, it demonstrated a Faradaic efficiency of over 93%. Additionally, Complex 1 maintained a stable oxygen evolution current even after constant potential electrolysis at 1.30 V_{RHE} after 10 hours, highlighting its long-term stability in OER applications.

The utilization of metal combined with other coordination units as catalysts in catalyzing water-splitting reactions has shown promising potential. Phthalocyanines are metal-organic complexes with a macrocyclic structure similar to that of porphyrins. Due to their abundance of active sites, excellent stability and metal anchoring capabilities, phthalocyanines can be used as excellent coordination ligands.[74] In a recent study, copper phthalocyanine (CuPc) was investigated as a catalyst for promoting hydrogen resolution in water.[75] In an acidic electrolyte, the overpotential of the ligand was reduced from –1.26 V to –1.30 V at the same current density by comparison with an unmodified electrode. This reduction could be attributed to the synergistic effect of the unique complex deposition phenomenon in phthalocyanines and the enhanced catalytic activity of $[CuPc]^{-}$ or $[CuPc]^{2-}$ in proton electroreduction.

Bipyridine structures have been found to exhibit metal coordination capabilities and catalyze the OER. Aiyappa and colleagues presented a cobalt bipyridine-based catalyst named Co-TpBpy and synthesized through the condensation of 2,2'-bipyridine-5,5'-diamine (Bpy) and 1,3,5-triphenylbenzene-1,3,5-triol (Tp) into a coordination framework.[76] This COF demonstrated a large surface area of 450 m^2 g^{-1}. Moreover, it exhibited an overpotential of 0.4 V at a current density of 1 mA cm^{-2}. Notably, it displayed an ultra-low Tafel slope of 59 mV dec^{-1} and a high Faradaic efficiency of 95%.

These data suggested that the bipyridine moieties as coordinating ligands to cobalt contributed to the excellent OER catalytic performance, which is potentially due to its abundant porous structure and coordinating motifs within the skeleton. Additionally, Co-TpBpy had remarkable stability. After 1000 cycles in a neutral electrolyte, its structure and activity were retained by more than 90%.

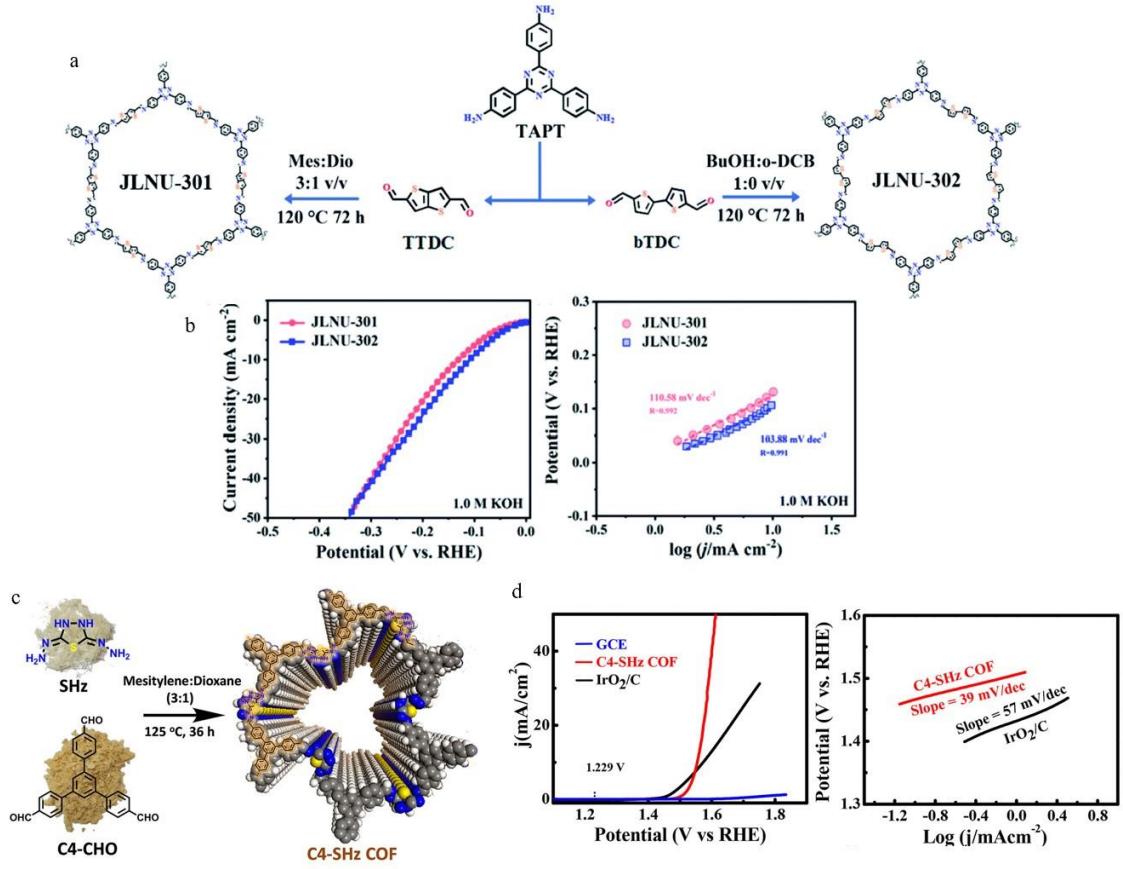

Figure 2.8. (a), Synthesis and structure of thiophene COF as an HER catalyst. (b), HER performance test of JLNU-COFs in alkaline electrolytes. (LSV polarization curves and Tafel plots)[69] (c), Synthetic strategy and schematic structure of thiadiazole COF as an OER catalyst. (d), OER polarization curves and Tafel plots of C_4-SHz COF and precursors at 1 M KOH at a scan rate of 5 mV s^{-1}.[70]

2.3.1.2 Oxygen Reduction Reaction (ORR)

ORR is a crucial energy conversion process in fuel cells, and the overall efficiency of the device is severely limited by the lack of efficient ORR catalysts. The evaluation of ORR catalysts can be assessed through several key aspects. Firstly, the onset potential and half-wave potential are the primary performance indicators to determine when the chemical reaction initiates. Secondly, the diffusion limiting current density (DLCD) represents the current that can pass through a unit area within a given time, indicating the kinetics of the reaction. A higher DLCD, therefore, indicates a reaction system with faster kinetics. Thirdly, ORR generally involves two transfer pathways: the $4e^-$ process from O_2 to H_2O and the $2e^-$ process from O_2 to H_2O_2. However, the four-electron transfer in fuel cells provides higher power output, making catalysts that promote the $4e^-$ pathway more desirable. Fourthly, the Tafel slope is also an important evaluation parameter. A lower Tafel slope indicates lower overpotential at the same current density, thus demonstrating better catalytic activity. Fifthly, the stability and durability of the catalyst determine its lifetime and suitability for long-term use.

Currently, COFs have been used directly as catalysts for ORR. COFs have been used directly as catalysts for ORR. A polychlorotrityl COF (PTM-H-CORF) which was highly active and durable as well as containing a π-conjugated system, has been reported (Figure 2.9a).[77] Its performance was evaluated in an O_2-saturated 0.1 M KOH electrolyte using Rotating Ring Disk Electrochemistry (RRDE) (Figure 2.9b). This catalyst exhibited remarkable reduction activity within the potential range of –300 mV to –180 mV. Simultaneously, it demonstrated a half-wave potential of –270 mV and a

total electron transfer number of 3.89. Moreover, PTM-H-COF displayed excellent durability, maintaining stable performance for more than 10 hours and a loss of current density of no more than 15%.

COFs, in coordination with metals, have gained widespread attention as catalysts for ORR. Among them, the porphyrin macrocycle structure has been extensively used to anchor O_2 within the metal and facilitate oxygen reduction due to its metal coordination sites. A study focused on the ORR activity of iron porphyrin complexes was reported.[78] This catalyst exhibited an onset potential of 0.93 V and a half-wave potential of 0.84 V at a current density of 0.1 mA cm $^{-2}$. Furthermore, it demonstrated a shift of 0.16 V in the half-wave potential, indicating the promotion of ORR by the porphyrin macrocycle structure. It also exhibited a total electron transfer number of 3.97. Moreover, this COF showed excellent durability, with a performance loss of less than 6% after 1000 cycles at high current density. Another study highlighted the high activity of cobalt porphyrin as an ORR catalyst.[79] The catalyst Co (TCPP) had a high onset potential of 300 mV and demonstrated significant reduction activity near –300 mV. In addition, it displayed excellent H_2O_2 selectivity, with a maximum H_2O_2 generation of 3.4×10^{-8} mol.

Sun and colleagues conducted an analysis of the ORR activity of two metal-porphyrin coordination complexes.[80] The Co-porphyrin exhibited high ORR activity, but it showed a preference for the $2e^-$ transfer pathway, leading to the generation of H_2O_2. On the other hand, the Fe-porphyrin demonstrated higher selectivity for the $4e^-$ oxygen reduction pathway, enabling direct reduction of O_2 to H_2O without the formation of intermediate species like hydrogen peroxide.

Other large cyclic molecules with M–N_4 structures, such as phthalocyanines and metal corroles, have also been demonstrated to be suitable metal coordination ligands.[81] Collman and co-workers synthesized two catalysts, iron porphyrin (Fe(mapc-t)) and cobalt porphyrin (Co(mapc-t)). And the ORR performance of two catalysts were tested by RRDE. Both catalysts exhibited an onset potential ranging from 500 to 700 mV and showed a half-wave potential shift of 200 to 400 mV. However, Co(mapc-t) demonstrated a more pronounced $2e^-$ ORR selectivity, while Fe(mapc-t) exhibited a higher disk current and a smaller ring current, which indicated direct oxygen reduction to H_2O. Furthermore, compared to the Tafel slope of 86 mV dec^{-1} for cobalt porphyrin, iron porphyrin displayed a lower Tafel slope of 120 mV dec^{-1}.

In addition, the development of hybrid electrodes combining COFs and conductive materials has been explored for catalyzing the ORR (Figure 2.9c).[50] A porphyrin-based COP coordinated with cobalt was synthesized and incorporated with highly conductive graphene to form a composite electrode. The resulting COP-P-SO_3-Co-rGO composite electrode exhibited significantly improved electrical conductivity of 3.06×10^{-9} S m^{-1}, which was seven times higher than that of the original COP. Simultaneously, this COP-P-SO_3-Co-rGO hybrid catalyst demonstrated excellent ORR activity (Figure 2.9d). It displayed an onset potential of 0.88 V and a half-wave potential of 0.15 V. In addition, it exhibited a high total electron transfer number of 3.7 and a low Tafel slope of 0.066 V dec^{-1}. Furthermore, this hybrid catalyst showed remarkable stability and durability, maintaining its activity after more than 3000 cycles in a strongly alkaline environment.

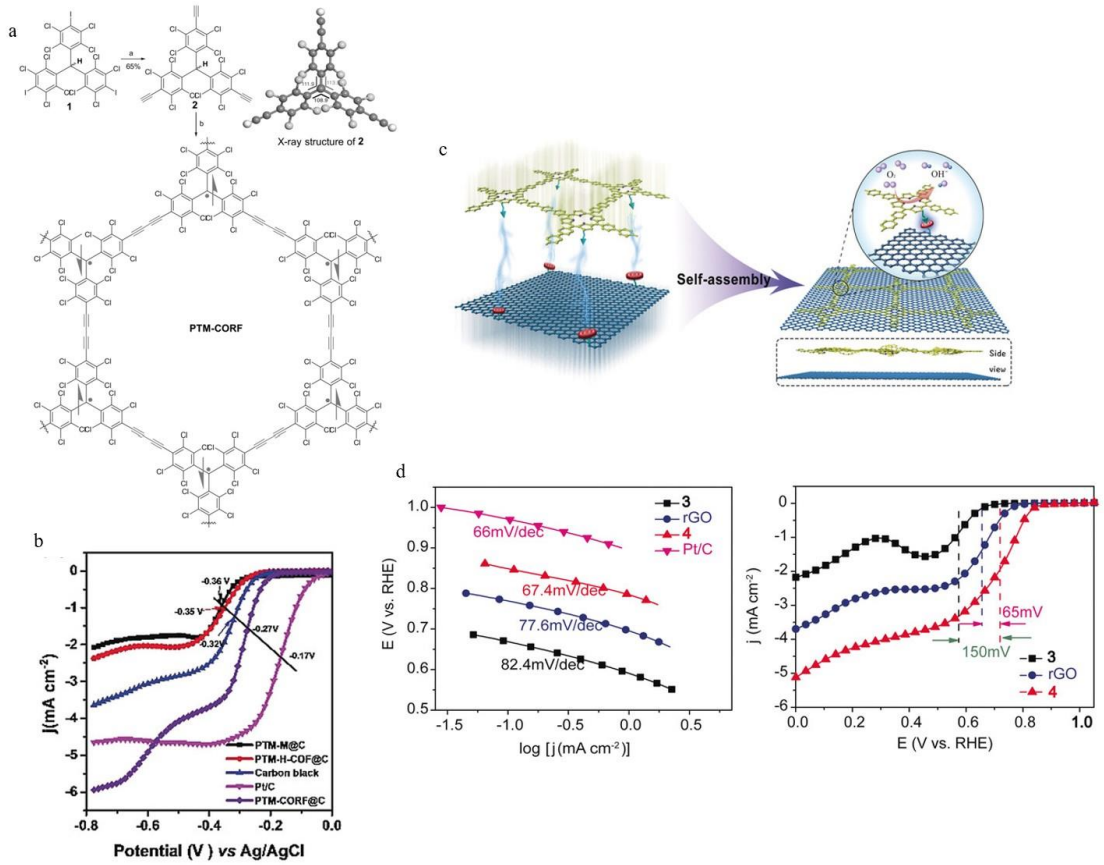

Figure 2.9. (a), Synthesis strategy of PTM-H-CORF containing polychlorinated triphenylmethyl as an ORR catalyst, where reactant 1 is tri(4-iodo-2,3,5,6-tetrachlorophenyl) methane monomer, and reactant 2 is tri(4-ethynyl-2,3,5,6-tetrachlorophenyl) methane monomer. (b), LSV curves of PTM-CORF in an oxygen-saturated 0.1 m KOH solution at a scan rate of 10 mVs $^{-1}$.[77] (c), Schematic diagram of the synthesis of a composite electrode of cobalt porphyrin COP and conductive graphene. (d), ORR performance test for COP-P-SO_3-Co-rGO.[50]

2.3.2 Energy storage

The unique advantages of COFs make them highly suitable as electrode materials for electrochemical energy storage devices.[82] Firstly, the ordered skeleton of COFs provides channels for rapid transfer of electrolyte ions. Secondly, their large specific

surface area can expose more redox active sites, thereby shortening the diffusion pathway for ions. Thirdly, their designable topological structures can accommodate various functional groups, enabling the development of energy storage devices with specific requirements. Fourthly, COFs exhibit excellent stability due to the presence of their strong covalent bonds and rigid structures.

2.3.2.1 Supercapacitors

Supercapacitors store electrical energy through two mechanisms, the double layer capacitance and the pseudocapacitance.[83] The double-layer capacitance is generated by the movement of charges across the surface of the electrodes, while the pseudocapacitance occurs through Faradaic electron transfer at the redox-active groups on the electrode. COFs, being a material with a large specific surface area, can provide a larger plane for the aggregation of charge, which enables a higher double-layer capacitance.[84] At the same time, the rich pore structure inside COFs can accommodate a larger number of redox-active groups, resulting in a significant pseudocapacitance contribution.[85] In addition to specific surface area and specific capacitance, other metrics such as energy density, power density, and thermal and chemical stability can also be used to characterize supercapacitors.

A π-conjugated COF synthesized from 1,3,5-tris(4-aminophenyl) triazine and 2,4,6-trihydroxyisophthalaldehyde was proposed as an effective material for enhancing double-layer capacitance.[86] This COF exhibited a high specific surface area of 545 $m^2 g^{-1}$ and provided enough space for charge accumulation. It also demonstrated excellent

electrochemical performance, with a high specific capacitance of 348 F g^{-1} at a current density of 0.5 A g^{-1}. In addition, after 1000 charge-discharge cycles at 5 A g^{-1} current density, it still retained 95% of its initial specific capacitance. This indicated the remarkable stability of the COF. The enhanced performance in electrochemical double-layer capacitors (EDLCs) could be attributed to its internal π-conjugated system, which facilitated a large specific surface area and promoted charge accumulation.

A *β*-ketoenamine COF named DAAQ-TFP COF was first explored as an electrode material for pseudocapacitors.[60] By employing a solvent-thermal condensation method, anthraquinone, one of the redox-active quinone moieties, is incorporated into the COF structure. The resulting DAAQ-TFP COF exhibited an outstanding specific surface area, reaching up to 1280 m^2 g^{-1}. However, the DAAQ-TFP COF did not show satisfactory specific capacitance, with only 48 F g^{-1} at a current density of 0.1 A g^{-1}. In the meantime, it only retained 80% of its capacitance after 5000 cycles. This could be attributed to the poor contact between the anthraquinone moieties and the active sites, resulting in a low utilization efficiency of only 2.5%. Therefore, further optimization strategies are necessary to improve the specific capacitance and utilization efficiency of COFs to enhance the pseudocapacitive performance.

The specific surface area and specific capacitance of the electrodes can be further improved by changing the morphology of the COFs. A tubular triazine COF (TPT-DAHQ COF) has been synthesized through a solvothermal reaction of 2,5-diaminohydroquinone and planar tris(4-formylphenyl) triazine.[87] The surface of this COF exhibited a spongy morphology with a hollow interior. This unique structure was

achieved by the initial formation of a ribbon-shaped COF, which had been through self-folding into tubular structures driven by intermolecular interactions. This resulted in a significantly increased specific surface area of 1855 $m^2 g^{-1}$. Meanwhile, the TPT-DAHQ COF possessed a high pore volume and a large number of mesopores with a diameter of 2.3 nm. The presence of the hollow structure and mesopores facilitated rapid particle transport within the electrode. As a result, the electrode demonstrated a high specific capacitance of 256 F g^{-1} at a current density of 0.5 A g^{-1}. Moreover, it had excellent cycling life as it retained 98% of its capacitance after more than 1000 cycles. In addition, the TPT-DAHQ COF exhibited an outstanding energy density of 43 W h kg^{-1}, highlighting its potential for energy storage applications.

Another research has demonstrated that thin film *β*-ketoimine COFs exhibited a significantly higher specific capacitance compared to their powder counterparts and achieved an increase of nearly eight times.[88] In contrast to solvothermal condensed powder COFs, these films with 200 nm thickness were prepared by the slow addition of reactants under a coating of Au. The thin film electrodes possessed a remarkable specific surface area of more than 1000 $m^2 g^{-1}$ due to their larger contact surface. They also featured abundant pore structures, including micropores and mesopores. The increased specific surface area significantly enhanced the utilization of the *β*-ketoimine moieties and increased the utilization efficiency from 2.5% in the powder form to over 80%. As a result, the areal capacitance of the thin film COF electrodes reached 3.0 mF cm^{-2}, much higher than the 0.40 mF cm^{-2} of the powder COF. In addition, the thin film electrodes had superior stability, retaining 93% of the initial capacitance after 5000 charge-

discharge cycles.

To further improve the charge transfer in electrodes, the synthesis of composites combining COFs and highly conductive materials has been explored. Sun and colleagues developed a composite electrode (COF/NH_2-rGO) that retained the nanoporous structure of COFs while incorporating highly conductive graphene as well as exhibited a unique π-conjugated system.[89] The composite material was first prepared by synthesizing a precursor COF through condensation of 1,3,5-triformylbenzene and 1,4-diaminobenzene, which was followed by doping with graphene modified with amines. By testing the electrochemical properties of the composite, its cyclic voltammetry curve revealed an irregular rectangular shape, indicating the contribution of both double-layer capacitance and pseudocapacitance. At the same time, COF/NH_2-rGO exhibited a high specific capacitance of 533 F g^{-1} at a current density of 0.2 A g^{-1} in alkaline electrolytes, surpassing the precursor COF (226 F g^{-1}) and nitrogen-doped graphene (190 F g^{-1}). The excellent performance could be attributed to the effective surface integration and growth of graphene on the COF surface, enabling efficient charge transfer. And the redox active moiety anthraquinone also facilitated redox reactions. This synergistic effect greatly enhanced the specific capacitance of the composite material. Additionally, COF/NH_2-rGO demonstrated 79% capacitance retention after 1000 charge-discharge cycles. These outstanding properties demonstrated that the combination of COF and conductive materials in composite electrodes offered improved rate performance and excellent electrochemical performance compared to original powder COFs.

2.3.2.2 Rechargeable batteries

Rechargeable batteries, particularly metal ion batteries, require electrode materials with excellent electrochemical performance and high durability. COFs offer promising prospects due to their unique structures. The distinctive skeleton of COFs can accommodate a regular distribution of redox-active sites, while the abundant porous structure facilitates charge movement. For lithium-ion batteries, COF electrodes connected by covalent bonds can prevent lithium-ion diffusion during lithiation, thereby enhancing the overall durability of the battery. In the case of lithium-sulfur (Li–S) batteries, COFs can inhibit the dissolution of lithium polysulfides and prevent lithium-ion migration between electrodes, thereby improving battery stability. For sodium-ion batteries, COFs can effectively mitigate the volume expansion caused by large-diameter sodium ions. Moreover, their rich porous structure facilitates the rapid kinetics of sodium-ion movement and then provides fast dynamics for the battery. Similar to supercapacitors, properties such as specific surface area, porosity, battery capacity and cycling stability serve as key performance indicators for evaluating batteries.

A COF with redox-active sites, named DTP-ANDI-COF, was first developed as a cathode material for lithium-ion batteries (Figure 2.10a).[90] This COF exhibited a large specific surface area of 1583 $m^2 g^{-1}$ and a pore volume of 0.78 $cm^3 g^{-1}$. The abundant porous structure of the COF not only consisted of micropores but also included mesopores with a diameter of 5.06 nm. The presence of mesopores facilitated fast charge transport and enhanced the interaction between electrolyte ions and active sites (Figure 2.10b). Simultaneously, electrochemical testing revealed that the DTP-ANDI-COF had

a discharge capacity of 42 mA h g^{-1} at a current density of 200 mA g^{-1}. The excellent performance could be attributed to the high pore volume and an impressive utilization rate of up to 82% for the active sites. Furthermore, carbon nanotubes (CNTs) were used as conductive additives to enhance the conductivity of the composite electrode by doping with the DTP-ANDI-COF. The electrode modified by CNT exhibited an improved conductivity and a higher capacity of 67 mAh g^{-1} at the same current density. Additionally, the composite material demonstrated good stability, maintaining its structural integrity and 100% coulombic efficiency after 100 cycles of high-speed charge and discharge.

COFs possess a π-electron leaving domain system. This conjugated structure not only facilitates ion transport but also allows for forming π–K^+ bonds with potassium ions, which is advantageous for potassium ion storage.[91] Therefore, COFs hold the potential to be used as anode materials for lithium-ion batteries in addition to cathode materials. The first reported COF used as a negative electrode material for Li-ion batteries, TThPP, was a thiophene COF containing a porphyrin macrocycle.[92] This COF exhibited a high capacity of 666 mAh g^{-1} at a current density of 200 mA g^{-1}. Its excellent performance could be attributed to the abundant pores and framework that provide pathways for Li^+ transport and storage as well as prevent electrode polarization caused by Li^+ diffusion. Simultaneously, lithium ions can not only be accommodated within the pore structure of the COF but also stored in the layered space of the porphyrin macrocycle. Furthermore, TThPP demonstrated high durability, maintaining over 90% coulombic efficiency after 200 charge-discharge cycles and retaining a high capacity even at high current densities.

The Li–S battery is an energy storage device similar in structure to lithium-ion batteries. The sulfur monomer acts as its cathode material and stores lithium ions by forming a compound with lithium ions. However, the leakage of lithium ions leads to a serious compromise in the performance of Li–S batteries.[93] The large specific surface area and reticulated conjugated structure of COFs can provide more active sites for binding with monomeric sulfur, thus facilitating better storage of lithium ions by sulfur monomers.[94] The sulfur-doped COFs with tailored pores have been investigated as cathode materials for Li–S batteries. An electrode (S-CTF-1) with up to 62 wt% sulfur content was synthesized by a sulphuration reaction between sulfur monomers and 1,4-dicyanobenzene.[95] This COF exhibited a high capacity of 482 mAh g^{-1} and maintained a remarkable coulombic efficiency of 99% after 300 cycles, demonstrating excellent stability. The high sulfur content indicated the successful integration of sulfur monomers into the micro-pores of the COF, resulting in a sulfur-containing reticulation structure. This structure effectively hindered the dissolution of lithium polysulfides and the movement of lithium ions between the positive and negative electrodes. Meanwhile, the outstanding durability of S-CTF-1 could be attributed to the formation of stable covalent bonds between sulfur and the COF skeleton, as well as the uniform distribution of sulfur within the pores of COFs.

Sodium-ion batteries (SIBs) have attracted significant attention due to their high abundance, ease of operation, low redox potential, and low activation energy required for monovalent sodium ions. Normally, the anode materials in sodium-ion batteries store sodium ions by conversion reactions. However, the insertion of sodium ions leads to

rapid volume expansion of the electrode, which not only affects the efficiency of sodium ion storage but also results in capacity loss and even electrode degradation. The rich porous structure of COFs can provide flexible pathways for sodium ion insertion, enabling efficient sodium ion storage while effectively mitigating the detrimental effects associated with electrode expansion.[96] The first COF developed as an anode material for SIBs was synthesized by condensing 1,3,5-tris (4-amino phenyl) triazine (TAPT) and 1,3,5-tris (4-formyl phenyl) benzene (TFPB) (Figure 2.10c).[97] This COF exhibited a high reversible capacity of 246 mAh g^{-1} at a current density of 30 mA g^{-1} as well as retained over 50% of its initial capacity after 500 charge-discharge cycles. The excellent performance of the electrode is probably attributed to its large specific surface area of 120 m^2 g^{-1} and mesopores with a diameter of 2.3 nm. The large surface area provided enhanced electrode-electrolyte interactions for ample active sites, while the presence of mesopores facilitated better embedding of sodium ions (Figure 2.10d).

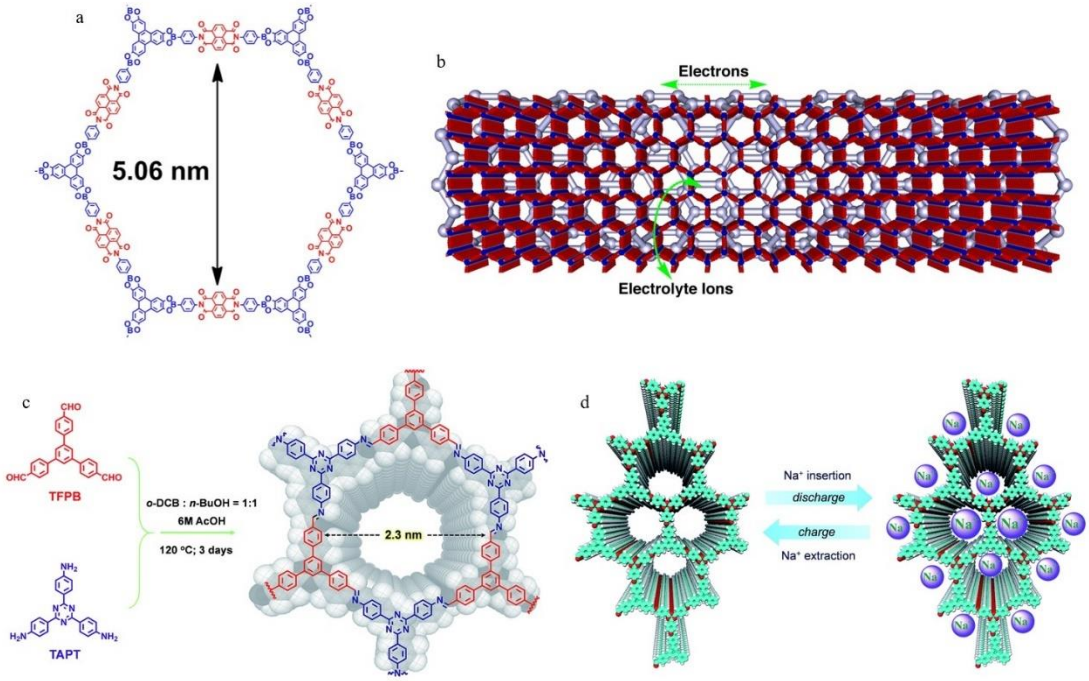

Figure 2.10. (a), Structure of DTP-ANDI-COF as an electrode material for lithium-ion batteries. (b), Schematic representation of mesoporous COF facilitating electron and electrolyte ion transport.[90] (c), Scheme for the synthesis of the anode material for SIBs. (d), A model of sodium ion embedding facilitated by triazine COF.[97]

Chapter III. COFs in supercapacitors

Part of this Chapter is published as:

"Zhuyu Wang, Chaojun Wang, Yuan Chen, Li Wei; *Covalent Organic Frameworks for Capacitive Energy Storage: Recent Progress and Technological Challenges*, Advanced Materials Technologies, **2023**, 8, 2201828"

Supercapacitors are emerging as a new type of high-capacity energy storage device. Compared to batteries, they can rapidly accept and deliver charges while surpassing traditional capacitors by withstanding a higher number of charge and discharge cycles.[98] Supercapacitors rely on two primary mechanisms for energy storage: double-layer capacitance and pseudocapacitance.[99] Over the years, numerous electrode materials have been developed to enhance their performance. Nanocarbon materials, such as activated carbon, carbon nanotubes, and graphene, have been widely used as double-layer capacitor materials. In contrast, metal oxides and conductive polymers have been employed as pseudocapacitive materials.[100] However, the further improvement of supercapacitor performance relies on the continuous development of electrode materials.

COFs, as periodic crystalline porous polymers, possess unique advantages as electrode materials for supercapacitors. Firstly, their high specific surface area provides ample interfaces that facilitate the formation of charge layers and contact with the electrolyte. Secondly, the tunable channels and optimized pore structures of COFs enable effective storage and rapid transport of electrolyte ions. Simultaneously, the presence of micropores and skeletons also provides embedding sites for redox-active functional

groups, thereby enhancing pseudocapacitance.

COFs containing various functional groups have been extensively studied as electrode materials for supercapacitors. Among them, COFs containing aromatized imine bonds have garnered significant attention due to their high chemical stability and excellent conductivity. The outstanding stability is attributed to the fully constrained imine bonds within their delocalization.[101] Moreover, their π-conjugated structures with long π–π bonds provide pathways for efficient and rapid electron movement, while facilitating enhanced contact with redox-active sites.[46, 102] Therefore, their conductivity has been improved. At the same time, the ordered framework structure of these COFs also provides a conductive network for charge storage. Additionally, electrolyte ions can undergo dipolar reactions with the nitrogen atoms in their skeletons, leading to the accumulation of additional protons and thus enhancing their energy storage capacity.[103]

In 2020, Kandambeth *et al.* produced the Hex-Aza-COF-2 containing redox active benzoquinone and the Hex-Aza-COF-3 with phenazine by a solvothermal method using hexaketocyclohexane octahydrate with 1,2,4,5-tetramino-benzoquinone and 2,3,6,7-tetraamino-phenazine hydrochloride.[104] GCD curves indicated a specific capacitance of 585 F g^{-1} for Hex-Aza-COF-2 and 663 F g^{-1} for Hex-Aza-COF-3 at a current density of 1 A g^{-1}. The device fabricated by Hex-Aza-COF-3 performed well in the cycle life testing as the cyclic stability was 89% after 7500 cycles. Meanwhile, it showed an energy density of 23.3 Wh kg^{-1} and a power density of 661.2 W kg^{-1}. The high performance of Hex-Aza-COF was due to the pseudo capacitance contributed by the reversible electron transfer of the phenazine and benzoquinone.

Kou *et al.* reported a series of cooperative porous frameworks (Aza-CMPs) containing aza π-conjugated microporous polymers from 1,2,4,5-Benzenetetramine tetrahydrochloride and triquinoyl hydrate in 2011.[105] Aza-CMP@350 had an excellent specific surface area of 546 $m^2 g^{-1}$ and an ordered pore structure with a large pore size of 1.4 nm. By GCD experiments, the specific capacitance was 397 F g^{-1} at a current density of 5 A g^{-1} and did not drop much to 378 F g^{-1} at 10 A g^{-1}. This result indicated that it is possible for Aza-CMP@350 to achieve fast charging and discharging. Meanwhile, the specific capacitance was maintained at 100% of the initial capacitance at 5 A g^{-1} after 10000 charge/discharge cycles. Aza-CMPs collected electrolyte ions through electrostatic effects, the suitable pore size promoted rapid ion movement and the large specific surface area provided an interface for ion aggregation, thus facilitating the formation of charge layers.

A composite MOF@COF electrode material (aza-MOF@COF) synthesised by aza-Diels-Alder ring addition was reported in 2020.[106] By introducing a quinoline fraction, these materials exhibited high porosity, crystallinity, and exceptional stability. As a result, when assembled as electrode materials in capacitors, they demonstrated outstanding specific capacitance of 20.35 μF cm^{-2}, which was twice as high as the capacitance of the precursors MOF-UIO66-NH_2 and MOF@COF-LZU1, and over ten times higher than commonly used electrode carbon materials such as graphene and activated carbon. Furthermore, the electrode maintained 89.3% of its maximum capacitance after 2000 cycles, indicating excellent electrochemical performance and cycling stability of aza-MOF@COF. This might be due to the expansion of the π ionization domain in the

electrode material after addition through the aza ring. At the same time, this π ionization could reduce the pore size to 0.7 nm, which was closer to 0.68 nm for $(C_2H_5)_4^+$ and 0.33 nm for NBF_4^-, thus facilitating the rapid movement of the electrolyte ions.

Although imine-linked COFs have been extensively studied for their excellent electrochemical performance, their thermal stability remains an issue. Studies have shown that incorporating charge carriers into COFs can effectively improve their stability.[107] And ammonium ions, as a charge carrier, can form unique hydrogen bonds with units containing pyridinic nitrogen, thereby enhancing the stability of the coordinating ligands.

Here, I aimed to synthesize an aza-COF containing NH_4^+ as a charge carrier and investigate its potential as an electrode material for supercapacitors with high electrochemical performance and excellent stability. My hypothesis was that this aza-COF would exhibit two pairs of redox peaks in cyclic voltammetry testing, including a reversible protonation reaction occurring on the nitrogen sp^2-orbitals and a reversible protonation reaction resulting from the introduction of pyridinic redox active moieties. However, I did not achieve the expected results. Therefore, we investigated the progress and applications of COFs as supercapacitor electrode materials after 2018 and summarized the challenges and prospects of COFs, compiled into a literature review and published.

3.1 Introduction

Renewable electricity harvested from primary energy sources, such as solar, wind, and

tide, is essential to addressing environmental challenges and enabling a sustainable future.[108] Developing high-performance electrochemical energy storage devices has attracted significant attention in the past few decades due to growing demands from our fast transformation into an electrified society.[109] Among various energy storage devices, supercapacitors (SCs) offer some unique energy storage properties, such as high power density, rapid charge/discharge rate, long cycling life, and working in a wide range of temperatures.[110]

In principle, supercapacitors may store electrical energy through the electrical double-layer capacitance (EDLC), pseudocapacitance, or a mix of the above two.[110f] EDLC stems from the electrostatically reversible electrolyte ion adsorption and desorption on electrode surfaces.[111] Therefore, electrodes with a large specific surface area and good electrical conductivity are essential to obtain a high EDLC. Carbon materials, such as activated carbon,[112] graphene,[113] carbon nanotubes (CNTs),[114] have common EDLC materials due to their large specific surface area, high electrical conductivity, good cycling stability, and reasonably low cost. On the other hand, pseudocapacitance originates from rapid and reversible faradaic reactions occurring on the surfaces of redox-active electrodes.[115] Common pseudocapacitive materials include transition metal oxides and conducting polymers.[116] Further, asymmetric hybrid capacitors combine electrodes with EDLC and pseudocapacitance to obtain broader operating potential windows and substantially higher energy density.[117]

The properties of capacitive electrode materials govern the energy storage performance of supercapacitors. Extensive research efforts have been devoted to

developing novel capacitive materials. These efforts have focused on two main strategies: (1) increasing the ion-accessible surface area of capacitive materials and (2) incorporating redox-active species to increase pseudocapacitance, achieving significant progress. For instance, a 3D graphene framework prepared by thermal decomposition exhibited a large specific surface area of 1018 $m^2 g^{-1}$ and a high specific capacitance of 266 F g^{-1} at a current density of 0.5 A g^{-1}.[118] A nanoporous carbon sphere with an exceptional specific surface area of 3357 $m^2 g^{-1}$ showed a specific capacitance of 405 F g^{-1} at 0.5 A g^{-1}.[119] Many studies have optimized the crystallinity, pore structure, and redox-active species of metal oxides/hydroxides and polymeric materials.[120] However, irregular pore structures, low electrical conductivity, uneven distribution of redox-active species in capacitive materials, and uncontrollable agglomeration of their nanoparticles often increase the mass transfer resistance of electrolyte ions and reduce their accessible surface areas, resulting in deteriorated energy storage performance. Further, metal dissolution and crystal structure transformation of metal oxides/hydroxides and fast degradation of polymeric materials also shorten the cycling life of supercapacitors fabricated using these materials.[121] Therefore, developing novel capacitive materials with regulatable pore structures, large specific surface area and uniformly distributed redox-active species is desirable.

As a new class of crystalline porous organic polymers, covalent organic frameworks (COFs) possess some unique properties, making them a potential material candidate for supercapacitors.[122] COFs are constructed from organic monomers linked by covalent bonds, and their structures are extended into 2D or 3D in an ordered fashion. COFs'

structures can be designed using suitable organic monomers, linking bonds, and appropriate post-synthetic functionalization, which grants them regulatable pore structures, large and accessible surface area, and abundant redox-active species anchored into their backbones or on pore surfaces.[123] Since the first report on applying *β*-ketoenamine-linked COFs for supercapacitors, this research area has witnessed rapid development. This review intends to provide a timely summary of COF-based or COF-derived materials for supercapacitor applications reported since 2018. We begin with a brief description of COF design and synthesis methods, followed by a detailed discussion on the recent progress of applying COF-based and COF-derived materials for supercapacitors. Finally, we provide our perspective on the challenges and future research directions of realizing practical applications of COF materials in supercapacitors.

3.2 The design and synthesis of COFs

COFs can be categorized into 2D and 3D COFs depending on the extending direction of their periodic-repeating units. COFs can be designed with tunable topology, crystallinity, porosity and other physiochemical properties governed by their constituting monomers.[124] These monomers can be classified by their symmetries (C_n, n=2, 3, 4 and 6, D_{2h}, and T_d).[123a, 123b] The varied combinations of different monomers result in various COF structures that now can be found *via* several online databases.[125]

2D COFs with a planar geometry can be symmetric or asymmetric[126], exhibiting trigonal, rhombic, tetragonal, hexagonal, or varied pore combinations (*e.g.*, dual-pore

Kagome and triple-pore Kagome), as displayed in Figure 3.1a. These topologies can be controlled using different combinations of monomers. For example, the combination of [$3C_6$–$3C_2$] (three C_6 monomers and three C_2 monomers) tends to form 2D COFs with trigonal topology.[127] The [$4C_4$–$4C_2$] and [$2C_4$–$2C_4$] combinations lead to tetragonal porous 2D COFs.[128] Regular hexagonal pores are obtained by the combinations of [$3C_2$], [$3C_3$], and [$3C_3$+$2C_2$].[129] Irregular hexagonal pores can be created by [$4C_2$+$4C_2$] and [$6C_2$+$6C_2$] combinations.[130] 2D COFs' structures can be further extended using a multiple-component strategy with two or three types of monomers.[131] On the other hand, 3D COFs are synthesized using one or more stereo-configurable building blocks. The requirement of multiple linking sites and highly symmetric stereo structures has resulted in fewer stereo-constituted monomer candidates and hence, much fewer reported 3D COFs than 2D COFs. The design and prediction of 3D COFs' topology also remain challenging because of their interpenetrated structures. Figure 3.1b illustrates several 3D COF topologies that have been demonstrated using monomers with different symmetries.[5, 125b, 132]

Covalent bonds hold different monomers in COFs together. Unlike amorphous polymers, the formation of covalent bonds in COF synthesis is usually reversible, allowing self-correction and rearrangement towards crystallized COF structures. Common covalent bonds include boroxine, boronic ester, borazine, triazine, imine, hydrazone, phenazine, azine, imide, β-ketoenamine, cyanovinylene, and 1,4-dioxin, as summarized in Figure 3.1c. However, the fast hydrolysis of boroxine and boronic ester bonds excludes COFs linked by them from potential supercapacitor applications. Imine

bonds are acceptable because of their excellent chemical stability.[133] The irreversible enol-keto tautomerization of *β*-ketoenamine bonds has enabled COFs with superior stability in strong acid and alkaline solutions (*e.g.*, 9 N HCl and 9 N NaOH).[134] specific surface areaacceptable chemical stability for supercapacitor applications.

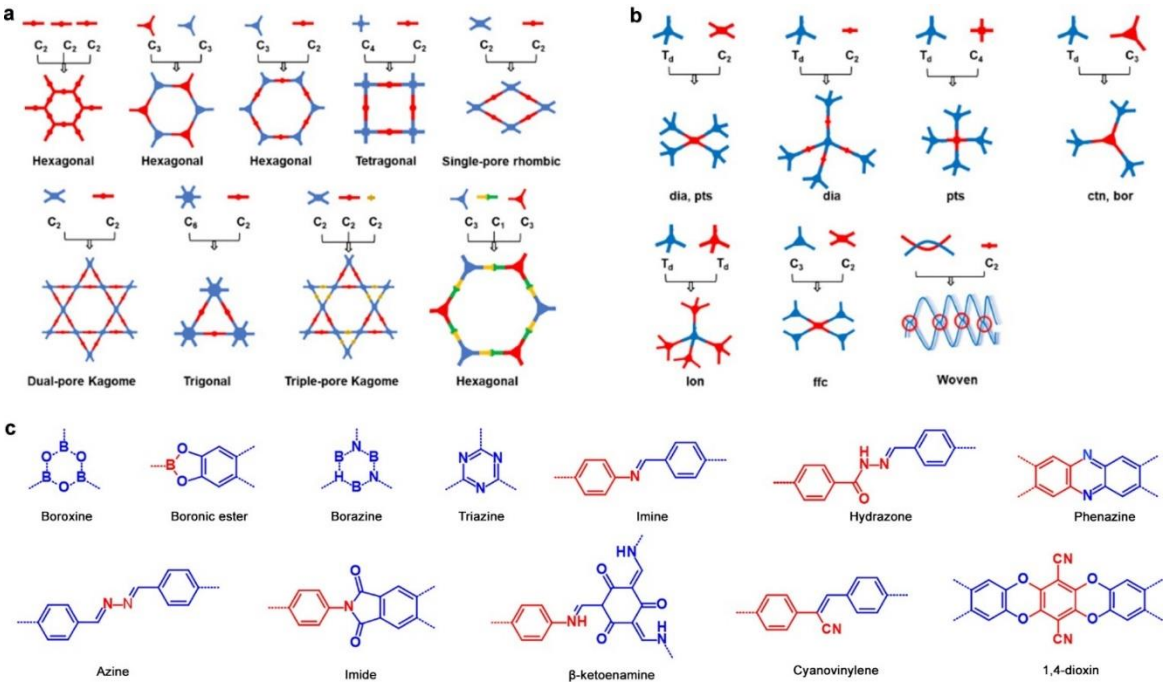

Figure 3.1. Topology diagrams of (a), 2D COFs and (b), 3D COFs formed by different building blocks.[123b] (c), Common linking covalent bonds in COFs. Red and blue colors indicate atoms contributed by different monomers.

Several COF synthesis methods, including solvothermal, ionothermal, microwave heating, sono- and mechano-chemical, have been used to drive covalent bond formations between monomers.[123b, 123e, 123g] Each method has advantages and disadvantages. Solvothermal methods are the most common method, where dissolved monomers react in suitable solvents. High-quality COF crystalline products can be obtained at a proper

temperature (80~180 °C) over an extended reaction time (3~7 days).[4] However, the monomer's solubility may limit this method's applicability to form some COFs. Ionothermal methods use ionic liquids or molten salts as the solvent. They can be carried out at much higher reaction temperatures (*e.g.*, 400 °C), which significantly accelerate COF formation. However, high-temperature reactions may cause undesired product decomposition.[135] Microwave heating methods offer better control over reaction temperatures and pressures, resulting in rapid COF formation, but they require high-cost microwave reactors.[136] Sono- and mechano-chemical methods utilize sonication and grinding to drive covalent bond formation at room temperatures.[137] They offer a facile, fast, and scalable route for COF synthesis. However, the lack of a solvent environment makes them only applicable to COFs with small monomers, often resulting in poor crystallinity. To date, solvothermal and mechanochemical methods are the primary methods to synthesize COFs used for supercapacitor applications.

3.3 COFs for supercapacitor applications

COFs with large specific surface areas and regular pore structures meet the essential requirements to enable large EDLC for supercapacitors. By further incorporating redox-active species, reversible Faradaic reactions at these redox sites can offer pseudocapacitance to boost energy storage density further. Hybridizing COFs with electrically conductive materials lead to COF-based hybrids with increased electrical conductivity. Furthermore, abundant heteroatoms in COFs, such as N and S, make them promising precursors to derive heteroatom-doped carbon materials for supercapacitor

applications. Following these different areas, we summarize this section's recently reported COF-based or COF-derived capacitive materials. The structural properties and performance of these materials are compared in Table 1. We will discuss these three areas in the following three sub-sections.

3.3.1 Pristine COFs for EDLC supercapacitors

Numerous studies have shown that electrode materials with well-developed porous structures and a large specific surface area can deliver good energy storage performance in EDLC supercapacitors.[138] Since the first report in 2013,[139] the unique structural advantages of COFs have made them appealing candidates as electrode materials for EDLC supercapacitors.

First, a 2D π-conjugated TFP-NDA-COF nanowire was prepared by Schiff-base condensation of 1,3,5-triformylphloroglucinol (TFP) and 1,5-diaminonaphthalene (NDA), as shown in Figure 3.2a.[140] This COF showed a specific surface area of 353 m ^{2} g $^{-1}$ with micropores centered around 1.67 nm. This COF exhibited a gravimetric specific capacitance (C_s) of 379 F g^{-1} at a scan rate of 2 mV s^{-1}. The authors claimed that the π-electronic conjugation of this COF enhanced ion diffusion in its framework and micropores. This COF retained 75% of its maximum capacitance after 8000 charge/discharge cycles. In another report, a TPDA-1 COF (Figure 3.2b) was synthesized by solvothermal condensation using 2,4,6-trihydroxyisophthalaldehyde and 1,3,5-tris(4-aminophenyl) triazine.[141] The resulting COF showed an of 5 specific surface area 45 m^2 g^{-1} but a poor crystallinity as determined by X-ray diffraction (XRD).

It delivered a C_s of 469.4 F g^{-1} at a scan rate of 2 mV s^{-1} and retained 95% of its capacitance after 1000 charge/discharge cycles. These two studies directly deposited the as-prepared COFs on current collectors for electrochemical tests. The low electrical conductivity of these two COFs can be found in their rhombic cyclic voltammetry (CV) curves obtained at increased scan rates (Figure 3.2c). Further, in combination with a high electrolytic ions diffusion resistance in bulk COF blocks, these two COFs exhibited unsatisfactory rate performance (*i.e.*, ~20% capacitance retention, as shown in Figure 3.2d).

An effective way to improve the rate performance of pristine COFs is to exfoliate stacked bulk COFs into nanosheets with reduced thickness, which are beneficial for electrolyte ion diffusion. Their low electrical conductivity can be increased by incorporating various conductive additives, such as carbon black, during the electrode fabrication. For example, by condensing hydroxyl-containing 4,4′-(1,2-ethynediyl)bis-2-hydroxybenzaldehyde and 5,10,15,20-tetrakis[(4-aminophenyl)porphyrin, Fang *et al.* reported a series of 2D COFs with 3.4 nm square-like open channels (JUC-510/511/512, Figure 3.2e).[142] The bulk COFs were exfoliated into nanosheets of 19~36 nm thickness in isopropanol by sonication (Figure 3.2f). The exfoliated JUC-512 COF was mixed with 30 wt% carbon black and fabricated into two-electrode supercapacitors, delivering a high areal specific capacitance of 5.85 mF cm^{-2} (Figure 3.2g) at a fast scan rate of 1000 mV s^{-1} using an organic electrolyte. The improved ion diffusion was further demonstrated with a short relaxation time constant (τ_0) of 178 ms, as determined by electrochemical impedance spectroscopy (EIS). These performance improvements were attributed to the

large pore size and reduced diffusion length in the thin COF nanosheets.

More recently, Zamora *et al.* demonstrated an approach to synthesize COF-based aerogels as supercapacitor electrodes, delivering good energy storage performance in acid, alkaline and organic electrolytes (Figure 3.2h).[143] By using solvent exchange and subsequent supercritical CO_2 activation, COF aerogels exhibited abundant mesopores ranging from 2–50 nm while retaining good crystallinity. A conductive carbon black was mixed with the aerogel, resulting in seven orders higher electrical conductivity than that of pristine COF aerogels. Consequently, the hybrid electrodes demonstrated a large areal specific capacitance of 11.2 mF cm^{-2} at a mass loading of 9.95 mg cm^{-2} in a 6 M KOH electrolyte. Notably, the authors carried out detailed EIS characterization, which can serve as a standard characterization protocol for future studies.

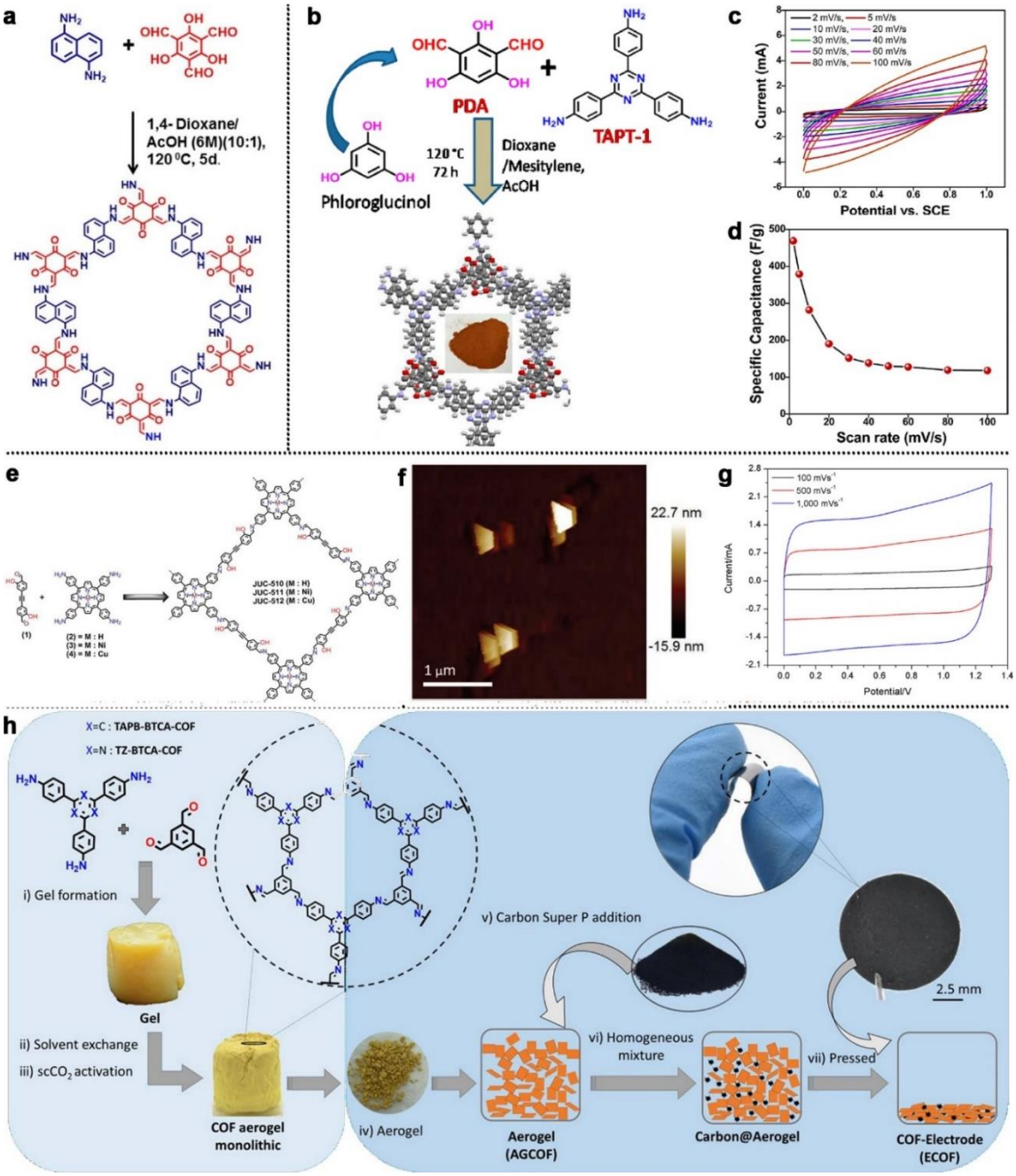

Figure 3.2. (a), The synthesis scheme of TFP-NDA-COF.[140] (b), Synthesis and atomic structure. (c), CV curves, and (d), rate performance of the TPDA-1 COF.[141] (e), Synthesis and structure (f), an AFM image, and (g), CV curves of the exfoliated JUC-512 COF.[142] (h), Synthesis of ECOF electrode via the aerogel approach.[143]

3.3.2 COF-based pseudocapacitors

The energy storage mechanism of the above COF-based EDLC supercapacitors is based on electrolyte ions' physical absorption and desorption on COF surfaces. Their specific capacitance is not high. Therefore, other researchers have introduced different redox-active species into COFs to create larger pseudocapacitance. Most redox sites used in pseudocapacitive COFs reported so far are based on redox reactions of non-metal N or O-containing groups or transition metals (*e.g.*, Co and Ni). Their details are discussed below.

Electron-rich N and O moieties are the most commonly used redox-active species. In 2017, an imine-linked COF, TDFP-1, was synthesized by Schiff base condensation between 1,3,5-tris-(4-aminophenyl)triazine (TAPT) and 2,6-diformyl-4-methylphenol (DFP) using a solvothermal method (Figure 3.3a).[144] Cyclic voltammetry scan revealed a pair of reversible redox peaks at ~0.1 V (*vs.* SCE, Figure 3.3b) in a 0.1 M H_2SO_4 electrolyte, which was assigned to the protonation of the imine bond (Figure 3.3c) due to the electron donation from the hydroxyl group on the DFP monomer. The TDFP-1 COF showed a C_s of 418 F g^{-1} at 0.5 A g^{-1}. However, this redox reaction in TDFP-1 was limited by ion diffusion, resulting in poor capacitance retention (<50%) when the current density was increased from 0.5 to 10 A g^{-1}. The poor stability of the imine redox sites also resulted in a 5% capacitance loss after only 1000 charge/discharge cycles.

Aromatized imine bonds exhibited improved electrochemical reversibility. A Hex-Aza-COF-3 COF with redox-active phenazine moiety containing aromatized imine bonds was synthesized by solvothermal condensation between hexaketocyclohexane octahydrate and 2,3,6,7-tetraamino-phenazine hydrochloride (Figure 3.3d).[145] The

phenazine group has a 2^- electron redox reaction (Figure 3.3e), delivering a C_s of 663 F g^{-1} at 1 A g^{-1}. The Hex-Aza-COF-3 COF was further coupled with RuO_2 to fabricate asymmetric hybrid capacitors with an extended operating voltage window up to 1.8 V while exhibiting improved stability by retaining ~90% capacitance after 7500 charge/discharge cycles (Figure 3.3f). In another study, a benzobisoxazole-linked TPT-DAHQ COF was syntheized by condensing 2,4,6-tris(4-formylphenyl)triazine and 2,5-diaminohydroquinone dihydrochloride, which exhibited ~99% capacitance retention after 1850 charge/discharge cycles.[146]

Pyridinic, triazine, quinone and diimide groups have also been used as redox-active species to introduce pseudocapacitance into COFs.[147] Some other redox groups have also been explored. For example, porphyrins can provide pseudocapacitance due to their redox-active pyrrole groups. Patra and co-workers synthesized a redox-active porphyrin-modified COF (PT-COF) by condensing 5,10,15,20-tetrakis(para-amino phenyl) porphyrin (TAPP) and 1,1,2,2-tetrakis(4-formyl-(1,1'-biphenyl))-ethane (TFBE).[148] In an acidic electrolyte, the 18-π electron system of the porphyrin can proceed by a $2H^+$-$2e^-$ coupled step to transform into a 20-π electron system (Figure 3.3g). The improved conjugation may also improve intramolecular electron transportation. Together with a large specific surface area of 1998 m^2 g^{-1}, the authors reported that this COF had a high C_s of 1443 F g^{-1} at 1 A g^{-1} and good cycling stability, *i.e.*, 91% capacitance retention after 3000 charge/discharge cycles.

Meanwhile, redox-active metal cations, such as Ni and Co, can also be incorporated into COFs to induce pseudocapacitance. For example, redox-active Ni^{2+} was

incorporated into a conjugated Ni-COF by a solvothermal method using 1,2,4,5-benzenetetraamine (BTA) and 2,5-dihydroxy-1,4-benzenedicarboxaldehyde (HBC) in the presence of $Ni(OAc)_2 \cdot 4H_2O$ (Figure 3.3h).[149] O and N firmly coordinated Ni^{2+} to form Ni(II)-salphen units, resulting in improved crystallinity and superior conductivity of 1.3×10^{-2} S cm^{-1}, about 1500 times of the COF synthesized without Ni^{2+} (8.4×10^{-6} S cm^{-1}). The authors further proposed that Ni^{2+} favored the hydroquinone/benzoquinone redox reaction (Figure 3.3i) and promoted the electron transport in COF planes, leading to a high C_s of 1257 F g^{-1} at 1 A g^{-1} and excellent stability of 94% capacitance retention after 10000 charge/discharge cycles. Qiao and co-workers grafted Co^{2+} into channels of a TAPB-DHPA COF ($COF_{TAPB\text{-}DHPA}$) by the condensation between 1,3,5-tris(4-aminophenyl)benzene (TAPB) and 2,5-dihydroxyterephthalaldehyde (DHPA).[150] The -OH functional groups and imine bonds on the $COF_{TAPB\text{-}DHPA}$ skeleton provided strong bindings with Co^{2+}. The resulting Co-$COF_{TAPB\text{-}DHPA}$ was fabricated into thin-film micro-supercapacitors, delivering an areal specific capacitance of 1.8 mF cm^{-2}, or a volumetric specific capacitance of 1790.1 F cm^{-3} at a scan rate of 10 mV s^{-1}, which are about 2.2 times higher to that of the corresponding pristine COF.

Besides incorporating redox-active species into COFs, several new strategies, such as creating intramolecular or interlayer interactions, enhancing proton conduction, forming intramolecular charge transfer, and controlling COF morphology, have also been implemented to construct novel COFs with enhanced pseudocapacitance.

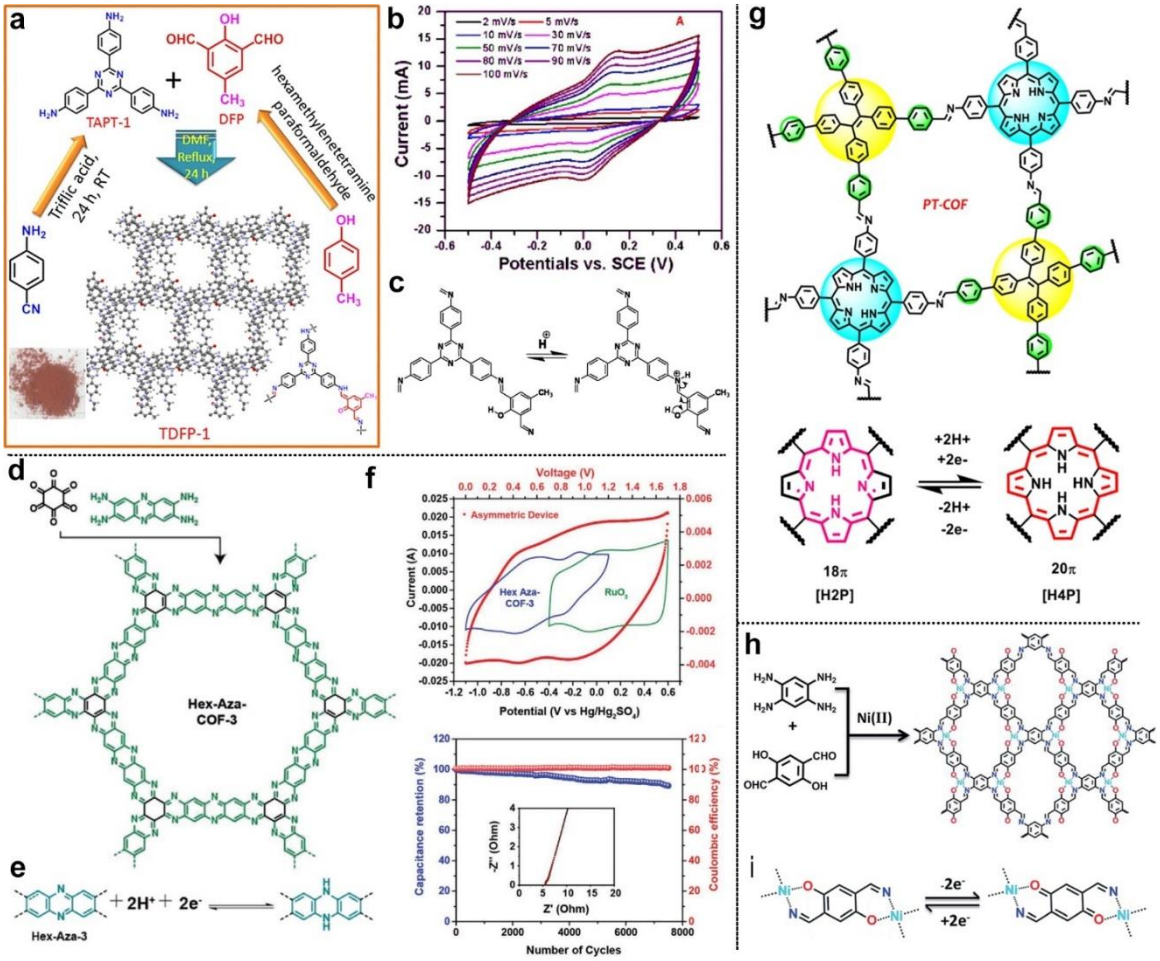

Figure 3.3. (a), The synthetic scheme, (b), CV curves and (c), proposed redox mechanism of TDFP-1 COF.[144] (d), The formation and (e), the $2H^{+}$-$2e^{-}$ coupled redox reaction of a phenazine containing Hex-Aza-COF-3. (f), CV curves and stability performance of asymmetric supercapacitors fabricated using Hex-Aza-COF-3 and RuO_2.[145] (g), Structure and redox reaction of the porphyrin-containing PT-COF.[148] (h), The synthesis scheme of the Ni-COF, and (i), its proposed Ni^{2+}-promoted redox reaction of hydroquinone/benzoquinone.[149]

Intramolecular charge transfer has recently been reported as an effective method to boost the capacitive performance of a TTF-COF-1 COF, which was synthesized from an

electron donor tetraformyl-tetrathiafulvalene (TTF) and electron acceptor 2,6-diaminoanthraquinone (DAQ, Figure 3.4a).[151] The donor-acceptor arrangement in the TTF-COF-1 enhanced the delocalization of π-electrons and improved its electrical conductivity (Figure 3.4b). It delivered a high C_s of 752 F g^{-1} at 1 A g^{-1}, much higher than a TTF-COF-2 COF obtained by replacing the electron acceptor DAQ monomer with non-redox active anthracene-2,6-diamine (DAA). However, it is still arguable whether the reduced capacitance is due to the loss of redox-active sites or the donor-acceptor arrangement.

In 2017, the intramolecular H bond in a TpPa-OH_2 COF synthesized from 1,3,5-triformylpholoroglucinol and 2,5-dihydroxy-1,4-phenyldiamine was found to improve the COF's stability.[120b] H bonds formed between the benzoquinone carbonyl O and the neighbouring amine inhibited the decomposition of the redox active sites, showing an 88% capacity retention after 10000 charge/discharge cycles in a two-electrode supercapacitor. Following this concept, the H bond formed between COF layers was also investigated. For example, the condensation of 2,4,6-trimethoxy-1,3,5-benzenetricarbaldehyde (TpOMe) and 2,6-diaminoanthraquinone (DAQ) by a mechanochemical method yielded freestanding TpOMe-DAQ COF thin films (Figure 3.4c).[152] H atoms in the methoxy moieties formed interlayer C–H···N H bonds with N in imine linking bonds (Figure 3.4d), improving the chemical and mechanical stability of the resulting COF film. This well-crystallized COF exhibited a large specific surface area of 1734 m^2 g^{-1} and a high areal specific capacitance of 1600 mF cm^{-2} (or 169 F g^{-1}) at a current density of 3.3 mA cm^{-2}, as well as excellent cycling stability even after

100,000 charge/discharge cycles. Similar interlayer H bonds were also observed in a PDC-MA-COF obtained by aldol-amine condensation between 1,4-piperazinedicarboxaldehyde (PDC) and melamine (MA).[147b] The neighbouring piperazine rings formed interlayer H bonds, which helped maintain the COF's planar conformation and ordered pores (Figure 3.4e). Besides, the piperazine rings coupled with the triazine moiety promoted a two-electron redox process (Figure 3.4f), resulting in a C_s of 335 F g^{-1} at 1.0 A g^{-1}.

In addition, an attempt was also made to improve the electrochemical performance of N-rich COFs by changing their proton conduction mechanism. Grotthuss proton conduction in inorganic materials was a practical approach to promote redox reactions and improve energy density performance.[153] Following this principle, COFs with improved proton conductivity were demonstrated.[154] Yang *et al.* synthesized an Azo-NHBoc center block by condensing N-Boc-*p*-phenylenediamine and phloroglucinol.[155] This building block offered abundant phenolic hydroxyl groups in COFs, forming aligned proton conducting pathways (Figure 3.4g). At the same time, redox-active azo groups contributed pseudocapacitance and underwent proton-coupled electron transfer to improve electrical conductivity. The NKCOF-2 synthesized using this Azo-NHBoc and 2,5-dihydroxyterephthalaldehyde (DPA) exhibited a high electrical conductivity of 2.42×10^{-3} S cm^{-1} at 298 K. Its Grotthuss proton transfer mechanism was further confirmed by its proton transfer activation energy of 0.15 eV, which was less than 0.4 eV. The hybrid prepared from NKCOF-2 and conductive CNTs demonstrated a C_s of 440 F g^{-1} at 0.5 A g^{-1} current density and reached a 90 % capacitance retention after 10000

charge/discharge cycles.

The atomic structure and morphology of COFs also significantly impact their pseudocapacitive performance. Vaidhyanathan and co-workers investigated the impact of functional groups in COF channels using a series of IISERP-COFs prepared from a (5,5′,5″-(1,3,5-triazine-2,4,6-triyl)tris(pyridine-2-amine) center block and linker monomers with different trialdehydes containing 1, 2, or 3 -hydroxyl groups (*i.e.*, 2-hydroxybenzene-1,3,5-tricarbaldehyde, 2,4-dihydroxybenzene-1,3,5-tricarbaldehyde, and 2,4,6-trihydroxybenzene-1,3,5-tricarbaldehyde).[156] Pore size distribution measurements revealed reduced pore radii with the increased number of the hydroxyl groups, suggesting a COF stacking model transition from eclipse (A–A stacking) towards staggered (A–B stacking). This observation was attributed to the interlayer H bond formed between the hydroxyl groups, which is more favoured in the symmetrically positioned 2- and 3-OH-containing COFs. Consequently, these COFs exhibited varied specific surface area and energy storage performance. The pore properties of COFs were tuned using a multiple-component method (Figure 3.4h).[157] The molar ratio between a redox-active 2,6-diaminoanthraquinone (Dq) and a π-electron-rich 2,6-diaminoanthracene (Da) was adjusted to form a series COFs with a 1,3,5-triformylphloroglucinol (Tp) center block. The resulting COFs exhibited various pore structures, mechanical properties, and electrochemical performance (Figure 3.4i). Dq and Da monomers were found to be critical for energy storage and mechanical strength, respectively. This work suggests that COFs with tunable properties could be designed and synthesized on demand. In addition, the location of active-redox species on

monomers could also impact their energy storage performance (Figure 3.4j).[158] COFs prepared from condensing (1,3,5-tris-(4-aminophenyl)triazine (TAPT) with 2,3-dihydroxynaphthalene dicarbaldehyde (2,3-NADC) or 2,6-dihydroxynaphthalene dicarbaldehyde (2,6-NADC) exhibited identical elemental composition but varied crystalline and pore structures. Interestingly, the TAPT-2,6-NA$(OH)_2$ COF showed a smaller capacitance to that of the TAPT-2,3-NA$(OH)_2$ COF (190 *vs*. 271 F g^{-1} at 0.5 A g^{-1}), while possessed a much larger specific surface area (1089 vs 429 m^2 g^{-1}). This difference was attributed to the increased redox capability of the 2,3-dihydroxynaphthalene over that of the 2,6-dihydroxynaphthalene (Figure 3.4k).

Furthermore, the synthesis reaction time was found to strongly influence the formation of hollow COF spheres synthesized from terephthalaldehyde and 4,4′,4″,4‴-(9,9′-spirobifluorene-2,2′,7,7′-tetrayl) tetraaniline.[159] At a growth time of 96 hours, the optimal 3D-Sp-COF@96 h, which exhibited a hollow interior via the Ostwald ripening mechanism, showed the largest specific surface area of 1016 m^2 g^{-1} and the highest C_s of 251 F g^{-1} at 1 A g^{-1}. However, this study did not discuss the origin of the pronounced redox peaks found in the CV curve of the COFs.

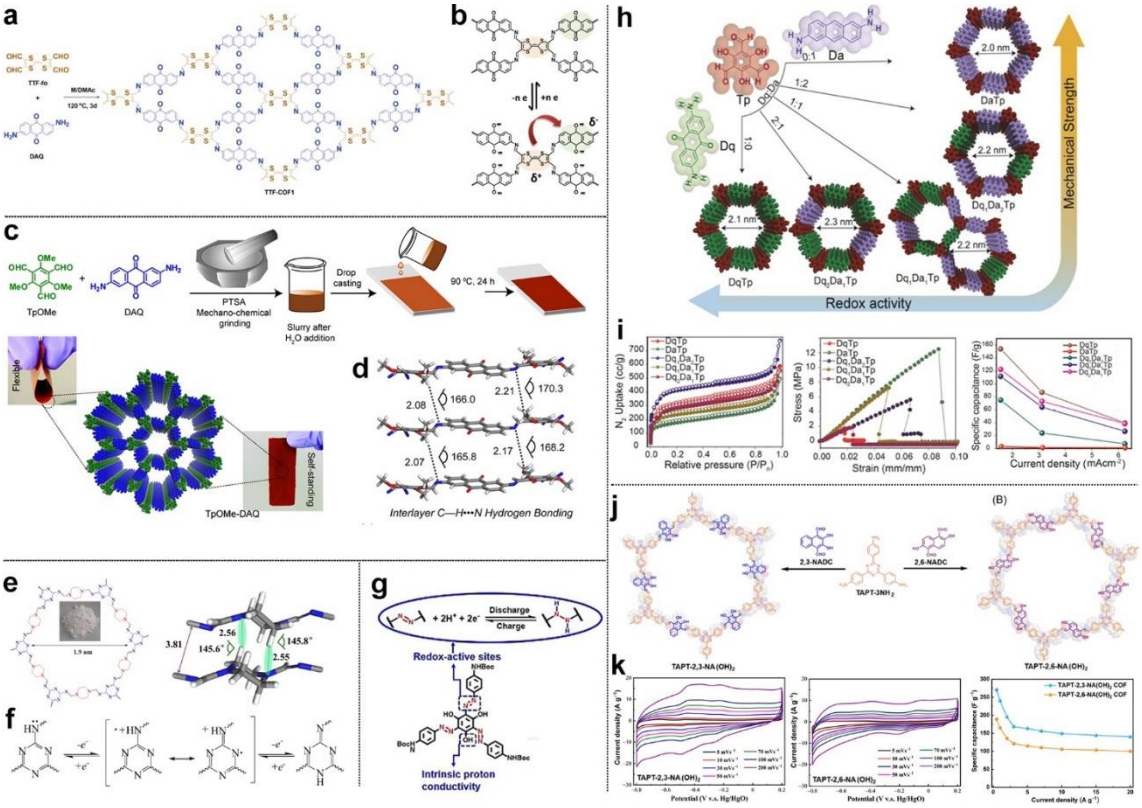

Figure 3.4. (a), Synthesis of TTF-COF-1 COF with electron donor-acceptor arrangement and (b), the corresponding redox mechanism.[151] (c), Mechano synthesis of the TpOMe-DAQ COF thin film and (d), the formation of interlayer hydrogen bonds.[152] (e), Structure and the interlayer H bonds of a PDC-MA-COF. (f), The piperazine group coupled triazine redox process.[147b] (g), The structural features of the Azo-NHBoc center block.[155] (h), Atomic structures and (i), physisorption isotherms, strain-stress test, and capacitive performance of COFs prepared from a Tp center block, and molar ratio varied Dq and Da linkers.[157] (j), The synthesis and (k), electrochemical performance of COFs with their di-hydroxy groups located at different positions.[158]

3.3.3 COF-based hybrid materials

Most COFs are conjugated organic semiconductors with an electrical conductivity

(10^{-8}~10^{-2} S m^{-1}), a few orders lower than carbon materials commonly used for supercapacitors.[160] Such low intrinsic electrical conductivity limits the rate performance of supercapacitors. Further, COFs tend to form bulk aggregates, which reduces their accessible surface area and introduces additional diffusion resistance for electrolyte ions to access COFs' internal surface. Therefore, significant efforts have been devoted to constructing COFs and various conductive substrates as hybrids. Carbon materials, including 1D CNTs, 1D carbon nanofibers (CNFs), 2D reduced graphene oxide (rGO), and 3D carbon scaffolds, are the most commonly used conductive substrates to create these hybrids.

COF hybrid materials with 1D CNTs and CNFs are usually synthesized by *in-situ* formation and deposition of COFs on carbon surfaces. In 2019, Banerjee *et al.* synthesized COF-coated CNF hybrids by adding CNFs in COF precursor pastes (Figure 3.5a).[161] Theoretical calculation and experimental measurements by X-ray photoelectron spectroscopy indicated that strong π–π interactions between COF nanoplates and CNFs led to the strong adsorption of COFs on CNFs, resulting in enhanced electron transfer and a nearly 9-order higher electrical conductivity. With a CNF mass loading of 20 wt% in the hybrids, the optimal redox-active anthraquinone containing DqTp-CNF and DqDaTp-CNF hybrids showed an areal specific capacitance of 464 mF cm^{-2} and 364 mF cm^{-2} at a current density of 0.25 mA cm^{-2}, respectively. Besides, the DqDaTp-CNF hybrid was directly fabricated into flexible thin films as electrodes to assemble supercapacitors, delivering a large areal specific capacitance of 167 mF cm^{-2}, an energy density of 5.8 μW h cm^{-2}, and a power density of 125.0 μW

cm^{-2} at 0.5 mA cm^{-2}. The supercapacitor retained 76% of its capacitance after 4500 charge/discharge cycles at 5 mA cm^{-2}.

Following a similar synthesis strategy, hybrids constituted of a COF shell and a CNT core have been extensively studied.[162] The mass ratio between the COF shell and the CNT core was found to influence electrochemical performances significantly.[162b, 162c] Several studies used redox-active linking bonds to structure COF shells, introducing additional pseudocapacitance or extending the operating potential window. For example, Zhang and co-workers demonstrated a hybrid in which redox-active azo (N=N) bonds linked the NKCOF-2 COF shell.[155] With effectively exposed redox-active sites in the core-shell structure, CNT/NKCOF-2 hybrids demonstrated a C_s of 440 F g^{-1} at 0.5 A g^{-1}. In another study, an imide-linked PAI COF was synthesized from condensation between tris(4-aminophenyl)amine (TAPA) and 1,4,5,8-naphthalene-tetracarboxylic acid dianhydride (NTCDA) in the presence of CNTs.[163] The reversible redox reaction of *n*-type aromatic diimide linking bonds made this PAI@40%CNT hybrid a suitable negative electrode material for asymmetric pseudocapacitors. The hybrid capacitor prepared using this hybrid and RuO_2 positive electrode delivered a C_s of 95 F g^{-1} at 0.5 A g^{-1}.

Conductive 2D materials, such as rGO, have also been used to construct hybrids with COFs. Both *in-situ* and *ex-situ* assembling methods have been explored. Following the similar *in-situ* assembling method used to obtain COF-CNT hybrids, Thomas *et al*. synthesized a COF/rGO aerogel from a GO solution containing COF monomers in a one-step hydrothermal reaction (Figure 3.5b).[164] After freeze drying, a 3D ultralight COF/rGO aerogel was obtained with COF nanosheets intercalated with rGO, exhibiting

a specific surface area of 246 m^2 g^{-1} due to its abundant pores. This aerogel was directly used as electrodes to fabricate supercapacitors. Redox-active anthraquinone groups provided an extended operating voltage window of up to 1.5 V in a 0.5 M H_2SO_4 electrolyte. The COF/rGO hybrid showed a C_s of 269 F g^{-1} at 0.5 A g^{-1}. It retained 83% capacitance at 10 A g^{-1}, which is much higher than the negligible performance of the pristine COF (Figure 3.5c). Similar methods were used to synthesize various hybrids with other COFs.[165] Furthermore, other conductive 2D materials, such as Ti_3C_2 MXene, have been used to replace rGO to form hybrids with COFs.[166] One study found that the surface modification with (3-aminopropyl) triethoxysilane guided the growth of COF nanosheets, delivering a C_s of 290 F g^{-1} at 0.5 A g^{-1} in a neutral 1 M Na_2SO_4 electrolyte.

Alternatively, *ex-situ* assembling methods were used to synthesize hybrids using COF and 2D conductive substrates. As-synthesized COFs were first exfoliated and suspended in organic solvents (*e.g.*, N-methyl-2-pyrrolidone, NMP), and then mixed with GO or rGO suspensions. The assembly can be realized by hydrothermal treatment or vacuum filtration. For example, a 2D COF, ILCOF-1, was exfoliated by sonication and added to a GO solution, followed by hydrothermal treatment to reduce GO and assemble with the COF into hybrids (Figure 3.5d).[167] The co-intercalation between exfoliated 2D COF and rGO nanosheets effectively prevented the restacking of both components and improved the electrical conductivity, surface area and ion diffusion properties. At an optimal COF mass loading of 20 wt%, the rGO/COF-20 hybrid delivered a C_s of 321 F g^{-1} at 1 A g^{-1}, much higher than that of rGO (194 F g^{-1}) and pristine COF (10 F g^{-1}). Following a similar method, redox-active COFs were also used to assemble hybrids,

showing improved electrochemical performance.[168] Vacuum filtration was also used to assemble COF-rGO films and applied as electrodes in supercapacitors directly (Figure 3.5e). Using an arbitrary filtering mask, comb-shaped electrodes were obtained and used to fabricate flexible micro-supercapacitors (Figure 3.5f), delivering a maximum power density of 9998 W kg^{-1}.[169]

3D porous substrates, such as graphene aerogels and other carbon skeletons, were also used to assemble hybrids with *in-situ* synthesized COFs. 3D carbon substrates usually possess abundant and interconnected macropores with large pore sizes, allowing easy infiltration of COF monomers. The resulting hybrids have hierarchical pore structures. For example, a porous graphene-wrapped carbon foam (GCF) was synthesized by coating GO nanosheets on a carbonized melamine foam and exposing them to a subsequent thermal treatment (Figure 3.5g).[170] It was then used to host a redox-active DAB-COF to form a hybrid. The hybrid was used as an electrode to fabricate compressible supercapacitors, which delivered a C_s of 129.2 F g^{-1} at 0.5 A g^{-1}. 3D porous kenaf stem-derived carbon (3D-KSC) exhibited well-aligned macropores, which were used to assemble hybrids with COF and redox-active polyaniline.[171] CNT films were also used to assemble composite membrane electrodes.[172] A redox-active Quinone containing COF was also synthesized *in-situ* by a quasi-solid state reaction. A paste containing the monomer was mechanically ground to form a dough and pressed into the CNT film. After brief heating and washing, the resulting hybrid film electrodes delivered a C_s of 425 F g^{-1} in a 2 M H_2SO_4 electrolyte. They were further fabricated into stretchable and bendable solid-state supercapacitors.

Controlling the morphology of COFs in hybrids is essential to achieve good electrochemical performance. Recently, Liu and co-workers applied a reversible polycondensation-termination method to grow vertically aligned COF nanoplates on rGO-based 3D macroporous graphene aerogel (GA).[173] Monofunctional competitors (benzaldehyde and aniline) were added with COF monomers to regulate the reaction rate and self-coagulation of COFs, resulting in direction-controlled growth of high-crystalline COF nanosheets. The v-COF-GA hybrid exhibited a hierarchically porous structure, delivering a specific surface area of 282 $m^2 g^{-1}$, much higher than that of plain COF layers deposited on the GA (73 $m^2 g^{-1}$). The v-COF-GA hybrid showed a C_s of 289 F g^{-1} at 0.5 A g^{-1}. The good conductivity and improved electrolyte ion diffusion in v-COF-GA also led to improved rate performance. It retained 77% capacitance when the current density was increased from 0.5 to 50 A g^{-1} or 74% when the electrode mass loading was increased from 1.2 to 10.4 mg cm^{-2}.

Owing to their ordered pore structures, COFs have been used as a template or a spacer to modify other redox-active materials. Zhao and co-workers synthesized a series of $[C_{60}]_X$-COF hybrids using a COF as an ordered porous template to embed zero-dimensional C_{60} fullerene particles.[174] The COF was synthesized by using 1,3,5-tri-(4-aminophenyl)benzene (TAPB) as the vertices. At a molar ratio of 3:1 between the 2,5-dihydroxyterephthalaldehyde (DHTA) and 2,5-bis(3-azidopropoxy) terephthalaldehyde (BATA) monomers, the resulting COF exhibited well-aligned pores of ~2 nm to host functionalized C_{60} by an azide-alkyne "click" reaction (Figure 3.5h). At the optimal C_{60} mass loading of 5 wt%, $[C_{60}]_{0.05}$-COF exhibited a C_s of 63.1 F g^{-1} at 0.7 A g^{-1} and

retained 99% capacitance after 5000 charge/discharge cycles. In another study, Vaidhyanathan and co-workers further loaded redox-active and conductive polypyrrole into COFs nanochannels and constructed a Ppy@COF hybrid, which exhibited a nearly 10,000-fold increased electrical conductivity.[175] The synergies between polypyrrole and redox-active imide linking bonds in the COF provided a high areal specific capacitance of 358 mF cm^{-2} at 1 mA cm^{-2} in a carbon-free quasi-solid-state capacitor.

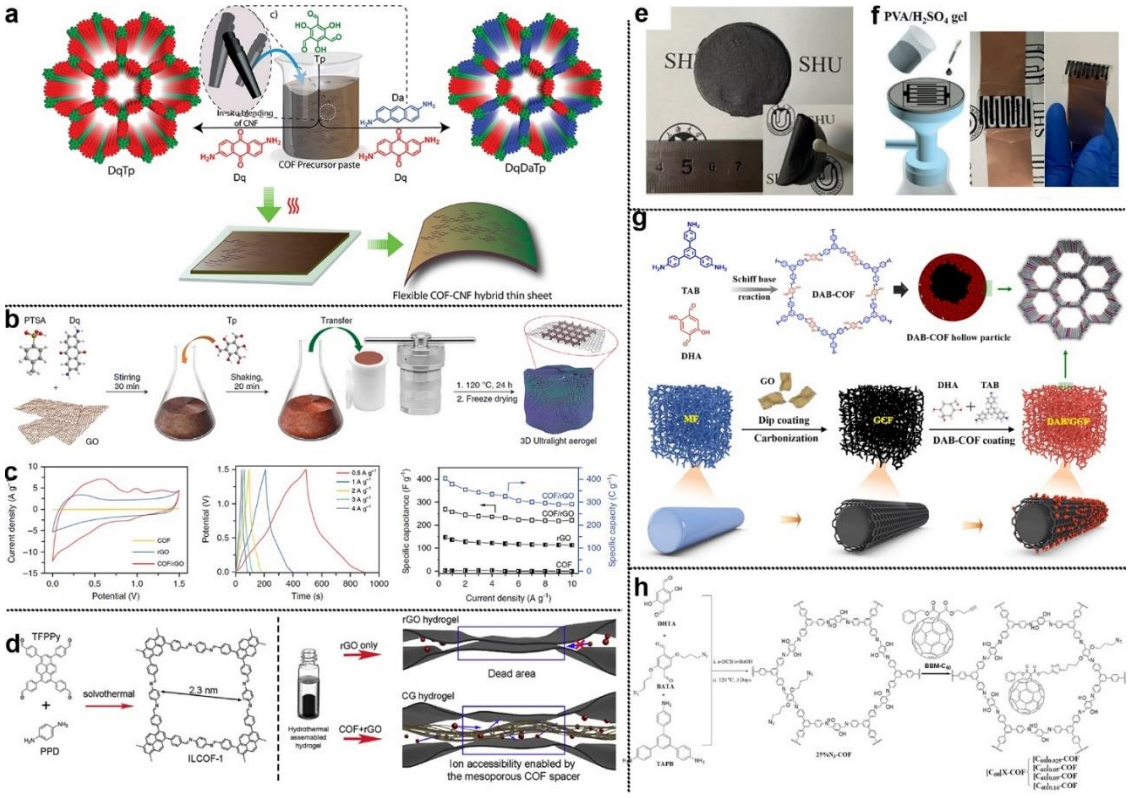

Figure 3.5. (a), The synthetic scheme of CNF-based flexible COF hybrid thin films.[161] (b), *In-situ* synthesis of a COF/rGO aerogel and (c), its electrochemical performance.[164] (d), *Ex-situ* assembly of COF-rGO hybrid by hydrothermal treatment.[167] (e), A COF-rGO freestanding hybrid film prepared by vacuum filtration and (f), its application for micro-supercapacitors.[168] (g), The multi-step formation of DAB/GCF 3D hybrid.[170] (h), Embedding functionalized C_{60} particles in COF pores by an azide-alkyne "click"

reaction.[174]

3.3.4 COF-derived carbon materials

COFs can be carbonized into various porous carbon materials with controlled morphologies, elemental compositions, and improved electrical conductivity. Abundant heteroatoms in COFs can be partially retained in the resulting carbon materials as heteroatomic dopants, providing pseudocapacitance. Carbonization temperature can significantly impact the properties of the resulting carbon materials. Meanwhile, various hard templates, pore formation agents and post-synthetic activation have also been explored to control the pore structure of the resulting carbon materials.

For example, in a recent study, carbonization temperature was found to significantly impact the porous structure of carbon materials derived from an imine-linked triazine COF (TACOF1).[176] Mesopores were dominant (43% of total pore volume) in carbon materials obtained at 800 °C (TACOF1-800), which was much higher than that of carbon materials obtained at 700 °C (21%) and 600 °C (13%). Consequently, the optimal TACOF1-800 showed a large specific surface area of 1194 $m^2 g^{-1}$ and a C_s of 124 $F g^{-1}$ at a current density of 0.1 $A g^{-1}$.

Various methods have been used to control the pore structure of the carbon materials derived from COFs. For example, a hard templating method was used to obtain a N and B co-doped porous carbon material (BN–C) from a Cu@BN-COF core-shell structure.[177] The COF shell was synthesized from condensation of melamine (MA) and 4-formylphenylboronic acid (4-FPBA) on a $Cu_2(NO_3)(OH)_3$ core, followed by

subsequent pyrolysis and template removal via acid-leaching (Figure 3.6a). The carbon material obtained at 1000 °C (B-N-C-1000) exhibited abundant mesopores and specific surface area of 399.4 m^2 g^{-1}, and high N content of up to 6.29 at%, resulting in a C_s of 230 F g^{-1} at a current density of 5 A g^{-1} in a three-electrode test. The porous structure further showed a good rate capability, retaining ~86% capacitance at 100 A g^{-1}. However, the B-N-C-1000 carbon lost ~15% of its capacitance after only 1400 charge/discharge cycles. Hao and co-workers showed that the pore structure of COF precursors impacted the pore structure of carbon materials obtained by $ZnCl_2$ ionothermal treatment.[178] By reacting a benzotrithiophene tricarbaldehyde (BTT) center block with size-varied linker monomers, *i.e.*, 1,1'-biphenyl-4,4'-diamine (DADP), *p*-phenylenediamine (DAB), and 1,3,5-tri(4-aminophenyl)benzene (TAB), a series COFs (BTT-DADP, BTT-DAB, and BTT-TAB) with varied pore sizes (2.17, 1.87 and 1.36 nm, respectively) were obtained. After carbonization at 700 °C, expanded mesopores of 3.38, 2.74 and 2.70 nm were found in the resulting carbon materials, respectively, exhibiting a similar pore size changing trend. Electrochemical tests showed that these carbon materials' specific capacitance depended on their specific surface area and the content of carbon in sp^2-hybridization. It is noteworthy that the $ZnCl_2$ ionothermal method used helped retain mesopores.

Post-synthetic activation methods have also been utilized to control COF-derived carbon materials' pore structures. B_2O_3 impurities generated from the pyrolysis of a boronic ester-linked COF-5 blocked the pores in the resulting carbon materials.[179] Washing the carbon materials with the water removed B_2O_3 and increased their specific

surface area from 26 to 525 m ^{2} g^{-1}. After pulverizing at the optimal condition, the resulting carbon materials (PCCOF-5) delivered a C_s of 82.9 F g^{-1}. In anaother study, Shim *et al.* examined the impact of CO_2 activation temperature on a COF-derived carbon material (Figure 3.6b).[180] The COF was prepared by cyanuric chloride and 1,3,5-triphenylbenzene *via* Friedel-Crafts reaction. Carbon materials with abundant micropores of 0.5 - 1.5 nm were obtained after carbonization at 900 °C. CO_2 activation at a moderate temperature of 900 °C introduced additional mesopores (Figure 3.6c and d) and increased the specific surface area from 988 to 1290 m^2 g^{-1}, resulting in a 28% higher C_s of 278 F g^{-1} at 1 A g^{-1}.

COF-based hybrid materials can also serve as precursors to obtain carbon materials. COF-1 nanoplates with a thickness of 3~15 nm were grown vertically on GO nanosheets by pre-grafting the benzene-1,4-diboronic acid (DBA) monomer on GO (DBA-GO, Figure 3.6e).[181] New mesopores with a diameter of 3~4 nm were created, offering a hierarchical pore structure beneficial for electrolyte filtration. The pre-grafted monomer was the key to guiding the formation of vertically aligned COF nanosheets, as confirmed by the different surface morphology found under scanning electron microscope (SEM) observation in Figure 3.6f. Carbonization in molten $ZnCl_2$ (m.p. = 290°C) at 600 °C largely retained the hybrid structure and preserved a large specific surface area of 500 m^2 g^{-1}. At an optimal DBA to GO mass ratio of 3:1, the resulting v-CNS-RGO-3 carbon exhibited a C_s of 165 F g^{-1} at a current density of 1 A g^{-1} and maintained its initial specific capacitance after 3000 charge/discharge cycles. In another work, Sun *et al.* showed that carbon materials obtained from the pyrolysis of a triazine COF grown *in-situ* on GO

nanosheets delivered better electrochemical performance than that obtained from post-synthetic physical mixing, pinpointing the importance of the precursor assembly method on the performance of resulting carbon materials.[182]

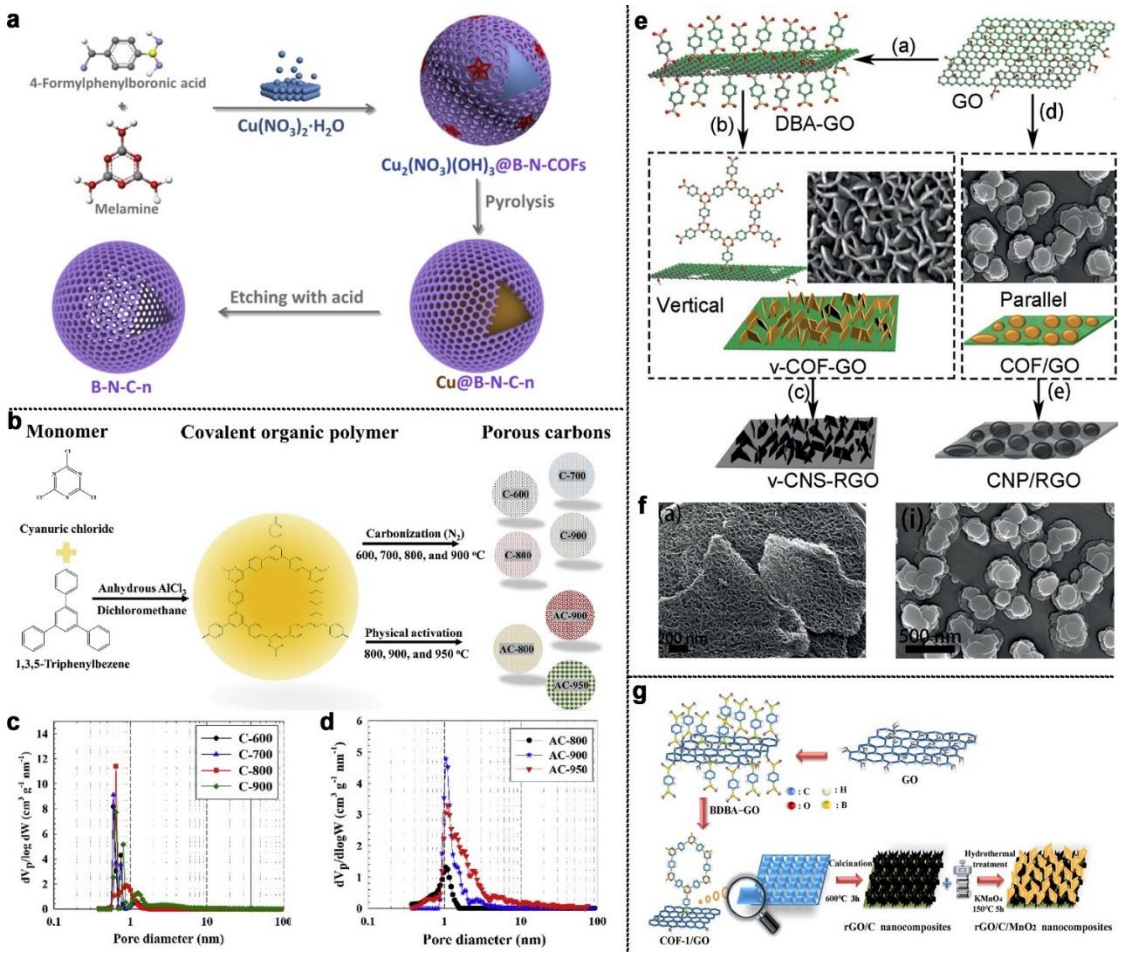

Figure 3.6. (a), The synthesis scheme of B-N-Cs.[177] (b), The synthetic scheme and pore size distribution of carbon materials (c), before and (d), after CO_2 activation.[180] (e), The synthesis scheme of v-CNS-RGO, and (f), SEM images of the hybrid obtained with (left) and without (right) pre-grafted DAB monomers.[181] (g), The method of using a COF-derived carbon hybrid as a support for loading MnO_2.[183]

The unique porous structure and good electrical conductivity of COF-derived carbon

materials make them suitable scaffolds for loading pseudocapacitive materials. For example, an MPC/PPy composite was prepared by electrochemical polymerization of redox-active polypyrrole (PPy) on a microporous carbon film (MPC) obtained by thermal annealing of COF nanoparticles (SNW-1).[183] The abundant micropores and large specific surface area of 679 $m^2 g^{-1}$ resulted in an areal specific capacitance of 2.55 F cm^{-2} at a current density of 3 mA cm^{-2}, which was an order higher than the 0.24 F cm^{-2} of the pristine MPC. MnO_2 can also be loaded on COF-derived carbon materials.[184] Moreover, the COF nanosheets vertically grown on GO sheets can be carbonized to serve as a conductive scaffold for hosting MnO_2 (Figure 3.6g), affording a C_s of 215.2 F g^{-1} at 0.15 A g^{-1}.[185]

3.4 Conclusion, challenges, and outlooks

COFs are a relatively new family of capacitive materials for supercapacitor applications compared to other commonly used carbon materials. Since the first report in 2013,[139] extensive efforts have been devoted to improving the energy storage performance of COF-based supercapacitors. Such research interests are inspired by the unique physiochemical properties of COFs, *i.e.*, designable pore structures, abundant and highly accessible surface area, and redox-active species. In the past five years, the C_s of COFs reached 470 F g^{-1} for EDLC and over 1400 F g^{-1} for pseudocapacitance.[141, 148] COF-based hybrid materials with other electrically conductive materials enhance their electrical conductivity and specific surface area, resulting in even better energy storage performance. Further, abundant heteroatoms in COFs, such as N, S, and P, make them

promising precursors to form heteroatom-doped porous carbon materials for supercapacitors. Tremendous research progress has been witnessed in the past few years. However, practical COF-based supercapacitors remain missing. Significant technological gaps exist in the following aspects, including COF structural controls, material processibility and scalability, and supercapacitor device designs, preventing practical applications.

COF structural controls in pore structures, chemical/electrochemical stability, electrical conductivity and crystallinity. The energy storage performance of COFs relies on their structures, particularly pore structures, chemical stability, electrical conductivity, and crystallinity.

COFs with various pore structures have been explored for supercapacitor applications. However, a comprehensive understanding of the correlations between COFs' energy storage performance and their pore structures remains elusive. Because of their versatile and rigorous synthesis chemistry, COFs with pores of identical chemical properties, such as steric effects, surface wetness to electrolytes, and functional groups, can be obtained. COFs can also offer size-tunable pores in a much wider range, up to 10 nm,[186] compared to the narrower range of metal-organic frameworks (*e.g.*, 0.81 to 2.34 nm[187]). Compared to carbon materials' tortuous and irregular pore structures, COFs' well-aligned pores are much easier to be characterized by common experimental tools and modelled using theoretical tools. Thus, we expect well-designed COFs to serve as unique models for experimental and theoretical studies of nanoscale charge transfer and adsorption behaviors. The improved understanding can in turn accelerate the development of COFs

with suitable pore structures for supercapacitor applications.

Chemical/electrochemical stability is another critical issue. The synthesis of high-quality COF crystals requires suitable linking covalent bonds with good reversibility to allow efficient bond self-correction and rearrangement. Many recently reported high-quality COF crystals are relatively stable in common aqueous and organic electrolytes. For example, imine bonds are widely used in COFs for supercapacitor applications because they have better stability than hydrolytic boroxine and boronate ester bonds.[132a] The chemical stability of COFs can be enhanced by several methods, such as irreversible tautomerization, post-synthetic modification, and aromatization. These efforts have created stable COFs even in strong acidic and basic electrolytes.[134, 188] However, in most studies, fast capacitance loss is still observed, especially when linking bonds in COFs are redox active.[145] Current studies often ignored the stability of many redox-active species incorporated in COFs, such as pyridines, quinones, porphines, and transitional metals. However, these redox-active species often strongly influence COFs' performance stability. For example, redox-active benzoquinone (Hex-Aza-COF-2) quickly lost 10% of its capacitance within about 1000 charge/discharge cycles,[145] while a PT-COF utilizing porphine redox lost 9% its capacitance after 3000 charge/discharge cycles.[148] Moreover, non-redox active regions in COFs also experience electrochemical degradation during charge/discharge cycles. Therefore, a better understanding of the capacitance degradation mechanism in COF-based materials is essential. While the performance loss due to EDLC or pseudocapacitance can be distinguished by performing the Trasatti and Dunn analysis,[189] chemical structure alternations require careful

monitoring using *in/ex-situ* and *operando* characterization tools.[190] Theoretical simulations may help to accelerate the rational design and screening of redox-active sites to create COFs with better stability.[191]

Poor electrical conductivity is another challenge for COFs to serve as effective capacitive materials. The electrical conductivity of pristine COFs is far inferior to that of carbon materials. The electrical conductivity of COFs used in most COF-based supercapacitors was not reported currently, which makes it more challenging to address this problem. In principle, the electrical conductivity of COFs can be improved by controlling their building blocks, linking covalent bonds, and crystallinity to build a more extensive conjugated π-electron network that would enable efficient charge transfer in delocalized π-electrons. Highly conjugated building blocks that provide more delocalized π-electrons are favored. However, such building block molecules often exhibit low solubility in most solvents, hindering their uses in COF synthesis in commonly used solvothermal methods. Some linking bonds may help to extend the π-conjugation between various building blocks. Aromatic imine-type linking bonds (*e.g.*, triazine, phenazine, and thiazole) are one promising candidate, as reflected in their dominating positions in recently published studies (see Table 1, Column 2). We propose that further research should further expand to other linking bonds. For example, a conjugated sp^2c-COF based on an sp^2-alkene bond exhibited improved charge transport performance.[192] COFs with enhanced electrical conductivity were also constructed from *sp*-alkyne bonds following the concept of conductive graphdiynes.[193] However, the synthesis of COFs using carbon-carbon linking bonds remains challenging.

The crystallinity of COFs directly impacts their specific surface area and pore alignment. The random conformation in COFs with poor crystallinity also breaks the conjugated π-electron alignment, resulting in significantly reduced electrical conductivity and electrochemical performance.[194] Synthesizing highly crystalized COFs is thermodynamically unfavoured compared to their amorphous or polymorph counterparts. Significant progress has been made in obtaining high-quality COF crystals by controlling reaction conditions, linking bonds, substituents on the building monomers, and more.[195] However, most of these methods require a long reaction time or only apply to small amounts of samples, which are still insufficient for practical supercapacitor applications. Novel synthesis approaches are needed to realize the efficient production of COFs with good crystallinity in bulk.

Material processibility and production scalability. As-prepared COFs are usually in powder form and insoluble in most solvents. For electrode and supercapacitor fabrication, they must be adequately exfoliated and suspended in a suitable solvent (*e.g.*, N-methyl-2-pyrrolidone).[196] Sonication or ball milling have been extensively used to prepare COF-based hybrids by mixing COFs with polymeric binders and electrically conductive additives. However, these methods have low productivity. They cause inevitable COF nanosheet stacking and crystal misalignment. They also introduce structural damages that are detrimental to the quality of resulting electrodes and supercapacitors. Current COF exfoliation methods require significant innovation and extensive optimization to improve material processability.

Recently, chemical exfoliation by protonation, defect-assisted and modification-

assisted methods have emerged as promising alternatives. However, controlling the thickness and lateral dimension of resulting COF nanosheets remains difficult. Novel chemical processing methods that could offer high-quality and precise dimension control at a large scale are highly desired. Some techniques used in exfoliating and suspending Mxenes and graphite, *e.g.*, using surfactants as a stabilizer or electrochemical exfoliation, may open new avenues for processing COF materials in bulk.[197]

Alternatively, direct synthesis of mechanically robust COF thin films is an appealing approach. COF thin films can be used as freestanding electrodes, avoiding polymeric binders, which may block COFs' pores. However, current COF thin film preparation methods require dedicated controls and are challenging to scale. Using properly designed reactors and optimized reaction conditions, some recently demonstrated COF thin-film synthesis methods at the liquid/air interface and liquid/liquid interface may offer an excellent opportunity to address this problem.[198]

Supercapacitor device designs. Many devices structural parameters, such as electrolytes, symmetric/asymmetric cells, mass loading of active materials in electrodes, and electrode thickness, can strongly influence the electrochemical performances of COF-based supercapacitors. As shown in Table 3.1, most current studies have used aqueous electrolytes, which limit device potential windows and energy density. Hydrophobic COFs may also have poor wetting in aqueous electrolytes.[199] Organic electrolytes and ionic liquids may expand the operating voltage window and facilitate efficient electrolyte infiltration if they could have better wetting with COFs. It should be noted that the pore size of COFs can be engineered to facilitate the mass transfer of

organic electrolyte molecules that often are larger than the size of water. Although device energy density can be increased in asymmetric hybrid capacitors fabricated using redox-active COFs, the mass loading of active materials in electrodes is critical. The mass loading carbon materials in practical supercapacitors is ~10 mg cm $^{-2}$.[200] In contrast, none of the recent studies of COF-based supercapacitors has reached this level of mass loadings, as summarized in Table 1. Table 1 also shows that only half of the studies reported the mass loading of COFs in tested electrodes. Only three studies evaluated how the mass loading of active materials affected their electrochemical performance. In future studies, the mass loading should be appropriately reported and examined to realize practical applications. Moreover, the versatility of COFs may also help to create multifunctional supercapacitors. For example, sensing and electrochromic-responsive[201] properties may be introduced into COF-based supercapacitors.

In summary, significant development of COF-based supercapacitors has been made in the past few years. From the current accomplishments highlighted above, we propose that future research should focus on addressing technological gaps to realize practical COF-based supercapacitors. As an emerging family of electrochemically active materials, we hope versatile COFs can eventually become an essential material in real-world applications.

Table 3.1. Summary of electrochemical performance of COFs as electrode materials in supercapacitors.

Electrode material	Linkage	Redox groups	SSA, $m^2\ g^{-1}$	Electrolyte	Potential window, V	Mass loading, mg cm^{-2}	Three-electrode performance	Two-electrode device performance			Ref.
							C_s, F g^{-1}@A g^{-1}	C_s, F g^{-1}@A g^{-1}	P, W kg^{-1}	E, Wh kg^{-1}	
EDLC											
TFP-NDA-COF	β-ketoenamine	-	353	1 M H_2SO_4	0 to 1	-	379@2 [a]	-	247	48.3	[140]
TPDA-1	β-ketoenamine	-	545	1 M H_2SO_4	0 to 1	-	469.4@2 [a]	-	3365.38	24.3	[141]
e-COF	Imine	-	1170	1 M NBu_4BF_4/ACN [h]	0 to 1.3	0.678	-	5.46 @1000 [a]	55000	-	[142]
TAPB-BTCA-ECOF	Imine	-	470	1 M H_2SO_4							[143]
				6 M KOH	-0.2 to 0.4	9.95	11.2 [c]@100 [a]	9.55 @1000 [a]	-	-	
				0.25 M $TBAPF_6$/ACN [h]							
Pseudocapacitance											
TDFP-1	Imine	Imine protonation	651	0.1 M H_2SO_4	-0.5-0.5	-	418@0.5	-	-	-	[144]
Hex-Aza-COF-3	Imine	Phenazine	124	1 M H_2SO_4	-1 to 0	-	663@1	64@1	661.2	23.3	[145]
TPT-DAHQ COF	C-C	Benzobisoxazole	1855	1 M KOH	-1 to 0	-	256@0.5	-	-	43	[146]
PDC-MA-COF	Imine	Triazine	748.2	6 M KOH	0 to 0.5	6.85	335@1	331@1	750	29.2	[147b]
FCTF	Triazine	Triazine	1345	1 M H_2SO_4	0 to 0.8	1.5	379@1	148@1	975	46.3	[147c]
DDP-based CTFs	Triazine	Triazine	2275	0.5 M in ACN	-0.5-0.5	3	270.7@10 [a]	118@0.5	7500	147.5	[147d]
NDTT	C-C	Naphthalene diimides	32.5	1 M KOH	-0.3 to 0.7	2	425.3@0.2	-	-	33.2	[147e]
PT-COF	Imine	Porphyrin	1998	0.5 M H_2SO_4	0 to 1	0.285	1443@1	-	7300	200	[148]
Ni-COF	Imine	Quinone and Ni(II)	362	3 M KOH	0 to 0.6	5	1257@1	417@1	839	130	[149]
Co-COF TAPB-DHPA	Imine	Co (II/III)	87.7	PVA/H_3PO_4 [h]	0 to 0.7	-	-	1.8 [c]@10 [a]	5.9 [f]	230.4 [g]	[150]
TpPa-$(OH)_2$	Imine	Benzoquinone	369	1 M phosphate buffer	-0.2 to 0.5	0.2	416@0.5	214@0.2	1956	29	[120b]

TpOMe-DAQ COF	β-ketoenamine	Hydroquinone	1734	2 M H_2SO_4	−0.5 to 0.5	9.5	135@3.3 [b]	8.8	61.8 [d]	2.9 [e]	[152]
TTF-COF1	Imine	Benzoquinone	729	3 M KOH	0 to 0.5	5	752@1	183@1	858	57	[151]
TTF-COF1	Imine	Benzoquinone	729	3 M KOH	0 to 0.5	5	752@1	183@1	858	57	[151]
IISERP-COF10	β-ketoenamine	Pyridine	1233	1 M H_2SO_4	0 to 0.8	-	546@0.5	92@0.5 [b]	-	98 [e]	[156]
IISERP-COF11	β-ketoenamine	Pyridine	921	1 M H_2SO_4	0 to 0.8	-	310@0.5	32@0.5	-	102 [e]	[156]
IISERP-COF12	β-ketoenamine	Pyridine	1067	1 M H_2SO_4	0 to 0.8	0.12	400@0.5	57@0.5 [b]	-	140 [e]	[156]
DqTp	β-ketoenamine	Anthraquinone	940	1 M H_2SO_4	-0.7-0.3	-	154@ 1.56 [b]	12 @0.39 [b]	980 [d]	0.43 [e]	[157]
Dq_2Da_1Tp COF	β-ketoenamine	Anthraquinone	1004	1 M H_2SO_4	-0.7-0.3	-	122@ 1.56 [b]	-	-	-	[157]
Dq_1Da_1Tp COF	β-ketoenamine	Anthraquinone	804	1 M H_2SO_4	-0.7-0.3	-	111@ 1.56 [b]	8.5 @0.39 [b]	960 [d]	0.3 [e]	[157]
Dq_1Da_2Tp COF	β-ketoenamine	Anthraquinone	1400	1 M H_2SO_4	-0.7-0.3	-	76@ 1.56 [b]	-	-	-	[157]
DaTp	β-ketoenamine	-	577	1 M H_2SO_4	-0.7-0.3	-	<10@ 1.56 [b]	-	-	-	[157]
TAPT-2,6-NA$(OH)_2$ COF	Imine	Dihydroxynaphthalene	1089	1 M KOH	-0.8 to 0.2	-	190@0.5	-	-	-	[158]
TAPT-2,3-NA$(OH)_2$ COF	Imine	Dihydroxynaphthalene	429	1 M KOH	-0.8 to 0.2	-	271@0.5	-	-	-	[158]
3D-Sp-COF@96 h	Imine	?	1016	6 M KOH	0 to 0.4	-	251@0.5	-	-	-	[159]
Hybrids											
DqTp-CNF	β-ketoenamine	Anthraquinone	472	1 M H_2SO_4	-0.5 to 0.5	-	464 @0.25 [b]	-	-	-	[161]
DqDaTp-CNF	β-ketoenamine	Anthraquinone	532	1 M H_2SO_4	-0.5 to 0.5	-	364 @0.25 [b]	167@0.5 [b]	125 [d]	5.8 [e]	[161]
COF/CNT-0.5	β-ketoenamine	Pyridine	398	1 M H_2SO_4	-0.2 to 0.8	1	357 @ 0.5	97@0.5	250	13.5	[162c]
c-CNT@COF-3	β-ketoenamine	Anthraquinone	576.7	0.5 M H_2SO_4	-0.3 to 0.3	0.5	418.7@0.2	123.2@0.2 [b]	591.9 [d]	30.7 [e]	[162b]
SWCNTs-TpPa-COF	β-ketoenamine	Quinone	235.5	1 M H_2SO_4	-0.2 to 0.8	-	153@0.5	-	-	-	[162a]
CNT/NKCOF-2	Azo	Azo groups	609	2 M H_2SO_4	-0.2 to 1	2	440@0.5	263@1	42000	71	[155]
PAI@40%CNT	Imide	Amine	386	1 M Na_2SO_4	-1 to 0	-	278@0.5	95@0.5	357.2	25.9	[163]
COF/rGO	β-ketoenamine	Anthraquinone	246	0.5 M H_2SO_4	0 to 1.5	-	-	269@0.5	-	-	[164]
$COF_{BTA\text{-}DPPD}$-rGO	Imine	Pyridine	371	2 M KOH	0 to 0.5	3	239.1@0.5	-	-	-	[165]

COF@MXene-15	β-ketoenamine	Anthraquinone	621	1 M Na_2SO_4	-0.9 to -0.1	-	290@0.5	-	-	-	[166]
rGO/COF-20	Imine	Oxygeneous groups	-	1 M H_2SO_4	0 to 1	0.2	321@1	74@0.1	50	10.3	[167]
COF/rGO-30	Imine	Pyridine	386	1 M H_2SO_4	-0.3 to 0.7	0.5	599@0.5	138@0.5	250	20.1	[168a]
DAAQ-COFs/GA	β-ketoenamine	Anthraquinone	425.3	1 M H_2SO_4	-0.5 to 0.5	0.36	378@1	112@1	700	30.5	[168b]
COF@rGO-2	β-ketoenamine	Anthraquinone	432	1 M H_2SO_4	-0.3 to 0.7	-	451.96@0.2	-	500	44.22	[169]
DAB/GCF	Imine	Anthraquinone	279	1 M H_2SO_4	0 to 1	-	-	129.2@0.5	125	4.47	[170]
3D-KSC/COF-LZU1/PANI	Imine	Polyaniline	31.7	0.1 M H_2SO_4	-0.2 to 0.8	-	583@0.1	-	-	-	[171]
CHCM	β-ketoenamine	Quinone	167	2 M H_2SO_4	-0.4 to 0.4	-	425@1.33 [b]	-	-	-	[172]
v-COF-GAs	Imine	-	282	1 M H_2SO_4	0 to 0.8	1.2-10.4	-	289@0.5	-	-	[173]
$[C_{60}]_{0.05}$-COF	Imine	Azide groups	320	1 M $NaSO_4$	0 to 0.5	1.8-2.2	63.1@0.7	53.3@1	900	21.4	[174]
Ppy@COF	Imide	Polyimide	657	1 M H_2SO_4/ PVA	0 to 2.5	-	1.983@1	358@1 [b]	4509 [d]	145 [e]	[175]
COF derived materials											
$TACOF_1$-800	Azine	-	1194	6 M KOH	-1 to 0	0.4	124@0.1	-	-	-	[176]
B-N-C-1000	Boroxine	-	399.4	6 M KOH	-1 to -0.4	-	230@5	-	-	-	[177]
PCCOF-5	Boronic ester	-	689	1.0 M $TEABF_4$/PC [h]	0 to 2.5	-	82.9@0.04	-	-	-	[179]
AC-900	C—C	-	1290	6 M KOH	-1 to 0	2.5-3	278@1	-	-	-	[180]
BTT-DADP COF-700	β-ketoenamine	-	121.4	6 M KOH	0 to 0.55	1 mg	407@1	90@1	800	32.1	[178]
v-CNS-RGO	Boroxine	-	500	6 M KOH	-0.5 to 0.5	-	165@1	-	-	-	[181]
N-doped C/rGO	Imine	-	300	6 M KOH	-1 to 0	10	215@0.5	161.8@0.5	14.3	400	[182]
MPC/PPy	β-ketoenamine	-	679	1 M KOH	-0.8 to 0.1	-	2.55@3 [b]	-	-	-	[183]
N-PC/α-MnO_2	C—C	-	245	1.0 M Na_2SO_4	-1 to 0	-	525.7@1	-	-	-	[184]
rGO/C/MnO_2	Boroxine	-	129.79	3 M KOH	0 to 0.6	3.22	215.2@0.15	59.5@0.16	3600	21.2	[185]

[a] Based on the mass of the supercapacitor device; [b] Specific Capacitance in a unit of mF cm^{-2}; [c] Power density in μW cm^{-2}; [d] Energy density in

μWh cm^{-2}; [e] Power density in W L^{-1}; [f] Energy density in Wh L^{-1}; [g] Specific Capacitance in mAh g^{-1}. [h] Abbreviation: ACN - acetonitrile; $TEABF_4$ - tetraethylammonium tetrafluoroborate; PC - propylene carbonate; PVA - polyvinyl alcohol

Chapter IV. COFs in Oxygen Reduction Reactions (ORR)

Metal-nitrogen-carbon (M-N-C) single-atom catalysts (SAC) have gained significant attention as ideal electrocatalysts due to their high catalytic activity and excellent electronic properties. However, further investigations are required to understand their catalytic activity, site distribution at different pH values and pH dependence. In this study, we employed a coaxial one-dimensional van der Waals heterostructure (1D vdWH) composed of a COF shell with a carbon nanotube (CNT) core that can be supplied with metal coordination sites. Five different transition metals exhibited similar pH-dependent activity trends during the oxygen reduction reaction. However, the influence of pH on the catalytic activity varied significantly among different metals. Therefore, studying the effect of pH on the catalytic activity of M-N-C SACs and precisely pinpointing the distribution of internal active sites is of paramount importance for the design and synthesis of more efficient electrocatalysts.

4.1 Introduction

ORR is considered to be an effective pathway to provide renewable and clean energy sources.[202] However, the sluggish kinetics of ORR has hindered the performance of many energy storage and conversion devices such as fuel cells, water electrolysis, and metal-air batteries.[203] Currently, the most efficient catalysts for ORR are precious metal-based electrocatalysts, including platinum (Pt), ruthenium (Ru) and iridium (Ir). However, their high cost and limited availability on Earth restrict their widespread application.[204] Recently, single-atom catalysts based on transition metals (Mn, Fe, Co,

Ni, Cu, Zn) have been extensively studied as potential alternatives to precious metal-based catalysts.[205] For instance, Co-N-C SACs can be used for the oxygen evolution reaction (OER) as they can reduce oxygen via 2-electron pathway ($2e^-$ ORR) to produce hydrogen peroxide (H_2O_2). On the other hand, Mn-N-C SACs exhibit high selectivity for the 4-electron transfer ($4e^-$ ORR) transfer, leading to the production of water (H_2O), which makes them suitable for hydrogen evolution reaction (HER).[206] Furthermore, the superior catalytic performance and selective properties of M-N-C SACs result from their maximum atomic utilization and specific active sites. At the same time, the strong coordination between metals and doped N atoms, as well as the interactions with carbon-based materials, can prevent the aggregation of single atoms and thus enhance their stability.[207]

SACs containing different transition metals have received significant attention as promising catalysts for ORR. Li *et al.* synthesized an electrocatalyst Cu-N-C SAC consisting of uniformly dispersed copper (Cu) atoms which were embedded in nitrogen-doped carbon nanosheets.[208] The Cu-N-C SAC exhibited several noteworthy features. Firstly, it had a high Cu content of 20.9 wt% and an abundance of active sites for Cu atoms. Secondly, the Cu-N-C SAC demonstrated superior ORR activity compared to commercial Pt/C catalysts, while exhibiting a similar onset potential and a lower Tafel slope (37 mV dec^{-1}) than that of Pt/C (84 mV dec^{-1}). Additionally, the Cu-N-C SAC exhibited a half-wave potential of 0.869 V, which was better than the value of 0.838 V for Pt/C. Moreover, the H_2O_2 production rate of Cu-N-C SAC was comparable to that of Pt/C.

Wang's group synthesized a Fe/N/C-SCN electrocatalyst using a pyrolysis method.[209] The catalyst exhibited high ORR activity in 0.1 M H_2, achieving a current density of approximately 23 A g^{-1} at 0.80 V, along with a remarkably low H_2O_2 yield (<1%). Furthermore, the Fe/N/C-SCN catalyst demonstrated a Tafel slope of 66 mV dec^{-1}, which is lower than that of Pt/C, indicating improved ORR kinetics. Additionally, Fe/N/C-SCN showed a better electrochemical stability compared to other catalysts. Sun and colleagues have developed a catalyst (Co-SAS/HOPNC) with an abundance of catalytic reaction sites, excellent electrical conductivity and a large surface area.[210] The catalyst exhibited outstanding ORR performance in alkaline media, which achieved a current density of 5.42 mA cm^{-2} at 0.90 V. Moreover, Co-SAS/HOPNC demonstrated a high half-wave potential ($E_{1/2}$) of 0.892 V, 53 mV higher than that of Pt/C. In addition, the Tafel slope of Co-SAS/HOPNC was 58 mV dec^{-1}, indicating fast kinetics.

Considerable research has been conducted to improve the catalytic performance of MNC SACs for ORR. To further investigate their catalytic activity in both acidic and alkaline ORR, the dependence of catalytic activity on pH and how different metals are influenced differently by pH. I propose the design of a model catalyst with a periodic repetitive structure and well-defined metal anchoring sites to accommodate a wide range of transition metals.

COFs present promising model catalysts due to their unique structure and properties. COFs are crystalline porous organic polymers composed of organic monomers which are periodically connected by covalent bonding.[44, 211] They possess tunable porosity,

large surface area, and excellent chemical stability and thermal stability, which makes them potential candidates for high-performance electrocatalysts.[212] Furthermore, COFs serve as ideal models for providing accurate and well-defined metal coordination sites. In addition, the distinctive porous structure of COFs can provide precise electrocatalytic active sites and facilitates rapid charge transfer pathways, thereby enhancing the catalytic activity and selectivity of the catalyst.[213]

Despite they show the potential as high-performance electrocatalysts, the inherent stacking of COF nanosheets leads to the concealment of numerous catalytic active sites and a reduction in specific surface area, which is detrimental to the transport of electrolyte ions. To overcome these challenges, we propose the incorporation of physical spacers.[214] CNTs are the optimal choice because CNTs not only prevent COFs from self-stacking and enable rapid transport but also facilitate charge transfer which can enhance their catalytic activity.[215]

I have successfully synthesized a coaxial 1D van der Waals heterostructure (vdWH) from COF and carbon nanotube by a bottom-up approach. The structure comprised a catalytically active porphyrin-based COF (COF-366) shell which wrapped around the exterior of a CNT core. Experimental investigations were conducted in electrolytes of varying pH values to explore the catalytic activity of different transition metals of Mn, Fe, Co, Ni, Cu and Zn. Results revealed that Fe exhibited the highest ORR activity among the transition metals in alkaline electrolytes. However, in acidic electrolytes, Co-COF366/CNT demonstrated the highest activity. This observation demonstrated the different influences of pH on various metals. Notably, the ORR activity of all metals in

alkaline catalysts surpassed the performance in acidic condition. The effect of pH on the activity of MNC SACs with different metals was further confirmed.

4.2 Experimental methods

4.2.1 Chemicals and Materials

Multi-walled carbon nanotube (MWCNT, diameter about 10~20 nm) was obtained from CNano Inc. 5,10,15,20-(Tetra-4-aminophenyl) porphyrin (TAPP, 98%) was purchased from PorphyChem, Inc. Terephthaldehyde (TPD, 99%), $Mn(OAc)_2$ (99.99%), $Fe(OAc)_2$ (99.99%), $Co(OAc)_2{\cdot}4\ H_2O$ (99.99%), Ni $(OAc)_2{\cdot}4\ H_2O$ (99.99%), $Cu(OAc)_2$ (99.99%), methanol (anhydrous, 99.9%), ethanol (200 proof, anhydrous, >99.5%), acetic acid (99.9%), mesitylene (98%), chloroform (>99.5%), N,N-dimethylformamide (DMF, anhydrous, 99.8%), H_2O_2 solution (30 wt%) and KSCN (99%) were purchased from Sigma-Aldrich. Argon (Ar, 5.0 grade), O_2 (5.0 grade) and 5% H_2/Ar gas cylinders were obtained from BOC Australia.

4.2.2 Purification of MWCNT

Before catalyst preparation, the as-received CNTs were purified by a multi-step purification approach. Briefly, the as-received CNTs were firstly subjected to mild-air oxidation at 300 °C in the air for 30 min to remove amorphous carbons. Afterward, the solids were refluxed in a 3 M alkaline NaOH solution for 1 hour to dissolve any catalyst template residues, *e.g.*, SiO_2, Al_2O_3, or MgO. The solids were recovered by filtration and washed with DI water repeatedly before they were further treated by 30 min sonication in 1 M HCl solution. The solid was further stirred at 70 °C for 5 hours. Then

the MWCNTs were collected by filtration and washed with DI water. After drying under vacuum for 8 hours, the MWCNTs were further thermally annealed at 1200 °C in 100 sccm 5% H_2/Ar flow for 1 hour and cooled to room temperature under the same gas atmosphere.

4.2.3 Synthesis of COF366/CNT

The COF-366 wrapped MWCNT catalysts were prepared by a solvothermal method. Briefly, about 0.02 mmol TAPP and 0.04 mmol TPD were added to a mixture of 1 mL of absolute ethanol, 1 mL of mesitylene, and 0.1 mL of 6 M acetic acid in a Pyrex tube. Purified CNT was added at a mass ratio of 2:1 to the COF-366 precursors. The mixture was then suspended and mixed by sonication for 30 min. The tube was then subjected to three-round freeze-thaw cycles using liquid N_2, preheated to 65 °C for 4 hours under Ar protection before further hydrothermally treated at 120 °C for 72 hours. The solid products were then recovered by filtration and washed with EtOH and DMAC repeatedly before being dried in a vacuum. The product is denoted as COF366/CNT and serves as the substrate to prepare M-COF366/CNT catalysts. These syntheses were repeated to accumulate enough material for the following metalation step.

4.2.4 Synthesis of M-COF366/CNT

Metallation of the COF366/CNT was then performed using various metal acetate salts as metal precursors. About 45 mg of the as-prepared COF366/CNT substrate and 0.27 mmol of the metal salts were suspended in 5 mL MeOH, followed by adding 20 mL $CHCl_3$ and 15 mL DMF. The mixture was bath sonicated for 60 min and further stirred at 80 °C under Ar protection for 24 hours. After cooling to room temperature, the solid

product was recovered by filtration and washed with DI water before being dried in a vacuum. The resulting catalysts were denoted as M-COF366/CNT, where M is Fe, Co, Ni, and Cu.

4.2.5 Material characterization

Thermogravimetric analysis (TGA) was performed on a TA Instrument TGA 5500 thermo analyzer under airflow (20 sccm). Liquid N_2 physisorption isotherms were collected on an Anton Paar Autosorb iQ analyzer. Metal residue in the purified CNT and metal loading in various catalysts were determined by inductively coupled plasma atomic emission spectroscopy (ICP-AES) on a Perkin Elmer Avio 500 spectrometer. The sample was acid digested in 6 M HNO_3 before dilution and measurement. X-ray photoelectron spectra (XPS) were obtained on a Thermo Scientific K-Alpha+ spectrometer with an Al-Kα source (1486.3 eV). Samples were loaded on a gold substrate. Survey spectra are obtained at a 1 eV step in CAE mode, with a pass energy of 200.0 eV. The high-resolution spectra were collected at a step of 0.1 eV. Transmission electron microscope (TEM) images and energy-dispersive X-ray (EDX) elemental analysis are collected on an FEI Themis-Z microscope under either bright-field high-resolution (BF-HRTEM) or high-angle angular dark-field scanning mode (HAADF-STEM) modes.

4.2.6 Electrocatalyst Performance Tests

The electrochemical performance of different catalysts was collected using a CHI760 electrochemical workstation and a Pine MSR rotator in a three-electrode configuration at 25 °C. A rotary ring-disk electrode (RRDE, E6R1, Pine Research, with a calibrated

collection efficiency *N*=0.249) equipped with a glassy carbon disk (GCD, 5 mm diameter) and a Pt ring (OD = 7.50 mm, ID = 6.50 mm). The electrode was polished using Al_2O_3 powder before each measurement. A pre-calibrated Ag/AgCl (3M KCl filling) reference electrode and a Hg/HgO (0.1 M KOH filling) reference electrode were used for the acidic 0.1 M $HClO_4$ and the alkaline 0.1 M KOH electrolytes, respectively. A graphite rod electrode (AFCTR3B, Pine Research) was used as the counter electrode. All reported potentials were calibrated to a reversible hydrogen electrode (RHE, V_{RHE}).

The catalyst ink was prepared by dispersing 5 mg of as-synthesized catalysts in 1 mL water/IPA solution (1/9 = v/v, containing 0.05% Nafion 117) by 30 min bath sonication. The freshly prepared ink was drop-casted on the GCD at a loading of 0.05 mg cm $^{-2}$. The catalyst was first stabilized by cycling between 0.2~1.2 V_{RHE} for 20 cycles at a scan rate of 50 mV s $^{-1}$. Afterward, a linear sweep polarization (LSV) curve was collected under Ar saturation at a scan rate of 5 mV s $^{-1}$, serving as a background for correction. Then the ORR performance of each catalyst was obtained by collecting the LSV curve in O_2 saturation at a scan rate of 5 mV s $^{-1}$. The Pt ring electrode was biased at 1.2 V_{RHE} to collect the ring current (i_{ring}). No *i*R-compensation was applied. The ORR test, the number of ORR electron transfers (n) and the selectivity for H_2O_2 formation (λ H_2O_2) are determined by the following equation:

$$n = 4 \times \frac{i_{disk}}{i_{disk} + i_{ring}/N}$$

$$\lambda_{H_2O_2} = \frac{2 \times i_{ring}/N}{i_{disk} + i_{ring}/N} \times 100$$

$$H_2O_2\% = 200 \times \frac{i_{ring}/N}{i_{disk} + i_{ring}/N}$$

where i_{ring} and i_{disk} are the currents obtained from the Pt ring and glassy carbon disk electrodes, respectively.

4.3 Results and Discussion

4.3.1 Physicochemical characterization of the purified CNT substrate

The carbon nanotube substrate was first purified by a multi-step method. The purity of the CNT was confirmed by TEM characterization, as shown in Figure 4.1a shown below. The CNT shows a clean surface. No observable amorphous carbon or metal nanoparticles can be found under the dark-field mode (Figure 4.1b). The TGA profile displayed in Figure 4.1c shows a fast mass loss starting at ~550 °C. No material loss at low-temperature region, *i.e.*, below 400 °C can be found, indicating a minimum amorphous carbon residue and good quality of the CNT. There are merely ~0.24 wt% remnants after thermal oxidation at 900 °C for 30 min, affording a carbon purity of 99.76 wt%.

XPS survey scan results displayed in Fig.4.1d show a strong C 1*s* peak at ~284 eV and a small amount of oxygen residue at ~530 eV. No Fe residue can be found at ~710 eV. The purified CNT is further acid-digested and ICP-AES measurement showed a small amount of Fe residue of about 0.09 wt%, which agrees well with the TGA analysis. The Raman spectrum of the CNT substrate is shown in Figure 4.1e. The intensity ratio (I_D/I_G) between the defect peak (D-band, at ~1350 cm^{-1}) and the graphitic peak (G-band, at ~1580 cm^{-1}) is about 0.873. Based on the N_2 physisorption isotherm displayed in

Figure 4.1f, the CNT substrate can offer a surface area of 162 m^2 g^{-1}. After all, the CNT shows good purity.

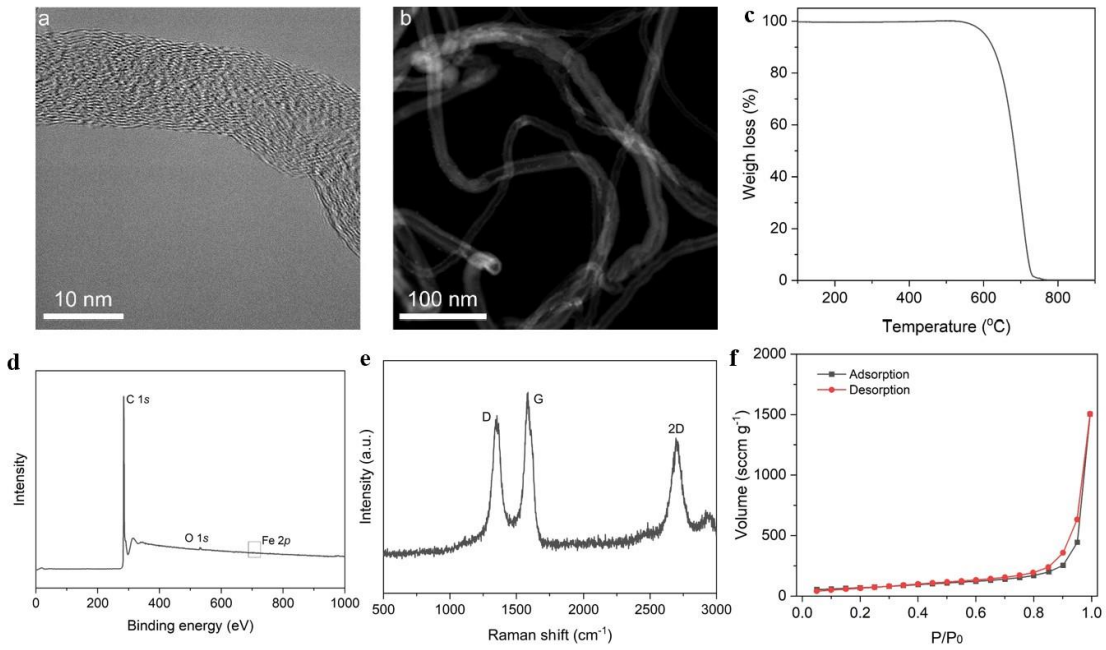

Figure 4.1. TEM images of the purified CNT substrate collected under (a), BF-HRTEM and (b), HAADF-STEM modes. (c), TGA profile, (d), XPS survey scan spectrum, (e), Raman spectrum, and (f), N_2 physisorption isotherm of the purified CNT sample.

The ORR activity of the purified CNT substrate is also assessed in O_2-saturated 0.1 M $HClO_4$ and 0.1 M KOH electrolytes, and the RRDE LSV curves obtained at a rotation speed of 1600 rpm and a catalyst loading of 0.05 mg cm^{-2} are shown in Figure 4.2. In the acidic electrolyte, the purified CNT substrate exhibits very poor ORR activity. The performance improved significantly in the alkaline 0.1 M KOH electrolyte, showing an onset potential at ~0.72 V_{RHE} on the disk electrode and reaching –0.92 mA cm^{-2} at 0.1 V_{RHE}. The main reason for the low catalytic activity under acidic electrolytes can be

attributed to the fact that acidic media are more corrosive than alkaline media and the nitrogen-containing active sites are susceptible to protonation, leading to failure in catalysing the ORR process.

However, these performances were much inferior to the M-COF366/CNT and FePc/CNT-R catalysts, suggesting the metal sites are the ORR active center.

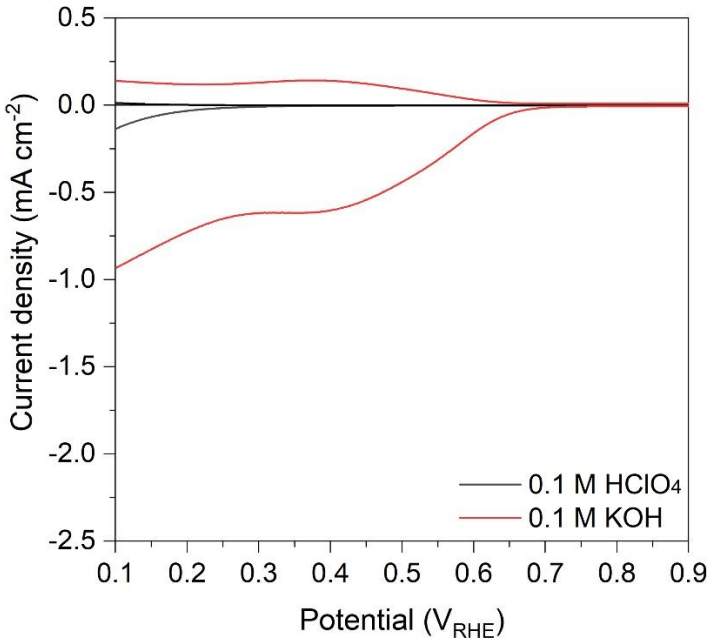

Figure 4.2. ORR LSV curves of the purified CNT in 0.1 M $HClO_4$ (black) and 0.1 M KOH (red) electrolytes.

4.3.2 Synthesis and characterization of M-COF366/CNT catalysts

A carrier COF-366 was constructed using 5,10,15,20-(Tetra-4-aminophenyl) porphyrin (TAPP) and terephthaldehyde (TPD) to facilitate the incorporation of different transition metals in the electrocatalyst M-COF366/CNT. The metal-N_4 (M-N_4) units, formed by the unique coordination bonds between the porphyrin moiety in TAPP and

transition metals, provide abundant metal catalytic active sites and can anchor metal atoms and prevent their aggregation.[216] COF-366 was selectively wrapped around the external surface of CNT using an in situ polymerization, forming a uniform and continuous shell. The new vibration peak found at 1625 cm^{-1} in the Fourier Transform Infrared Spectroscopy (FTIR, Figure 4.3) demonstrates the formation of an imine (–C=N–) bond and confirms the successful formation of COF-366.

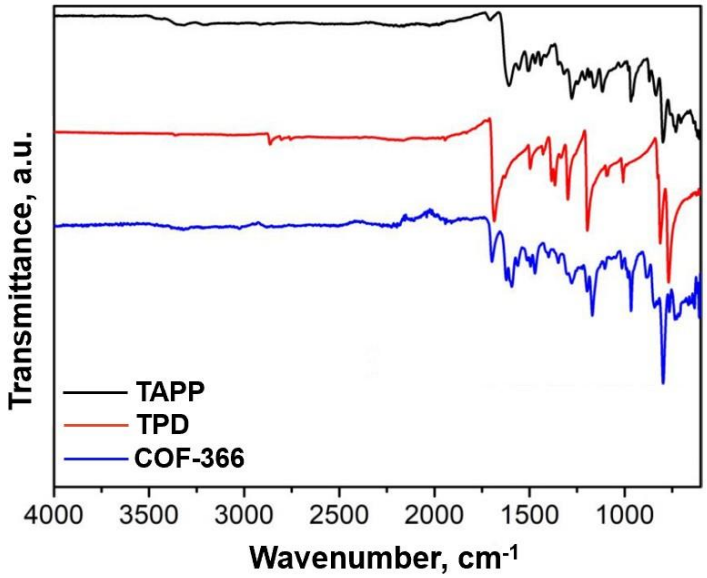

Figure 4.3. FTIR spectra of COF-366 as well as precursor TAPP and TPD.

After metalation, the M-COF366/CNT catalysts were obtained. Metal loading determined by ICP-AES is 1.9, 1.02, 1.70 and 1.47 wt% for Fe, Co, Ni and Cu, respectively, which are comparable. The TEM and XPS spectra of various M-COF366/CNT catalysts were collected. Fig. 4.4 shows the BF-HRTEM images and EDX elemental mapping results obtained under the STEM mode of the M-COF366/CNT catalysts. All catalysts exhibit an amorphous surface layer of ~4~5 nm

around the CNT core (marked by the red dashed boxes), which exhibits well-defined lattice fringes. EDX elemental mapping results show a uniform distribution of C, N, and metal elements.

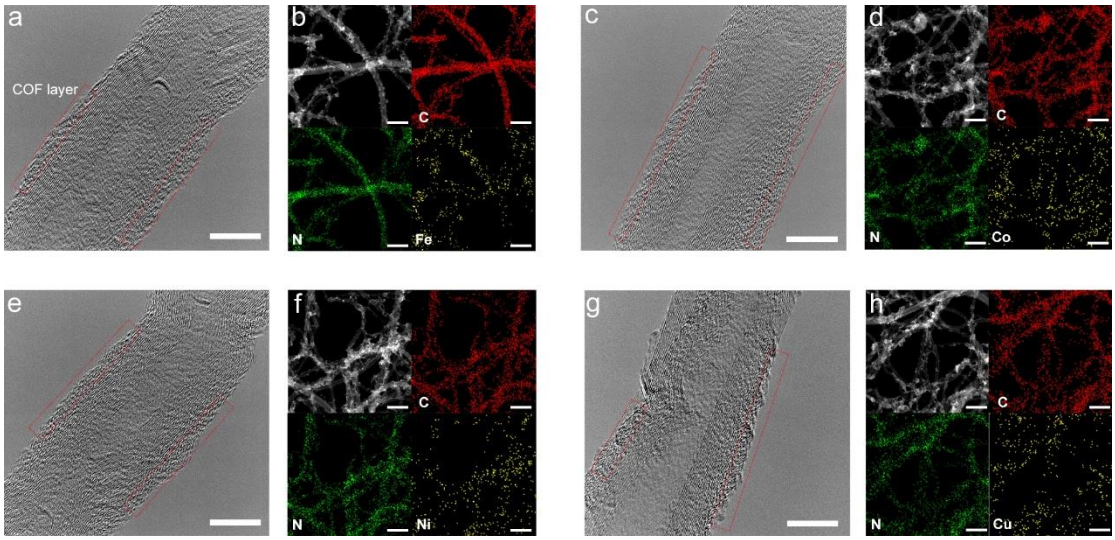

Figure 4.4. BF-TEM image and corresponding DF-STEM EDX elemental mapping result of various M-COF366/CNT catalysts. (a)-(b), Fe-COF366/CNT; (c)-(d), Co-COF366/CNT; (e)-(f), Ni-COF366/CNT; (g)-(h), Cu-COF366/CNT. The scale bar in (a), (c), (e), and (g) is 10 nm; the scale bar in (b), (d), (f), and (h) is 50 nm.

The XPS spectra of the M-COF366/CNT catalysts are shown in Figure 4.5. Survey scans displayed in Figure 4.5a show a strong C 1*s* peak. Compared to the survey can spectrum of the pristine CNT (Fig.4.5d), all catalysts show an N 1*s* peak at ~400 eV. Various metal 2*p* features also emerge in the corresponding catalysts. The high-resolution C 1*s* and N 1*s* spectra of these catalysts are shown in Figure 4.5b and 4.5c, respectively, and identical lineshapes can be found. Fig. 4.5d shows the high-resolution spectra of the M 2*p* features.

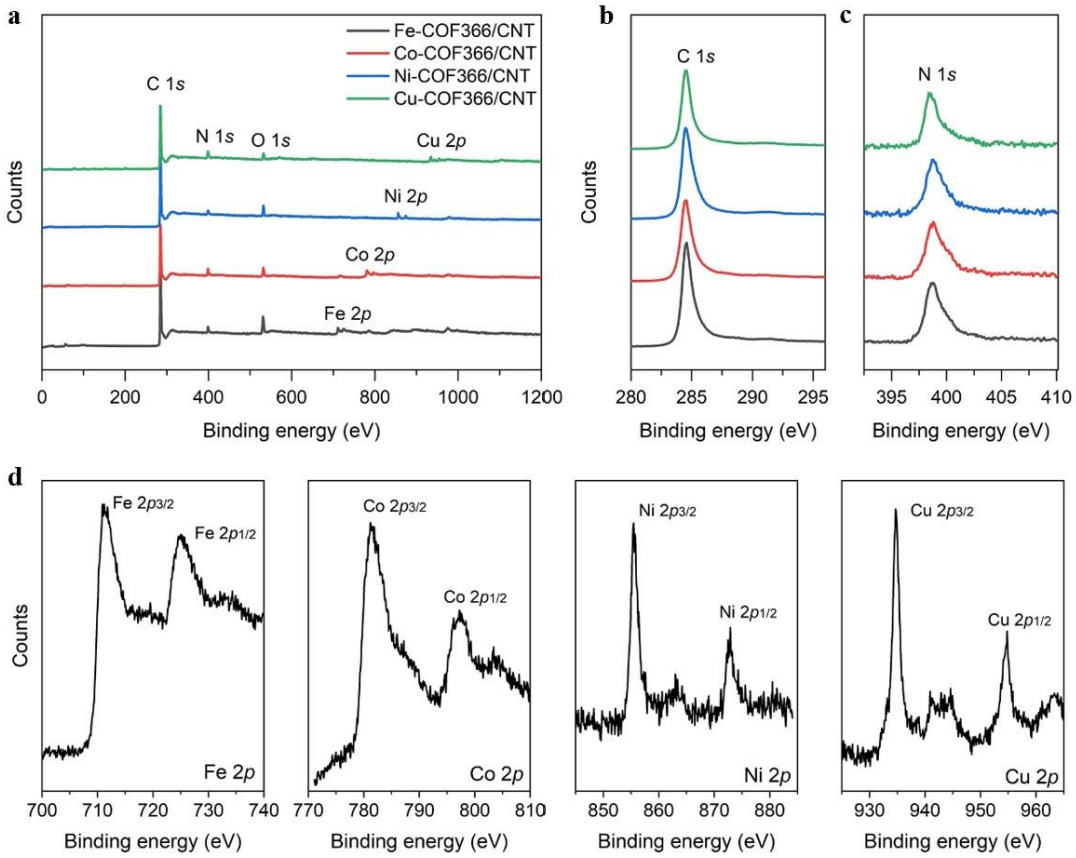

Figure 4.5. XPS spectra of different M-COF366/CNT catalysts. (a), Survey scan, and high-resolution scan of (b), C 1*s*, (c), N 1*s*, and (d), different M 2*p* features.

4.3.3 Electrocatalytic Properties of M-COF366/CNT

The electrocatalytic performance of M-COF366/CNT has been tested by RRDE in an O_2-saturated 0.1 M KOH (pH = 12.6) and 0.1 M $HClO_4$ (pH = 1.3) electrolytes by drop casting the catalyst ink onto a pre-polished glassy carbon disk electrode.

The effect of catalyst mass loading was first investigated using the Ni-COF366/CNT catalyst. The RRDE LSV curves were collected at mass loadings of 0.025, 0.05, 0.1, and 0.2 mg cm^{-2} to determine the optimal catalyst loading for maximum disk and ring currents (Figure 4.6). The experimental results showed that the catalyst ink does not

completely cover the surface of the electrode at a catalyst mass loading of 0.025 mg cm^{-2}. On the other hand, a mass loading of 0.05 mg cm^{-2} exhibited the highest disk and ring currents compared to the other tested mass loadings. Therefore, a mass loading of 0.05 mg cm^{-2} was chosen as the optimal loading for evaluating all catalysts.

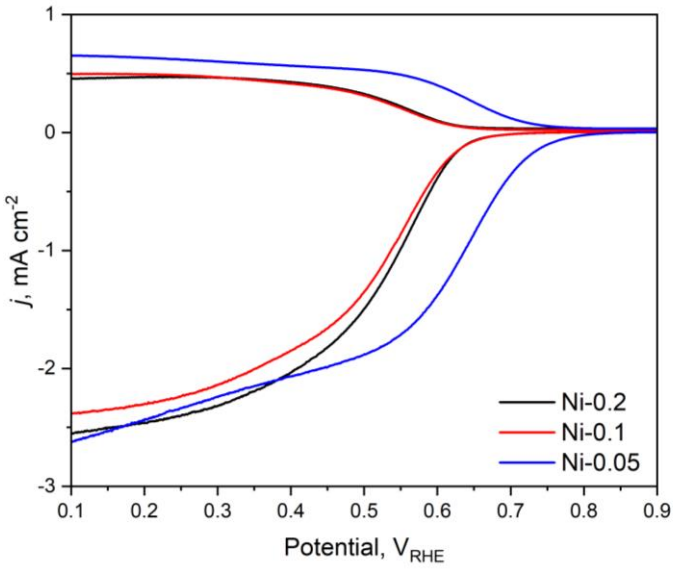

Figure 4.6. RRDE LSV curves collected for Ni-COF366/CNT mass loadings of 0.025, 0.05, 0.1 and 0.2 mg cm^{-2}, respectively, in O_2-saturated 0.1 M KOH electrolyte.

The ORR performance of M-COF366/CNT catalysts were collected in acidic and alkaline electrolytes, and the results are presented in Figures 4.7. It can be found that the overall ORR activity trend in the acidic 0.1 M $HClO_4$ electrolyte is that Co > Ni > Fe > Cu, as shown in Figure 4.7a. Their H_2O_2 preference, in terms of H_2O_2 faradaic efficiency (FE_{H2O2}) and molar selectivity (X_{H2O2}), were calculated and compared in Figure 4.7b. Co-COF366/CNT and Ni-COF366/CNT catalysts both show good selectivity towards H_2O_2 formation, affording an FE_{H2O2} >70% (corresponding to a

X_{H2O2}>80%) in a wide potential range. In contrast, Fe-COF366/CNT catalyst is preferential for 4e $^-$ORR pathway, showing an FE_{H2O2} <20%. The Tafel plots of these catalysts were also developed based on their kinetic ORR current density. As shown in Figure 4.7c, Fe-COF366/CNT exhibits the smallest Tafel slope of 104 mV dec^{-1}, showing superior kinetic performance over other catalysts. The value of this Tafel slope suggests an electron transfer or a proton-electron coupled transfer step as the rate determining step (RDS). Other catalysts show a much larger Tafel slope over 150 mV dec^{-1}, showing much slower kinetic performance that maybe caused by the initial O_2 adsorption.

The ORR performance in alkaline electrolyte is also collected and compared in Figure 4.7d-f. The performance trend has changed slightly that Fe-COF366/CNT becomes the best ORR catalyst, followed by Co, Ni and Cu. However, the ORR pathway preference of these catalyst doesn't change. Their FE_{H2O2} all dropped slightly. Additionally, all catalysts show much improved kinetic performance, evidently from their reduced Tafel slope values, as shown in Figure 4.7f. These experimental results are in good agreement to a new theoretical model being developed with a collaborator.

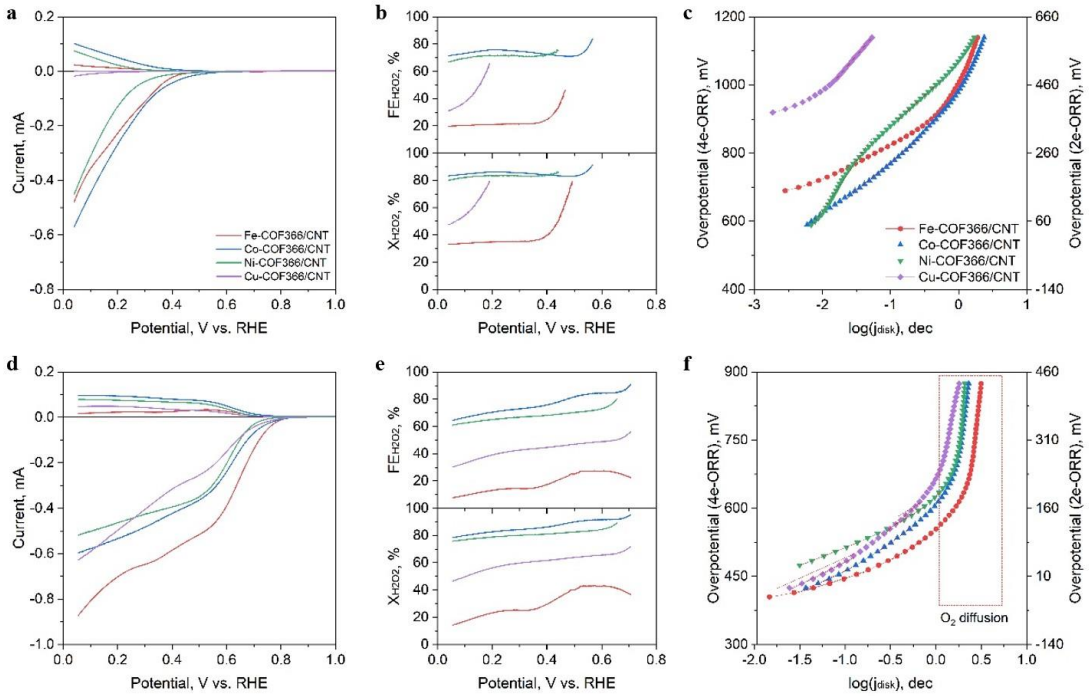

Figure 4.7. Electrochemical performance testing of the M-COF366/CNT catalysts. (a), RRDE LSV curves, (b), H_2O_2 Faradiac efficiency and molar selectivity, and (c), Tafel plots obtained in an acidic O_2-saturated 0.1 M $HClO_4$ electrolyte. (d)-(f), Performance collected in an alkaline O_2-saturated 0.1 M KOH electrolyte.

4.4 Conclusions

In summary, I presented a series of M-N-C SACs based on coaxial one-dimensional van der Waals heterostructures of COF and CNT. The M-COF366/CNT catalysts exhibited distinct catalytic activities tested in electrolytes with different pH values. Fe-COF366/CNT demonstrated the highest activity in alkaline electrolyte, while Co-COF366/CNT had the excellent activity in acidic and neutral electrolytes. Simultaneously, the influence of pH on the catalytic performance varied depending on the metal. In comparison to alkaline electrolyte, Cu-COF366/CNT showed almost no

catalytic activity in acidic electrolyte, whereas Co-COF366/CNT maintained high catalytic activity in alkaline, neutral, and acidic electrolytes. These findings provided a new strategy for the synthesis and design of M-N-C SACs. The incorporation of COFs and CNTs as a doping structure replaced traditional substrates and offered a more stable platform with increased exposure of active sites. Furthermore, the ORR activity of M-N-C SACs was further investigated as influenced by the pH of the electrolyte. This provided insights for the development of highly active electrocatalysts with excellent ORR performance and has potential applications in various fields.

Chapter V. Conclusions and Outlooks

5.1 Conclusions

COFs, a new type of porous polymer, have demonstrated their potential for use in electrochemical devices. In my first research, I designed and synthesized a composite comprising a pyrazine-based COF and conductive graphene as an electrode material for supercapacitors. And the performance of the composite was evaluated in an electrolyte containing ammonium ions. According to previous studies, the COF containing phenazine redox active groups exhibited excellent specific capacitance and cycle life. Supercapacitors assembled solely with this COF as the electrode material also demonstrated high energy density and power density. However, the internal stacking of COF layers hinders the exposure of redox-active sites, thus affecting its performance. In the meantime, the reversible decomposition of phenazine groups leads to the unsatisfactory stability of the COF. Therefore, I aimed to modify the high-performance pyrazine-based COF by designing a composite electrode doped with graphene. The objectives of my design were as follows: (1) graphene as a physical spacer can effectively mitigates the interlayer van der Waals forces of COF; (2) graphene with high electrical conductivity can provide additional charge carriers and thus enhance the conductivity of the composite electrode; (3) the ammonium ions in the electrolyte can form unique hydrogen bonds with phenazine nitrogen, imparting higher stability to the composite electrode. However, the synthesized phenazine-based COF did not exhibit satisfactory electrochemical performance. The possible reason for this was the poor stability of this COF led to the reversible reaction of phenazine groups after more than

three charge/discharge cycles, resulting in the loss of electrode activity. Consequently, this research had to be terminated. To gain deeper insights into the application and prospects of COFs in supercapacitors, I conducted an extensive literature review, which provides a comprehensive analysis of the progress, challenges, and future directions in utilizing COFs for supercapacitor electrodes.

In my second project, I investigated the catalytic effect of COFs as substrates for M-N-C SACs and their ORR catalytic performance in electrolytes of different pH values. I synthesized a composite of COFs containing porphyrin macrocycles with carbon nanotubes and introduced a range of transition metals (Fe, Co, Ni, Cu). The porphyrin units enabled the formation of M-N_4 coordination structures, which could effectively anchor the metal and has high atomic utilization. In the meantime, COFs provided well-defined and designable catalytic active sites, while their large surface area facilitated enhanced contact with reactants. As a result, M-N-C SACs exhibited outstanding catalytic activity comparable to precious metal catalysts.

To prevent COF stacking and improve its electric conductivity, CNTs were introduced as spacers and conductive substrate, facilitating intermolecular charge transfer between COF and CNT and further enhancing the catalytic activity of the composite catalyst. To investigate the ORR catalytic mechanisms of the catalysts and develop more efficient catalysts, I conducted tests in electrolytes of acidic and alkaline with different pH, evaluating the influence on catalyst activity and the dependence of different metal atoms. Performance tests revealed that the catalyst containing iron atoms exhibited the highest ORR activity in O_2-saturated 0.1 M KOH (pH = 12.6),

while the catalyst containing manganese atoms showed the poorest performance. However, in O_2-saturated 0.1 M KOH (pH = 12.6) electrolytes, Co-COF366/CNT demonstrated excellent performance. Thus, the results of the performance tests indicate a significant influence of pH on the ORR activity of the catalysts, with lower pH values corresponding to lower catalytic activity. Furthermore, different metals exhibited varying pH dependencies, such as the cobalt-containing catalyst showing ORR performance in both acidic and alkaline electrolytes, while the copper-containing catalyst exhibited almost no activity in low pH electrolytes. The good correlation between my experimental results and a theoretical model being developed by a collaborator could shade new lights on the rational catalyst design.

5.2 Outlooks

Although COFs have found widespread use in the field of electrochemistry, several challenges need to be addressed to fully exploit their potential. In terms of COF performance, the first challenge is to develop COFs with higher crystallinity. This can be achieved by designing conjugated structures and stacking motifs for the synthesis modules of COFs. The second challenge involves improving the periodicity of COFs, which can be accomplished by controlling reaction conditions to promote the formation of weak chemical bonds, such as intermolecular hydrogen bonds or π-π interactions. Thirdly, to enhance the application of COFs as electrode materials in energy storage and electrocatalysis, their conductivity can be improved by doping them with highly conductive materials to form composite materials. Fourthly, the reusability of COFs can

be enhanced by designing fully conjugated structures or incorporating olefinic linkages. Fifthly, their processability necessitates requires clarification of each step in the synthesis as well as the precise control of structure and arrangement of COF modules.

In terms of the synthesis of COFs, a combination of existing synthetic methods, such as solvent-thermal synthesis, microwave synthesis, and mechanochemical synthesis, can be employed or upgraded to improve COF synthesis efficiency. On the other hand, to cater to the requirements of flexible devices, COFs can be processed into thin film electrodes via solution casting methods.[217] Additionally, for industrial-scale production, rapid and large scale synthesis of COFs can be achieved through flow reactor methods[218] or salt mediated crystallization[38] techniques. Regarding characterization techniques, the development of more accurate and precise instruments is crucial for determining the detailed structure of COFs. The integration of theoretical models and computational approaches is also essential for analyzing and predicting COF stacking arrangements and topological structures.

In terms of energy storage applications, the specific capacitance of COFs firstly needs to be increased by introducing more stable and highly reactive redox active groups. Additionally, controlling the growth mode of COFs, such as transitioning from parallel growth with the substrate to vertical growth, can effectively enhance their performance. In terms of catalytic applications, it is essential to improve the hydrolytic stability of COFs and their durability in extreme environments, such as strong acid or alkaline electrolytes. Furthermore, the solubility can be enhanced and the synthesis process can be facilitated by controlling the morphology of COFs, such as transforming

them from insoluble powders to soluble films or tubular structures. These advancements in COFs' properties and synthesis strategies will contribute to their widespread use in areas such as energy storage and catalysis applications.

Reference

[1] a)A. Thomas, *Angewandte Chemie International Edition* **2010**, 49, 8328; b)J. D. Wuest, *Chemical communications* **2005**, 5830; c)T. F. De Greef, M. M. Smulders, M. Wolffs, A. P. Schenning, R. P. Sijbesma, E. Meijer, *Chemical Reviews* **2009**, 109, 5687; d)L. C. Palmer, S. I. Stupp, *Accounts of chemical research* **2008**, 41, 1674.

[2] a)G. M. Whitesides, E. E. Simanek, J. P. Mathias, C. T. Seto, D. Chin, M. Mammen, D. M. Gordon, *Accounts of Chemical Research* **1995**, 28, 37; b)S. J. Rowan, S. J. Cantrill, G. R. Cousins, J. K. Sanders, J. F. Stoddart, *Angewandte Chemie International Edition* **2002**, 41, 898; c)L. Zang, Y. Che, J. S. Moore, *Accounts of chemical research* **2008**, 41, 1596; d)A. I. Cooper, *Advanced Materials* **2009**, 21, 1291; e)M.-L. Tong, X.-M. Chen, X.-L. Yu, T. C. Mak, *Journal of the Chemical Society, Dalton Transactions* **1998**, 5.

[3] a)L. Lin, A. Argon, *Journal of Materials Science* **1994**, 29, 294; b)J. R. Wünsch, **2000**; c)J. X. Jiang, F. Su, A. Trewin, C. D. Wood, N. L. Campbell, H. Niu, C. Dickinson, A. Y. Ganin, M. J. Rosseinsky, Y. Z. Khimyak, *Angewandte Chemie International Edition* **2007**, 46, 8574; d)P. M. Budd, B. S. Ghanem, S. Makhseed, N. B. McKeown, K. J. Msayib, C. E. Tattershall, *Chemical communications* **2004**, 230.

[4] A. P. Cote, A. I. Benin, N. W. Ockwig, M. O'Keeffe, A. J. Matzger, O. M. Yaghi, *science* **2005**, 310, 1166.

[5] H. M. El-Kaderi, J. R. Hunt, J. L. Mendoza-Cortés, A. P. Côté, R. E. Taylor, M. O'Keeffe, O. M. Yaghi, *Science* **2007**, 316, 268.

[6] a)S. Kandambeth, D. B. Shinde, M. K. Panda, B. Lukose, T. Heine, R. Banerjee, *Angewandte Chemie* **2013**, 125, 13290; b)B. P. Biswal, H. D. Chaudhari, R. Banerjee, U. K. Kharul, *Chemistry–A European Journal* **2016**, 22, 4695.

[7] a)X.-D. Li, H.-P. Zang, J.-T. Wang, J.-F. Wang, H. Zhang, *Journal of Materials Chemistry A* **2014**, 2, 18554; b)M. G. Rabbani, A. K. Sekizkardes, Z. Kahveci, T. E. Reich, R. Ding, H. M. El-Kaderi, *Chemistry–A European Journal* **2013**, 19, 3324.

[8] a)M. Bhadra, H. S. Sasmal, A. Basu, S. P. Midya, S. Kandambeth, P. Pachfule, E. Balaraman, R. Banerjee, *ACS Applied Materials & Interfaces* **2017**, 9, 13785; b)D. B. Shinde, S. Kandambeth, P. Pachfule, R. R. Kumar, R. Banerjee, *Chemical Communications* **2015**, 51, 310.

[9] a)S. Wan, J. Guo, J. Kim, H. Ihee, D. Jiang, *Angewandte Chemie* **2008**, 120, 8958; b)X. Ding, J. Guo, X. Feng, Y. Honsho, J. Guo, S. Seki, P. Maitarad, A. Saeki, S. Nagase, D. Jiang, *Angewandte Chemie International Edition* **2011**, 50, 1289.

[10] a)X. Ding, L. Chen, Y. Honsho, X. Feng, O. Saengsawang, J. Guo, A. Saeki, S. Seki, S. Irle, S. Nagase, *Journal of the American Chemical Society* **2011**, 133, 14510; b)X. Feng, L. Liu, Y. Honsho, A. Saeki, S. Seki, S. Irle, Y. Dong, A. Nagai, D. Jiang, *Angewandte Chemie* **2012**, 124, 2672.

[11] a)S. Mitra, H. S. Sasmal, T. Kundu, S. Kandambeth, K. Illath, D. Diaz Diaz, R. Banerjee, *Journal of the American Chemical Society* **2017**, 139, 4513; b)Q. Fang, J. Wang, S. Gu, R. B. Kaspar, Z. Zhuang, J. Zheng, H. Guo, S. Qiu, Y. Yan, *Journal of the American chemical society* **2015**, 137, 8352.

[12] a)T. Zhang, C. Gao, W. Huang, Y. Chen, Y. Wang, J. Wang, *Talanta* **2018**, 188, 578; b)S. Dalapati, S. Jin, J. Gao, Y. Xu, A. Nagai, D. Jiang, *Journal of the American Chemical Society* **2013**, 135, 17310.

[13] a)R. Sun, S. Hou, C. Luo, X. Ji, L. Wang, L. Mai, C. Wang, *Nano Letters* **2020**, 20, 3880; b)S. Haldar, R. Kushwaha, R. Maity, R. Vaidhyanathan, *ACS Materials Letters* **2019**, 1, 490.

[14] J. Yan, Q. Wang, T. Wei, Z. Fan, *Advanced Energy Materials* **2014**, 4, 1300816.

[15] T. Wilberforce, A. Alaswad, A. Palumbo, M. Dassisti, A.-G. Olabi, *International journal of*

hydrogen energy **2016**, 41, 16509.
[16] M. S. Lohse, T. Bein, *Advanced Functional Materials* **2018**, 28, 1705553.
[17] B. J. Smith, W. R. Dichtel, *Journal of the American Chemical Society* **2014**, 136, 8783.
[18] J. W. Colson, A. R. Woll, A. Mukherjee, M. P. Levendorf, E. L. Spitler, V. B. Shields, M. G. Spencer, J. Park, W. R. Dichtel, *Science* **2011**, 332, 228.
[19] W. Huang, Y. Jiang, X. Li, X. Li, J. Wang, Q. Wu, X. Liu, *ACS Applied Materials & Interfaces* **2013**, 5, 8845.
[20] S. B. Kalidindi, C. Wiktor, A. Ramakrishnan, J. Weßing, A. Schneemann, G. Van Tendeloo, R. A. Fischer, *Chemical Communications* **2013**, 49, 463.
[21] X. Guan, Y. Ma, H. Li, Y. Yusran, M. Xue, Q. Fang, Y. Yan, V. Valtchev, S. Qiu, *Journal of the American Chemical Society* **2018**, 140, 4494.
[22] P. Kuhn, M. Antonietti, A. Thomas, *Angewandte Chemie International Edition* **2008**, 47, 3450.
[23] M. J. Bojdys, J. Jeromenok, A. Thomas, M. Antonietti, *Advanced materials* **2010**, 22, 2202.
[24] J. Maschita, T. Banerjee, G. Savasci, F. Haase, C. Ochsenfeld, B. V. Lotsch, *Angewandte Chemie International Edition* **2020**, 59, 15750.
[25] B. Baumgartner, M. J. Bojdys, M. M. Unterlass, *Polymer Chemistry* **2014**, 5, 3771.
[26] Q. Fang, Z. Zhuang, S. Gu, R. B. Kaspar, J. Zheng, J. Wang, S. Qiu, Y. Yan, *Nature communications* **2014**, 5, 4503.
[27] A. Kumar, Y. Kuang, Z. Liang, X. Sun, *Materials Today Nano* **2020**, 11, 100076.
[28] S. Nain, R. Singh, S. Ravichandran, *Advanced Journal of Chemistry-Section A* **2019**, 2, 94.
[29] N. L. Campbell, R. Clowes, L. K. Ritchie, A. I. Cooper, *Chemistry of Materials* **2009**, 21, 204.
[30] H. Wei, S. Chai, N. Hu, Z. Yang, L. Wei, L. Wang, *Chemical Communications* **2015**, 51, 12178.
[31] J. Xie, S. A. Shevlin, Q. Ruan, S. J. Moniz, Y. Liu, X. Liu, Y. Li, C. C. Lau, Z. X. Guo, J. Tang, *Energy & Environmental Science* **2018**, 11, 1617.
[32] K. S. Suslick, D. A. Hammerton, R. E. Cline, *Journal of the American Chemical Society* **1986**, 108, 5641.
[33] W.-J. Son, J. Kim, J. Kim, W.-S. Ahn, *Chemical Communications* **2008**, 6336.
[34] S.-T. Yang, J. Kim, H.-Y. Cho, S. Kim, W.-S. Ahn, *RSC advances* **2012**, 2, 10179.
[35] W. Zhao, P. Yan, H. Yang, M. Bahri, A. M. James, H. Chen, L. Liu, B. Li, Z. Pang, R. Clowes, *Nature Synthesis* **2022**, 1, 87.
[36] B. P. Biswal, S. Chandra, S. Kandambeth, B. Lukose, T. Heine, R. Banerjee, *Journal of the American Chemical Society* **2013**, 135, 5328.
[37] G. Das, D. B. Shinde, S. Kandambeth, B. P. Biswal, R. Banerjee, *Chemical Communications* **2014**, 50, 12615.
[38] S. Karak, S. Kandambeth, B. P. Biswal, H. S. Sasmal, S. Kumar, P. Pachfule, R. Banerjee, *Journal of the American Chemical Society* **2017**, 139, 1856.
[39] Y. Jiang, W. Huang, J. Wang, Q. Wu, H. Wang, L. Pan, X. Liu, *Journal of Materials Chemistry A* **2014**, 2, 8201.
[40] J. Wang, J. Tang, B. Ding, V. Malgras, Z. Chang, X. Hao, Y. Wang, H. Dou, X. Zhang, Y. Yamauchi, *Nature communications* **2017**, 8, 15717.
[41] F. J. Uribe-Romo, J. R. Hunt, H. Furukawa, C. Klock, M. O'Keeffe, O. M. Yaghi, *Journal of the American Chemical Society* **2009**, 131, 4570.
[42] F. J. Uribe-Romo, C. J. Doonan, H. Furukawa, K. Oisaki, O. M. Yaghi, *Journal of the American Chemical Society* **2011**, 133, 11478.

[43] N. Huang, X. Chen, R. Krishna, D. Jiang, *Angewandte Chemie International Edition* **2015**, 54, 2986.
[44] X. Zhao, P. Pachfule, S. Li, T. Langenhahn, M. Ye, C. Schlesiger, S. Praetz, J. Schmidt, A. Thomas, *Journal of the American Chemical Society* **2019**, 141, 6623.
[45] J. Guo, Y. Xu, S. Jin, L. Chen, T. Kaji, Y. Honsho, M. A. Addicoat, J. Kim, A. Saeki, H. Ihee, *Nature communications* **2013**, 4, 2736.
[46] Z. Meng, R. M. Stolz, K. A. Mirica, *Journal of the American Chemical Society* **2019**, 141, 11929.
[47] H. Li, J. Chang, S. Li, X. Guan, D. Li, C. Li, L. Tang, M. Xue, Y. Yan, V. Valtchev, *Journal of the American Chemical Society* **2019**, 141, 13324.
[48] J. I. Feldblyum, C. H. McCreery, S. C. Andrews, T. Kurosawa, E. J. Santos, V. Duong, L. Fang, A. L. Ayzner, Z. Bao, *Chemical Communications* **2015**, 51, 13894.
[49] C. R. Mulzer, L. Shen, R. P. Bisbey, J. R. McKone, N. Zhang, H. c. D. Abruña, W. R. Dichtel, *ACS central science* **2016**, 2, 667.
[50] J. Guo, C. Y. Lin, Z. Xia, Z. Xiang, *Angewandte Chemie International Edition* **2018**, 57, 12567.
[51] F. Haase, B. V. Lotsch, *Chemical Society Reviews* **2020**, 49, 8469.
[52] B. Lukose, A. Kuc, T. Heine, *Chemistry–A European Journal* **2011**, 17, 2388.
[53] W. Zhou, H. Wu, T. Yildirim, *Chemical Physics Letters* **2010**, 499, 103.
[54] H. Xu, J. Gao, D. Jiang, *Nature chemistry* **2015**, 7, 905.
[55] X. Chen, M. Addicoat, E. Jin, L. Zhai, H. Xu, N. Huang, Z. Guo, L. Liu, S. Irle, D. Jiang, *Journal of the American chemical society* **2015**, 137, 3241.
[56] G. Das, B. P. Biswal, S. Kandambeth, V. Venkatesh, G. Kaur, M. Addicoat, T. Heine, S. Verma, R. Banerjee, *Chemical science* **2015**, 6, 3931.
[57] M. Matsumoto, R. R. Dasari, W. Ji, C. H. Feriante, T. C. Parker, S. R. Marder, W. R. Dichtel, *Journal of the American Chemical Society* **2017**, 139, 4999.
[58] S. Karak, S. Kumar, P. Pachfule, R. Banerjee, *Journal of the American Chemical Society* **2018**, 140, 5138.
[59] E. L. Spitler, M. R. Giovino, S. L. White, W. R. Dichtel, *Chemical Science* **2011**, 2, 1588.
[60] C. R. DeBlase, K. E. Silberstein, T.-T. Truong, H. D. Abruña, W. R. Dichtel, *Journal of the American Chemical Society* **2013**, 135, 16821.
[61] S. Lin, C. S. Diercks, Y.-B. Zhang, N. Kornienko, E. M. Nichols, Y. Zhao, A. R. Paris, D. Kim, P. Yang, O. M. Yaghi, *Science* **2015**, 349, 1208.
[62] S. Kandambeth, A. Mallick, B. Lukose, M. V. Mane, T. Heine, R. Banerjee, *Journal of the American Chemical Society* **2012**, 134, 19524.
[63] F. Haase, E. Troschke, G. Savasci, T. Banerjee, V. Duppel, S. Dörfler, M. M. Grundei, A. M. Burow, C. Ochsenfeld, S. Kaskel, *Nature communications* **2018**, 9, 2600.
[64] P. J. Waller, S. J. Lyle, T. M. Osborn Popp, C. S. Diercks, J. A. Reimer, O. M. Yaghi, *Journal of the American Chemical Society* **2016**, 138, 15519.
[65] X. Li, C. Zhang, S. Cai, X. Lei, V. Altoe, F. Hong, J. J. Urban, J. Ciston, E. M. Chan, Y. Liu, *Nature communications* **2018**, 9, 2998.
[66] Y. Yan, T. He, B. Zhao, K. Qi, H. Liu, B. Y. Xia, *Journal of Materials Chemistry A* **2018**, 6, 15905.
[67] a)J. Gu, Y. Peng, T. Zhou, J. Ma, H. Pang, Y. Yamauchi, *Nano Research Energy* **2022**, 1, e9120009; b)Y. Bai, Y. Liu, M. Liu, X. Wang, S. Shang, W. Gao, C. Du, Y. Qiao, J. Chen, J. Dong, *Angewandte Chemie* **2022**, 134, e202113067; c)Y. Peng, G. Xu, Z. Hu, Y. Cheng, C. Chi, D. Yuan, H. Cheng, D. Zhao, *ACS applied materials & interfaces* **2016**, 8, 18505.
[68] C. C. McCrory, S. Jung, J. C. Peters, T. F. Jaramillo, *Journal of the American Chemical Society*

2013, 135, 16977.
[69] Y. Ma, Y. Fu, W. Jiang, Y. Wu, C. Liu, G. Che, Q. Fang, *Journal of Materials Chemistry A* **2022**, 10, 10092.
[70] S. Mondal, B. Mohanty, M. Nurhuda, S. Dalapati, R. Jana, M. Addicoat, A. Datta, B. K. Jena, A. Bhaumik, *ACS Catalysis* **2020**, 10, 5623.
[71] Z. Liang, H.-Y. Wang, H. Zheng, W. Zhang, R. Cao, *Chemical Society Reviews* **2021**, 50, 2540.
[72] Y. Wu, J. M. Veleta, D. Tang, A. D. Price, C. E. Botez, D. Villagrán, *Dalton Transactions* **2018**, 47, 8801.
[73] Y. Liu, Y. Han, Z. Zhang, W. Zhang, W. Lai, Y. Wang, R. Cao, *Chemical science* **2019**, 10, 2613.
[74] F. Zhao, J. Zhang, D. WÖhrle, M. Kaneko, *Journal of Porphyrins and Phthalocyanines* **2000**, 4, 31.
[75] A. Koca, *Electrochemistry communications* **2009**, 11, 838.
[76] H. B. Aiyappa, J. Thote, D. B. Shinde, R. Banerjee, S. Kurungot, *Chemistry of Materials* **2016**, 28, 4375.
[77] S. Wu, M. Li, H. Phan, D. Wang, T. S. Herng, J. Ding, Z. Lu, J. Wu, *Angewandte Chemie International Edition* **2018**, 57, 8007.
[78] L. Xie, X. P. Zhang, B. Zhao, P. Li, J. Qi, X. Guo, B. Wang, H. Lei, W. Zhang, U. P. Apfel, *Angewandte Chemie* **2021**, 133, 7654.
[79] Y. Yamada, Y. Fukunishi, S.-i. Yamazaki, S. Fukuzumi, *Chemical communications* **2010**, 46, 7334.
[80] S. Sun, N. Jiang, D. Xia, *The Journal of Physical Chemistry C* **2011**, 115, 9511.
[81] J. P. Collman, M. Kaplun, R. A. Decréau, *Dalton Transactions* **2006**, 554.
[82] a)M. Wang, H. Guo, R. Xue, Q. Li, H. Liu, N. Wu, W. Yao, W. Yang, *ChemElectroChem* **2019**, 6, 2984; b)T. Sun, J. Xie, W. Guo, D. S. Li, Q. Zhang, *Advanced Energy Materials* **2020**, 10, 1904199.
[83] M. S. Halper, J. C. Ellenbogen, *The MITRE Corporation, McLean, Virginia, USA* **2006**, 1.
[84] L. Qie, W. Chen, H. Xu, X. Xiong, Y. Jiang, F. Zou, X. Hu, Y. Xin, Z. Zhang, Y. Huang, *Energy & Environmental Science* **2013**, 6, 2497.
[85] I. E. Rauda, V. Augustyn, B. Dunn, S. H. Tolbert, *Accounts of chemical research* **2013**, 46, 1113.
[86] P. Bhanja, S. K. Das, K. Bhunia, D. Pradhan, T. Hayashi, Y. Hijikata, S. Irle, A. Bhaumik, *ACS Sustainable Chemistry & Engineering* **2018**, 6, 202.
[87] A. F. El-Mahdy, Y. H. Hung, T. H. Mansoure, H. H. Yu, T. Chen, S. W. Kuo, *Chemistry–An Asian Journal* **2019**, 14, 1429.
[88] C. R. DeBlase, K. Hernández-Burgos, K. E. Silberstein, G. G. Rodríguez-Calero, R. P. Bisbey, H. D. Abruña, W. R. Dichtel, *ACS nano* **2015**, 9, 3178.
[89] P. Wang, Q. Wu, L. Han, S. Wang, S. Fang, Z. Zhang, S. Sun, *Rsc advances* **2015**, 5, 27290.
[90] F. Xu, S. Jin, H. Zhong, D. Wu, X. Yang, X. Chen, H. Wei, R. Fu, D. Jiang, *Scientific Reports* **2015**, 5, 8225.
[91] T. Sun, Z.-J. Li, X. Yang, S. Wang, Y.-H. Zhu, X.-B. Zhang, *CCS Chemistry* **2019**, 1, 365.
[92] H. Yang, S. Zhang, L. Han, Z. Zhang, Z. Xue, J. Gao, Y. Li, C. Huang, Y. Yi, H. Liu, *ACS applied materials & interfaces* **2016**, 8, 5366.
[93] X. Chen, W. Sun, Y. Wang, *ChemElectroChem* **2020**, 7, 3905.
[94] J. Yoo, S.-J. Cho, G. Y. Jung, S. H. Kim, K.-H. Choi, J.-H. Kim, C. K. Lee, S. K. Kwak, S.-Y. Lee, *Nano letters* **2016**, 16, 3292.
[95] S. N. Talapaneni, T. H. Hwang, S. H. Je, O. Buyukcakir, J. W. Choi, A. Coskun, *Angewandte Chemie International Edition* **2016**, 55, 3106.
[96] Z. Wang, W. Jin, X. Huang, G. Lu, Y. Li, *The Chemical Record* **2020**, 20, 1198.

[97] B. C. Patra, S. K. Das, A. Ghosh, P. Moitra, M. Addicoat, S. Mitra, A. Bhaumik, S. Bhattacharya, A. Pradhan, *Journal of Materials Chemistry A* **2018**, 6, 16655.
[98] R. Kötz, M. Carlen, *Electrochimica acta* **2000**, 45, 2483.
[99] J. Libich, J. Máca, J. Vondrák, O. Čech, M. Sedlaříková, *Journal of Energy Storage* **2018**, 17, 224.
[100] P. Simon, Y. Gogotsi, *Nature materials* **2008**, 7, 845.
[101] a)T. Li, X. Yan, Y. Liu, W.-D. Zhang, Q.-T. Fu, H. Zhu, Z. Li, Z.-G. Gu, *Polymer Chemistry* **2020**, 11, 47; b)Z. Meng, A. Aykanat, K. A. Mirica, *Chemistry of Materials* **2018**, 31, 819; c)J.-M. Seo, H.-J. Noh, H. Y. Jeong, J.-B. Baek, *Journal of the American Chemical Society* **2019**, 141, 11786.
[102] X. Li, H. Wang, H. Chen, Q. Zheng, Q. Zhang, H. Mao, Y. Liu, S. Cai, B. Sun, C. Dun, *Chem* **2020**, 6, 933.
[103] K. Gotoh, T. Asaji, H. Ishida, *Acta Crystallographica Section C: Crystal Structure Communications* **2007**, 63, o17.
[104] S. Kandambeth, J. Jia, H. Wu, V. S. Kale, P. T. Parvatkar, J. Czaban-Jóźwiak, S. Zhou, X. Xu, Z. O. Ameur, E. Abou-Hamad, *Advanced Energy Materials* **2020**, 10, 2001673.
[105] Y. Kou, Y. Xu, Z. Guo, D. Jiang, *Angewandte Chemie* **2011**, 123, 8912.
[106] H. Peng, J. Raya, F. Richard, W. Baaziz, O. Ersen, A. Ciesielski, P. Samorì, *Angewandte Chemie International Edition* **2020**, 59, 19602.
[107] Z. Tian, V. S. Kale, Y. Wang, S. Kandambeth, J. Czaban-Jozwiak, O. Shekhah, M. Eddaoudi, H. N. Alshareef, *Journal of the American Chemical Society* **2021**, 143, 19178.
[108] a)S. Chu, A. Majumdar, *Nature* **2012**, 488, 294; b)A. Q. Al-Shetwi, *Sci. Total Environ.* **2022**, 822, 153645.
[109] a)M. R. Chakraborty, S. Dawn, P. K. Saha, J. B. Basu, T. S. Ustun, *Batteries* **2022**, 8, 124; b)A. S. Arico, P. Bruce, B. Scrosati, J.-M. Tarascon, W. Van Schalkwijk, *Materials for sustainable energy: a collection of peer-reviewed research and review articles from Nature Publishing Group* **2011**, 148.
[110] a)P. Simon, Y. Gogotsi, B. Dunn, *Science* **2014**, 343, 1210; b)M. Lu, *Supercapacitors: materials, systems, and applications*, John Wiley & Sons, **2013**; c)Y. Zhang, H. Feng, X. Wu, L. Wang, A. Zhang, T. Xia, H. Dong, X. Li, L. Zhang, *Int J Hydrogen Energ* **2009**, 34, 4889; d)J. R. Miller, P. Simon, *science* **2008**, 321, 651; e)M. I. Ionescu, Y. Zhang, R. Li, H. Abou-Rachid, X. Sun, *Appl Surf Sci* **2012**, 258, 4563; f)G. Wang, L. Zhang, J. Zhang, *Chem. Soc. Rev.* **2012**, 41, 797; g)P. Simon, Y. Gogotsi, in *Nanoscience and technology: a collection of reviews from Nature journals*, World Scientific, 2010.
[111]H. v. Helmholtz, *Annalen der Physik* **1879**, 243, 337.
[112] F. Béguin;, V. Presser;, A. Balducci;, E. Frackowiak, *Adv. Mater.* **2014**, 26, 2219.
[113] H. Zhang, G. Cao, Y. Yang, *Energy Environ. Sci.* **2011**, 4, 932.
[114] Y. B. Tan, J.-M. Lee, *J Mater Chem A* **2013**, 1, 14814.
[115] B. E. Conway, V. Birss, J. Wojtowicz, *J Power Sources* **1997**, 66, 1.
[116] a)J. Kim, J. Lee, J. You, M.-S. Park, M. S. Al Hossain, Y. Yamauchi, J. H. Kim, *Mater Horizons* **2016**, 3, 517; b)G. Zhang, X. Xiao, B. Li, P. Gu, H. Xue, H. Pang, *J Mater Chem A* **2017**, 5, 8155.
[117] Y. Shao, M. F. El-Kady, J. Sun, Y. Li, Q. Zhang, M. Zhu, H. Wang, B. Dunn, R. B. Kaner, *Chem. Rev.* **2018**, 118, 9233.
[118] Y. Zhu, H. Cui, X. Meng, J. Zheng, P. Yang, L. Li, Z. Wang, S. Jia, Z. Zhu, *ACS Appl. Mater. Interfaces* **2016**, 8, 6481.
[119] S. Liu, Y. Cai, X. Zhao, Y. Liang, M. Zheng, H. Hu, H. Dong, S. Jiang, Y. Liu, Y. Xiao, *J Power Sources* **2017**, 360, 373.
[120] a)J. Yang, T. Lan, J. Liu, Y. Song, M. Wei, *Electrochim. Acta* **2013**, 105, 489; b)S. Chandra, D.

Roy Chowdhury, M. Addicoat, T. Heine, A. Paul, R. Banerjee, *Chem Mater* **2017**, 29, 2074.

[121] a)M. Inagaki, H. Konno, O. Tanaike, *J Power Sources* **2010**, 195, 7880; b)E. Frackowiak, *hys. Chem. Chem. Phys.* **2007**, 9, 1774.

[122] a)H. Furukawa, O. M. Yaghi, *J. Am. Chem. Soc.* **2009**, 131, 8875; b)Y. Zeng, R. Zou, Y. Zhao, *Adv. Mater.* **2016**, 28, 2855; c)N. Huang, X. Chen, R. Krishna, D. Jiang, *Angewandte Chemie* **2015**, 127, 3029; d)J.-T. Yu, Z. Chen, J. Sun, Z.-T. Huang, Q.-Y. Zheng, *J. Mater. Chem.* **2012**, 22, 5369; e)Y. Li, Q. Chen, T. Xu, Z. Xie, J. Liu, X. Yu, S. Ma, T. Qin, L. Chen, *J. Am. Chem. Soc.* **2019**, 141, 13822; f)W. K. Haug, E. M. Moscarello, E. R. Wolfson, P. L. McGrier, *Chem. Soc. Rev.* **2020**, 49, 839; g)Q. Fang, J. Wang, S. Gu, R. B. Kaspar, Z. Zhuang, J. Zheng, H. Guo, S. Qiu, Y. Yan, *J. Am. Chem. Soc.* **2015**, 137, 8352; h)Q. Guan, L. L. Zhou, W. Y. Li, Y. A. Li, Y. B. Dong, *Eur. J. Chem.* **2020**, 26, 5583; i)X. Liu, D. Huang, C. Lai, G. Zeng, L. Qin, H. Wang, H. Yi, B. Li, S. Liu, M. Zhang, *Chem. Soc. Rev.* **2019**, 48, 5266; j)S.-Y. Ding, M. Dong, Y.-W. Wang, Y.-T. Chen, H.-Z. Wang, C.-Y. Su, W. Wang, *J. Am. Chem. Soc.* **2016**, 138, 3031; k)S. Pakhira, K. P. Lucht, J. L. Mendoza-Cortes, *J Phys Chem C* **2017**, 121, 21160; l)X. Ding, J. Guo, X. Feng, Y. Honsho, J. Guo, S. Seki, P. Maitarad, A. Saeki, S. Nagase, D. Jiang, *Angew. Chem., Int. Ed.* **2011**, 50, 1289; m)T. Sick, A. G. Hufnagel, J. Kampmann, I. Kondofersky, M. Calik, J. M. Rotter, A. Evans, M. Döblinger, S. Herbert, K. Peters, *J. Am. Chem. Soc.* **2017**, 140, 2085; n)P.-F. Wei, M.-Z. Qi, Z.-P. Wang, S.-Y. Ding, W. Yu, Q. Liu, L.-K. Wang, H.-Z. Wang, W.-K. An, W. Wang, *J. Am. Chem. Soc.* **2018**, 140, 4623.

[123] a)K. Geng, T. He, R. Liu, S. Dalapati, K. T. Tan, Z. Li, S. Tao, Y. Gong, Q. Jiang, D. Jiang, *Chem. Rev.* **2020**, 120, 8814; b)H. R. Abuzeid, A. F. M. El-Mahdy, S.-W. Kuo, *Giant* **2021**, 6, 100054; c)X. Feng, X. Ding, D. Jiang, *Chem. Soc. Rev.* **2012**, 41, 6010; d)S.-Y. Ding, W. Wang, *Chem. Soc. Rev.* **2013**, 42, 548; e)X. Guan, F. Chen, Q. Fang, S. Qiu, *Chem. Soc. Rev.* **2020**, 49, 1357; f)Y. Yusran, X. Guan, H. Li, Q. Fang, S. Qiu, *Natl. Sci. Rev.* **2020**, 7, 170; g)N. Huang, P. Wang, D. Jiang, *Nat Rev Mater* **2016**, 1, 1.

[124] R. P. Bisbey, W. R. Dichtel, *ACS Cent. Sci.* **2017**, 3, 533.

[125] a)D. Ongari, A. V. Yakutovich, L. Talirz, B. Smit, *ACS Cent. Sci.* **2019**, 5, 1663; b)Y. Lan, X. Han, M. Tong, H. Huang, Q. Yang, D. Liu, X. Zhao, C. Zhong, *Nat. Commun.* **2018**, 9, 1; c)M. Tong, Y. Lan, Q. Yang, C. Zhong, *Chem Eng Sci* **2017**, 168, 456.

[126] W. Chen, P. Chen, D. Chen, Y. Liu, G. Zhang, L. Wang, L. Chen, *Adv. Sci.* **2022**, 9, 2105517.

[127] S. Dalapati, M. Addicoat, S. Jin, T. Sakurai, J. Gao, H. Xu, S. Irle, S. Seki, D. Jiang, *Nat. Commun.* **2015**, 6, 1.

[128] R.-R. Liang, F.-Z. Cui, Q.-Y. Qi, X. Zhao, *CCS Chemistry* **2020**, 2, 139.

[129] H. Xu, J. Gao, D. Jiang, *Nat. Chem.* **2015**, 7, 905.

[130] T.-Y. Zhou, S.-Q. Xu, Q. Wen, Z.-F. Pang, X. Zhao, *J. Am. Chem. Soc.* **2014**, 136, 15885.

[131] N. Huang, L. Zhai, D. E. Coupry, M. A. Addicoat, K. Okushita, K. Nishimura, T. Heine, D. Jiang, *Nat Commun* **2016**, 7, 12325.

[132] a)F. J. Uribe-Romo, J. R. Hunt, H. Furukawa, C. Klöck, M. O'Keeffe, O. M. Yaghi, *J. Am. Chem. Soc.* **2009**, 131, 4570; b)G. Lin, H. Ding, D. Yuan, B. Wang, C. Wang, *J. Am. Chem. Soc.* **2016**, 138, 3302; c)Y. Zhang, J. Duan, D. Ma, P. Li, S. Li, H. Li, J. Zhou, X. Ma, X. Feng, B. Wang, *Angew. Chem., Int. Ed.* **2017**, 56, 16313; d)O. Yahiaoui, A. N. Fitch, F. Hoffmann, M. Fröba, A. Thomas, J. Roeser, *J. Am. Chem. Soc.* **2018**, 140, 5330; e)T. Ma, E. A. Kapustin, S. X. Yin, L. Liang, Z. Zhou, J. Niu, L.-H. Li, Y. Wang, J. Su, J. Li, *Science* **2018**, 361, 48; f)H. Li, F. Chen, X. Guan, J. Li, C. Li, B. Tang, V. Valtchev, Y. Yan, S. Qiu, Q. Fang, *J. Am. Chem. Soc.* **2021**, 143, 2654; g)H. Li, J. Ding, X. Guan, F. Chen, C. Li, L. Zhu, M. Xue, D. Yuan, V. Valtchev, Y. Yan, *J. Am. Chem. Soc.* **2020**, 142, 13334.

[133] J. Li, X. Jing, Q. Li, S. Li, X. Gao, X. Feng, B. Wang, *Chem. Soc. Rev.* **2020**, 49, 3565.

[134] S. Kandambeth, A. Mallick, B. Lukose, M. V. Mane, T. Heine, R. Banerjee, *J. Am. Chem. Soc.* **2012**, 134, 19524.

[135] P. Kuhn, M. Antonietti, A. Thomas, *Angew. Chem., Int. Ed.* **2008**, 47, 3450.

[136] N. L. Campbell, R. Clowes, L. K. Ritchie, A. I. Cooper, *Chem Mater* **2009**, 21, 204.

[137] a)J. H. Bang, K. S. Suslick, *Adv. Mater.* **2010**, 22, 1039; b)T. Friščić, *J. Mater. Chem.* **2010**, 20, 7599.

[138] a)C. Zheng, X. Zhou, H. Cao, G. Wang, Z. Liu, *J Power Sources* **2014**, 258, 290; b)J. Niu, R. Shao, J. Liang, M. Dou, Z. Li, Y. Huang, F. Wang, *Nano Energy* **2017**, 36, 322; c)K. Zhao, S. Liu, G. Ye, Q. Gan, Z. Zhou, Z. He, *J Mater Chem A* **2018**, 6, 2166.

[139] J. Guo, Y. Xu, S. Jin, L. Chen, T. Kaji, Y. Honsho, M. A. Addicoat, J. Kim, A. Saeki, H. Ihee, S. Seki, S. Irle, M. Hiramoto, J. Gao, D. Jiang, *Nat. Commun.* **2013**, 4, 2736.

[140] S. K. Das, K. Bhunia, A. Mallick, A. Pradhan, D. Pradhan, A. Bhaumik, *Micropor Mesopor Mat* **2018**, 266, 109.

[141] P. Bhanja, S. K. Das, K. Bhunia, D. Pradhan, T. Hayashi, Y. Hijikata, S. Irle, A. Bhaumik, *Acs Sustain Chem Eng* **2018**, 6, 202.

[142] Y. Yusran, H. Li, X. Guan, D. Li, L. Tang, M. Xue, Z. Zhuang, Y. Yan, V. Valtchev, S. Qiu, Q. Fang, *Adv. Mater.* **2020**, 32, 1907289, 1907289.

[143] J. Martin-Illan, L. Sierra, P. Ocón, F. Zamora, *Angew. Chem., Int. Ed.* , n/a.

[144] P. Bhanja, K. Bhunia, S. K. Das, D. Pradhan, R. Kimura, Y. Hijikata, S. Irle, A. Bhaumik, *ChemSusChem* **2017**, 10, 921.

[145] S. Kandambeth, J. Jia, H. Wu, V. S. Kale, P. T. Parvatkar, J. Czaban-Jóźwiak, S. Zhou, X. Xu, Z. O. Ameur, E. Abou-Hamad, *Adv. Energy Mater.* **2020**, 10, 2001673.

[146] A. F. El-Mahdy, Y. H. Hung, T. H. Mansoure, H. H. Yu, T. Chen, S. W. Kuo, *Chem. Asian J.* **2019**, 14, 1429.

[147] a)A. M. Khattak, Z. A. Ghazi, B. Liang, N. A. Khan, A. Iqbal, L. Li, Z. Tang, *J Mater Chem A* **2016**, 4, 16312; b)L. Li, F. Lu, R. Xue, B. Ma, Q. Li, N. Wu, H. Liu, W. Yao, H. Guo, W. Yang, *ACS Appl. Mater. Interfaces* **2019**, 11, 26355; c)Y. Gao, C. Zhi, P. Cui, K. A. Zhang, L.-P. Lv, Y. Wang, *Chem. Eng. J.* **2020**, 400, 125967; d)M. Mahato, S. Nam, R. Tabassian, S. Oh, V. H. Nguyen, I. K. Oh, *Adv. Funct. Mater.* **2022**, 32, 2107442; e)C. Weng, X. Li, Z. Yang, H. Long, C. Lu, L. Dong, S. Zhao, L. Tan, *Chem. Commun.* **2022**, 58, 6809.

[148] B. C. Patra, S. Bhattacharya, *Chem Mater* **2021**, 33, 8512.

[149] T. Li, W.-D. Zhang, Y. Liu, Y. Li, C. Cheng, H. Zhu, X. Yan, Z. Li, Z.-G. Gu, *J Mater Chem A* **2019**, 7, 19676.

[150] X. Xu, R. Xiong, Z. Zhang, X. Zhang, C. Gu, Z. Xu, S. Qiao, *Chem. Eng. J.* **2022**, 447, 137447.

[151] T. Li, X. Yan, W.-D. Zhang, W.-K. Han, Y. Liu, Y. Li, H. Zhu, Z. Li, Z.-G. Gu, *Chem. Commun.* **2020**, 56, 14187.

[152] A. Halder, M. Ghosh, A. Khayum M, S. Bera, M. Addicoat, H. S. Sasmal, S. Karak, S. Kurungot, R. Banerjee, *J. Am. Chem. Soc.* **2018**, 140, 10941.

[153] X. Wu, J. J. Hong, W. Shin, L. Ma, T. Liu, X. Bi, Y. Yuan, Y. Qi, T. Surta, W. Huang, *Nat Energy* **2019**, 4, 123.

[154] X. Meng, H.-N. Wang, S.-Y. Song, H.-J. Zhang, *Chem. Soc. Rev.* **2017**, 46, 464.

[155] Y. Yang, P. Zhang, L. Hao, P. Cheng, Y. Chen, Z. Zhang, *Angew. Chem., Int. Ed.* **2021**, 60, 21838.

[156] S. Haldar, R. Kushwaha, R. Maity, R. Vaidhyanathan, *ACS Mater. Lett.* **2019**, 1, 490.

[157] A. Khayum M, V. Vijayakumar, S. Karak, S. Kandambeth, M. Bhadra, K. Suresh, N. Acharambath, S. Kurungot, R. Banerjee, *ACS Appl. Mater. Interfaces* **2018**, 10, 28139.

[158] T.-L. Yang, J.-Y. Chen, S.-W. Kuo, C.-T. Lo, A. F. M. El-Mahdy, *Polymers* **2022**, 14, 3428.

[159] Y.-Y. Liu, X.-C. Li, S. Wang, T. Cheng, H. Yang, C. Liu, Y. Gong, W.-Y. Lai, W. Huang, *Nat. Commun.* **2020**, 11, 5561.

[160] Y. Yang, K. Börjesson, *Trends Chem.* **2022**, 4, 60.

[161] A. K. Mohammed, V. Vijayakumar, A. Halder, M. Ghosh, M. Addicoat, U. Bansode, S. Kurungot, R. Banerjee, *ACS Appl. Mater. Interfaces* **2019**, 11, 30828.

[162] a)Y. Han, Q. Zhang, N. Hu, X. Zhang, Y. Mai, J. Liu, X. Hua, H. Wei, *Chin. Chem. Lett.* **2017**, 28, 2269; b)X. Kong, S. Zhou, M. Strømme, C. Xu, *Carbon* **2021**, 171, 248; c)F. Liu, C. Wang, C. Liu, Z. Yu, M. Xu, Y. Chen, L. Wei, *Appl. Phys. Lett.* **2021**, 119, 211905.

[163] Y. Dai, Y. Wang, X. Li, M. Cui, Y. Gao, H. Xu, X. Xu, *Electrochim. Acta* **2022**, 421, 140470.

[164] C. Li, J. Yang, P. Pachfule, S. Li, M.-Y. Ye, J. Schmidt, A. Thomas, *Nat. Commun.* **2020**, 11, 1.

[165] L. Xu, F. Wang, X. Ge, R. Liu, M. Xu, J. Yang, *Micropor Mesopor Mat* **2019**, 287, 65.

[166] Q. Geng, H. Wang, Y. Wu, L.-P. Lv, S. Chen, W. Sun, Y. Wang, *ChemElectroChem* **2022**, 9, e202200340.

[167] C. Wang, F. Liu, J. Chen, Z. Yuan, C. Liu, X. Zhang, M. Xu, L. Wei, Y. Chen, *Energy Storage Mater* **2020**, 32, 448.

[168] a)C. Wang, F. Liu, S. Yan, C. Liu, Z. Yu, J. Chen, R. Lyu, Z. Wang, M. Xu, S. Dai, Y. Chen, L. Wei, *Carbon* **2022**, 190, 412; b)N. An, Z. Guo, J. Xin, Y. He, K. Xie, D. Sun, X. Dong, Z. Hu, *J Mater Chem A* **2021**, 9, 16824.

[169] M. Yao, C. Guo, Q. Geng, Y. Zhang, X. Zhao, X. Zhao, Y. Wang, *Ind. Eng. Chem. Res.* **2022**, 61, 7480.

[170] Y. Dong, Y. Wang, X. Zhang, Q. Lai, Y. Yang, *Chem. Eng. J.* **2022**, 449, 137858.

[171] C. Peng, H. Yang, S. Chen, L. Wang, *J. Energy Storage* **2020**, 32, 101786.

[172] Z. Xu, Y. Liu, Z. Wu, R. Wang, Q. Wang, T. Li, J. Zhang, J. Cheng, Z. Yang, S. Chen, *Chem. Eng. J.* **2020**, 387, 124071.

[173] Y. Jiang, Z. Zhang, D. Chen, J. Du, Y. Yang, S. Wang, F. Guo, X. Chen, C. Gao, W. J. Wang, P. Liu, *Adv. Mater.* **2022**, n/a, e2204250.

[174] X. Zhao, M. Sajjad, Y. Zheng, M. Zhao, Z. Li, Z. Wu, K. Kang, L. Qiu, *Carbon* **2021**, 182, 144.

[175] S. Haldar, D. Rase, P. Shekhar, C. Jain, C. P. Vinod, E. Zhang, L. Shupletsov, S. Kaskel, R. Vaidhyanathan, *Adv. Energy Mater.* **2022**, 12, 2200754.

[176] G. Kim, T. Shiraki, T. Fujigaya, *B Chem Soc Jpn* **2020**, 93, 414.

[177] Z. Zhou, X. Zhang, L. Xing, J. Liu, A. Kong, Y. Shan, *Electrochim. Acta* **2019**, 298, 210.

[178] L. Li, F. Lu, H. Guo, W. Yang, *Micropor Mesopor Mat* **2021**, 312, 110766.

[179] S. Umezawa, T. Douura, K. Yoshikawa, Y. Takashima, M. Yoneda, K. Gotoh, V. Stolojan, S. R. P. Silva, Y. Hayashi, D. Tanaka, *Carbon* **2021**, 184, 418.

[180] M. Kim, P. Puthiaraj, Y. Qian, Y. Kim, S. Jang, S. Hwang, E. Na, W.-S. Ahn, S. E. Shim, *Electrochim. Acta* **2018**, 284, 98.

[181] J. Sun, A. Klechikov, C. Moise, M. Prodana, M. Enachescu, A. V. Talyzin, *Angew. Chem., Int. Ed.* **2018**, 57, 1034.

[182] M. Ibrahim, H. N. Abdelhamid, A. M. Abuelftooh, S. G. Mohamed, Z. Wen, X. Sun, *J. Energy Storage* **2022**, 55, 105375.
[183] D. J. Kim, J. W. Yoon, C. S. Lee, Y.-S. Bae, J. H. Kim, *Appl Surf Sci* **2018**, 439, 833.
[184] S. Vargheese, D. Pattappan, K. V. Kavya, M. S. Sivaramkumar, R. T. R. Kumar, Y. Haldorai, *Carbon Letters* **2021**, 31, 1309.
[185] H. Zhang, L. Lin, B. Wu, N. Hu, *J Power Sources* **2020**, 476, 228527.
[186] Z. Mu, Y. Zhu, B. Li, A. Dong, B. Wang, X. Feng, *J. Am. Chem. Soc.* **2022**, 144, 5145.
[187] S. Bi, H. Banda, M. Chen, L. Niu, M. Chen, T. Wu, J. Wang, R. Wang, J. Feng, T. Chen, M. Dincă, A. A. Kornyshev, G. Feng, *Nat. Mater.* **2020**.
[188] P. J. Waller, S. J. Lyle, T. M. Osborn Popp, C. S. Diercks, J. A. Reimer, O. M. Yaghi, *J. Am. Chem. Soc.* **2016**, 138, 15519.
[189] a)S. Ardizzone, G. Fregonara, S. Trasatti, *Electrochim. Acta* **1990**, 35, 263; b)J. Wang, J. Polleux, J. Lim, B. Dunn, *J Phys Chem C* **2007**, 111, 14925.
[190] G. Gourdin, V. Doan-Nguyen, *Cell Rep Phys Sci* **2021**, 2, 100660.
[191] D. P. Tabor, R. Gómez-Bombarelli, L. Tong, R. G. Gordon, M. J. Aziz, A. Aspuru-Guzik, *J Mater Chem A* **2019**, 7, 12833.
[192] E. Jin, M. Asada, Q. Xu, S. Dalapati, M. A. Addicoat, M. A. Brady, H. Xu, T. Nakamura, T. Heine, Q. Chen, D. Jiang, *Science* **2017**, 357, 673.
[193] X. Chen, X. Jiang, N. Yang, *Small* **2022**, 18, 2201135.
[194] X. Chen, M. Addicoat, S. Irle, A. Nagai, D. Jiang, *J. Am. Chem. Soc.* **2013**, 135, 546.
[195] F. Haase, B. V. Lotsch, *Chem. Soc. Rev.* **2020**, 49, 8469.
[196] Y. Tao, W. Ji, X. Ding, B.-H. Han, *J Mater Chem A* **2021**, 9, 7336.
[197] a)F. Liu, C. Wang, X. Sui, M. A. Riaz, M. Xu, L. Wei, Y. Chen, *Carbon Energy* **2019**, 1, 173; b)P. Simon, *ACS Nano* **2017**, 11, 2393.
[198] a)J. I. Feldblyum, C. H. McCreery, S. C. Andrews, T. Kurosawa, E. J. G. Santos, V. Duong, L. Fang, A. L. Ayzner, Z. Bao, *Chem. Commun.* **2015**, 51, 13894; b)K. Dey, M. Pal, K. C. Rout, S. Kunjattu H, A. Das, R. Mukherjee, U. K. Kharul, R. Banerjee, *J. Am. Chem. Soc.* **2017**, 139, 13083.
[199] D. Mullangi, S. Shalini, S. Nandi, B. Choksi, R. Vaidhyanathan, *J Mater Chem A* **2017**, 5, 8376.
[200] Y. Dong, J. Zhu, Q. Li, S. Zhang, H. Song, D. Jia, *J Mater Chem A* **2020**, 8, 21930.
[201] a)S. Chen, B. Yuan, G. Liu, D. Zhang, *Frontiers in Chemistry* **2020**, 8; b)F. Yu, W. Liu, S.-W. Ke, M. Kurmoo, J.-L. Zuo, Q. Zhang, *Nature Communications* **2020**, 11, 5534.
[202] a)Y. Jiao, Y. Zheng, M. Jaroniec, S. Z. Qiao, *Chemical Society Reviews* **2015**, 44, 2060; b)M. Shao, Q. Chang, J.-P. Dodelet, R. Chenitz, *Chemical reviews* **2016**, 116, 3594.
[203] M. K. Debe, *Nature* **2012**, 486, 43.
[204] a)S. Liu, Z. Wang, S. Zhou, F. Yu, M. Yu, C. Y. Chiang, W. Zhou, J. Zhao, J. Qiu, *Advanced Materials* **2017**, 29, 1700874; b)S. Sakong, A. Groß, *Physical Chemistry Chemical Physics* **2020**, 22, 10431; c)A. Kumar, G. Yasin, V. K. Vashistha, D. K. Das, M. U. Rehman, R. Iqbal, Z. Mo, T. A. Nguyen, Y. Slimani, M. T. Nazir, *Diamond and Related Materials* **2021**, 113, 108272.
[205] U. I. Koslowski, I. Abs-Wurmbach, S. Fiechter, P. Bogdanoff, *The Journal of Physical Chemistry C* **2008**, 112, 15356.
[206] H. Xu, D. Cheng, D. Cao, X. C. Zeng, *Nature Catalysis* **2018**, 1, 339.
[207] a)P. Liu, Y. Zhao, R. Qin, S. Mo, G. Chen, L. Gu, D. M. Chevrier, P. Zhang, Q. Guo, D. Zang, *Science* **2016**, 352, 797; b)A. Wang, J. Li, T. Zhang, *Nature Reviews Chemistry* **2018**, 2, 65; c)P. Hu, Z.

Huang, Z. Amghouz, M. Makkee, F. Xu, F. Kapteijn, A. Dikhtiarenko, Y. Chen, X. Gu, X. Tang, *Angewandte Chemie International Edition* **2014**, 53, 3418; d)H. Yan, H. Cheng, H. Yi, Y. Lin, T. Yao, C. Wang, J. Li, S. Wei, J. Lu, *Journal of the American chemical society* **2015**, 137, 10484; e)U. I. Kramm, I. Herrmann-Geppert, J. Behrends, K. Lips, S. Fiechter, P. Bogdanoff, *Journal of the American Chemical Society* **2016**, 138, 635.

[208] F. Li, G.-F. Han, H.-J. Noh, S.-J. Kim, Y. Lu, H. Y. Jeong, Z. Fu, J.-B. Baek, *Energy & Environmental Science* **2018**, 11, 2263.

[209] Y. C. Wang, Y. J. Lai, L. Song, Z. Y. Zhou, J. G. Liu, Q. Wang, X. D. Yang, C. Chen, W. Shi, Y. P. Zheng, *Angewandte Chemie* **2015**, 127, 10045.

[210] T. Sun, S. Zhao, W. Chen, D. Zhai, J. Dong, Y. Wang, S. Zhang, A. Han, L. Gu, R. Yu, *Proceedings of the National Academy of Sciences* **2018**, 115, 12692.

[211] a)S. Yang, Y. Yu, M. Dou, Z. Zhang, L. Dai, F. Wang, *Angewandte Chemie International Edition* **2019**, 58, 14724; b)P. Peng, Z. Zhou, J. Guo, Z. Xiang, *ACS Energy Letters* **2017**, 2, 1308.

[212] L. Ma, S. Wang, X. Feng, B. Wang, *Chinese Chemical Letters* **2016**, 27, 1383.

[213] X. Cui, S. Lei, A. C. Wang, L. Gao, Q. Zhang, Y. Yang, Z. Lin, *Nano Energy* **2020**, 70, 104525.

[214] S.-Y. Ding, W. Wang, *Chemical Society Reviews* **2013**, 42, 548.

[215] W. Niu, K. Marcus, L. Zhou, Z. Li, L. Shi, K. Liang, Y. Yang, *ACS Catalysis* **2018**, 8, 1926.

[216] a)W. Auwärter, D. Écija, F. Klappenberger, J. V. Barth, *Nature chemistry* **2015**, 7, 105; b)X. Wang, X. Ding, T. Wang, K. Wang, Y. Jin, Y. Han, P. Zhang, N. Li, H. Wang, J. Jiang, *ACS Applied Materials & Interfaces* **2022**, 14, 41122.

[217] M. A. Meitl, Y. Zhou, A. Gaur, S. Jeon, M. L. Usrey, M. S. Strano, J. A. Rogers, *Nano Letters* **2004**, 4, 1643.

[218] R. M. Myers, D. E. Fitzpatrick, R. M. Turner, S. V. Ley, *Chemistry–A European Journal* **2014**, 20, 12348.